Title
Design, Fabrication and Testing of Angled Fiber Suspension for Electrostatic Actuators

Author
Schubert, Bryan Edward

Publication Date
2011

Design, Fabrication and Testing of Angled Fiber Suspension for Electrostatic Actuators

by

Bryan Edward Schubert

A dissertation submitted in partial satisfaction of the
requirements for the degree of
Doctor of Philosophy

in

Engineering - Electrical Engineering and Computer Sciences

in the

Graduate Division

of the

University of California, Berkeley

Committee in charge:

Professor Ronald S. Fearing, Chair
Professor Ali Javey
Professor Roya Maboudian

Spring 2011

Design, Fabrication and Testing of Angled Fiber Suspension for Electrostatic Actuators

Abstract

Design, Fabrication and Testing of Angled Fiber Suspension for Electrostatic Actuators

by

Bryan Edward Schubert

Doctor of Philosophy in Engineering - Electrical Engineering and Computer Sciences

University of California, Berkeley

Professor Ronald S. Fearing, Chair

A suspension comprised of angled fibers is proposed as a new means for achieving high strain, high stress, energy dense electrostatic actuators. Angled fiber arrays have low density and can be placed between the electrodes of a parallel plate or comb-drive type actuator to create a self-contained actuator sheet with low mass and volume. Angled fibers also have a Poisson's ratio of zero, allowing the use of robust, rigid electrodes, and they can be composed of stiff materials with low viscoelastic properties. This is in contrast to the alternative technology of dielectric elastomers that depend on unreliable compliant electrodes and highly viscoelastic dielectrics. Performance limits of an ideal nanometer-scale actuator, such as energy density, stress and strain, and efficiency are considered through theoretical modeling. A micrometer scale prototype is fabricated using a novel fiber peeling technique that easily produces high-aspect-ratio (1.8 μm radius, 66 μm long), angled microfibers. The microfibers are used as a suspension for a parallel plate actuator. The prototype actuator is characterized through static and dynamic tests, to reveal a maximum static strain of 3.4% at a static stress of 0.8 kPa (electric field of 13.9 V/μm), a fast unloaded step response of < 2 ms, a Q of 12.9 and a power density of 12.8 W/kg when driving an inertial load in resonance at 845 Hz.

To my amazing wife, Jessica.

Contents

List of Figures

List of Tables

Acknowledgments

There are a lot of people that have helped me during my graduate studies at Berkeley. I would first like to thank my advisor, Prof. Ronald Fearing, for his constant encouragement, wisdom and seemingly endless supply of clever ideas. I would also like to thank my other committee members, Prof. Roya Maboudian and Prof. Ali Javey, for their insightful comments on my research over the years. I would also like to acknowledge Prof. Kyriakos Komvopoulos who was a valued member of my qualifying committee. Additionally, I would like to offer my thanks to Prof. Kellar Autumn and Prof. Robert Full for their help with my gecko-related research.

Next, I would like to mention some of my fellow graduate students. This group of people was always willing to toss around ideas or offer assistance with tough problems. Dr. Carmel Majidi provided invaluable help with theoretical models. Dr. Richard Groff's Simulink models formed the foundation for my experimental test setup. Dr. Brian Bush, Dr. Dae Ho Lee, Dr. Jongho Lee and Andrew Gillies were always more than willing to SEM whatever crazy new device I had fabricated. Andrew Gillies was also very patient in assisting with data collection using his force sensing apparatus. I would also like to thank Fernando Garcia Bermudez, Paul Birkmeyer, Stan Baek, Dr. Aaron Hoover and Dr. Erik Steltz for being nice enough to let me win an occasional game of nine ball. The rest of my lab is also deserving of thanks for listening to my research problems every week during group meeting, and for offering numerous suggestions. They are (in alphabetical order): Korok Chatterjee, Michael Cohen, Xiao-Yu Fu, Jaakko Karras, Nick Kohut, Kevin Ma, Kevin Peterson and Andrew Pullin.

I would also like to acknowledge some of the friends that I have made while working at Berkeley. They include Marci Meingast, Vincent Duindam, Ephrat Bitton, Alvaro Cardenas and Gelareh Taban. They have been invaluable in making the most of my free time.

I would also like to thank my family, whose complete faith in my abilities has kept me motivated over the years. I would especially like to thank my brother-in-law, Dr. Andrew McCarthy, whose daily words of inspiration helped me through the difficult task of writing this dissertation.

Finally, I want to thank my wife for her love, patience and support during this long process. This task would have been much harder without her by my side.

Chapter 1

Introduction

Actuators are one of the key elements limiting the creation of dynamic micro-robots. At the large scale, the robot designer has a wide choice of powerful, efficient, reliable actuation mechanisms, including pneumatics and electromagnetic motors. However, when transitioning to small scale designs, traditional actuators, such as motors, begin to suffer issues related to low power density and efficiency. For the case of motors, the housing becomes a significant part of the overall weight, therefore lowering the power-to-weight ratio. Furthermore, extra gearing mechanisms are generally required that lower the power-to-weight ratio even further. Additionally, frictional losses also become more significant in small motors [97].

For small scale robots, there is also a wide range of actuator technologies available, but most are lacking in key aspects such as maximum stress and strain, energy density or reliability. Some are well established, such as piezoelectric ceramics, and others, such as dielectric elastomers, are the subject of ongoing research. However, as actuator technology currently stands, there is not a suitable solution for small-scale robotics. Of the many technologies, only a few have been used to make working robots: DEAs in walking robots [12], IPMCs in swimming robots [17], piezoelectric ceramic in flying robots [98] and shape memory alloy in crawling robots [35].

As with large-scale robots, small-scale robots require efficient, energy dense actuation with large strain and force capabilities, and good static and dynamic reponses. Each technology has advantages and disadvantages in terms of these metrics as will be discussed further in Chapter 2 (see Table 2.1). Shape memory alloy has a very high elastic energy density (0.78 J/g), but it is too slow ($<$10 Hz) and inefficient for dynamic locomotion [93]. Piezoelectric ceramics have high efficiency, stress and speed, but they can only produce small strains ($<$0.1%) [91]. Ionic polymer-metal composites (IPMCs) also suffer from small strains ($<$3%) and can only be used as bending actuators, but they require very little voltage ($\sim$1-3 V) and can be used underwater (hence the large number of swimming robots using these actuators) [17]. DEAs have the highest strains (30% up to 380%) and they are able to generate large stresses ($>$1 MPa), resulting in large elastic energy density ($>$3.4 J/g). However, they are not without their problems.

DEAs in principle are a nice compact electrostatic actuator. The elastic energy density is high because the dielectric acts to both amplify the electric field, and also serves as the suspension.

The highly compliant dielectric also allows large elastic strains. However, in practice, the highly compliant electrode introduces a number of problems. The DEAs that report the largest strains ($>$ 380%) suffer severely from creep, preventing them from holding static loads because of pull-in failures (dielectric creeps until the field reaches breakdown), causing large losses at low frequencies (90% at 10 Hz) [71]. A constant prestrain can be applied to offset these problems, but this requires the addition of bulky frames around the actuator [12]. Furthermore, because the dielectric is incompressible, DEAs need flexible electrodes that can maintain electrical continuity with very high strains. The electrode technology has advanced somewhat with the use of CNTs that self-limit breakdown, but even this solution can lead to losses due to air ionization [99]. Finally, because of viscoelastic issues, DEAs need to be fairly thick to avoid breakdown at high fields ($>$ 200 V/μm), and this translates into large voltages ($>$ 1 kV).

Building off the DEA concept of a sandwiched suspension, we propose a distributed support structure composed of angled fibers that has an effective Poisson's ratio of zero. This allows the use of rigid electrodes. Electrostatic actuators with rigid electrodes, such as parallel plate or comb-drive actuators, are appealing because of their high efficiency ($>$90%), long lifetime, quick response time ($>$100 kHz and limited primarily by actuator stiffness and mass instead of diffusion (IPMCs) or thermal transport (SMA)), and their ability for low-power static hold (ideally zero if there is no leakage current).

However, electrostatic actuators with rigid electrodes suffer from some of the same problems as DEAs; namely, they require a high electric field to attain high energy density. There are two problems with high electric fields. One problem is attaining them, and the other is limiting the required voltage. Both problems have the same solution; make the gap as small as possible. While this is not an option with DEAs because of creep-related failures, angled fibers can be made out of materials with low viscoelasticity because their compliance is primarily related to geometry. By using more rigid materials, such as high-density polymers, creep can be mitigated, allowing very small gaps. However, the compliance and elastic strain limit will not suffer because, as will be shown in Chapter 3, high elastic strains ($>$50%) are possible by adjusting the fiber angle.

One potential drawback of dividing the dielectric into individual fibers is that it lowers the relative permittivity. However, as will be discussed in depth in the design and modelling chapter, decreasing the gap below 1 μm can increase the allowable electric field before breakdown by 3-4 orders of magnitude (up to 2300 V/μm [36] equivalent to $>$ 23 MPa for a parallel plate actuator in air). For a gap of 100 nm, applying just 10 V will result in an electrostatic stress of 4 N/cm^2.

Fiber supports also have a low density ($\sim$90% less than solid), allowing the creation of lightweight actuators, which is important for small-scale robots with low payload capability. Finally, by incorporating the support structure within the electrodes, arbitrarily large sheets of actuator material can be generated. These sheets can then easily be cut, rolled, or stacked to create the appropriate actuator dimensions for the application.

The following chapters will discuss the current field of actuators through a detailed survey, explore design criteria and actuator limits through modelling, and fabricate and test a microscale prototype of a parallel-plate actuator with angled microfiber suspension.

1.1 Contributions

This work builds on the field of electrostatic actuators. Specifically:

- Chapter 2 presents a detailed survey of the current small-scale actuator field. Technologies considered are piezoelectrics (both ceramic and polymeric), shape memory alloy, dielectric elastomers, ionic polymer-metal composites, carbon nanotubes sheets, thermal, magnetic and electrostatic actuators.
- Chapter 3 explores the design considerations for creating electrostatic actuators with compliant, compressible dielectrics. Topics covered include the electric field limit due to dielectric breakdown; the elastic strain limits of angled fibers and porous foam supports; potential losses due to the dielectric, viscoelasticity and air damping, and trade-offs between parallel-plate and comb-drive type electrodes.
- Chapter 4 details a fabrication technique for generating angled, high-aspect-ratio microfibers by controlled demolding through peeling. This chapter also looks at the fiber radius and length limits from the standpoint of cold-drawing of polymers.
- Chapter 5 characterizes the parallel-plate, angled-fiber actuator prototype through the use of DC and AC analysis. The static and dynamic responses are compared with theoretical predictions from Chapter 3. In particular, the strain, stress, losses and power density are estimated from experimental data and theoretical models.

Chapter 2

Survey of Actuators

The following is a comparison of some of the actuator technologies that may be viable at the small scale. Table 2.1 gives a comparison of representative examples of each technology. Most of the numbers are from ideal laboratory settings so they do not necessarily reflect the expected performance of an integrated actuator. Often these numbers neglect practical considerations such as the volume or weight of support structures necessary to achieve useful force and motion. Therefore, these numbers should not be taken as absolute truth for any given technology.

2.1 Piezoelectric Ceramics

Piezoelectric ceramics, such as lead zirconate titanate (PZT), are polycrystalline ferroelectric materials. Above the Curie temperature, these materials have no dipoles and thus no polarization. Below the Curie temperature, the positive and negative charge sites no longer cancel each other out, so the unit cells display a built in electric dipole [91]. Groups of neighboring dipoles will align with each other to form polarized domains, known as Weiss domains. The Weiss domains throughout a material can be out of alignment with each other by 90° or 180°, leading to no net polarization. However, if a high enough poling voltage is applied to the material, the domains can be forced to line up in the direction of the poling field, causing the material to stretch along the poling direction. After the poling voltage is removed, the domains reorder slightly, but they remain approximately aligned, locking in some level of strain. The material now behaves like a piezoelectric. However, the ceramic can become depolarized if it is subjected to a high electric field opposite to the poling field, a high mechanical stress that causes reorientation of the domains, or if it is heated above its Curie temperature. The hysteresis loop for the described behavior is shown in Figure 2.1(b).

Actuation can be caused by applying an electric field to the piezoelectric. A field with the same polarity as the original poling field will cause the material to stretch in the field direction until all the dipoles are aligned. Once the dipoles are aligned, increasing the voltage has no effect. If a field is applied with opposite polarity to the original poling field, then the material will compress

Actuator	Maximum strain (%)	Maximum stress (MPa)	Elastic modulus (MPa)	Electric field (MV/m)	Specific elastic energy density (J/g)	Volume elastic energy density (J/cm^3)	Efficiency (%)	Specific density (g/cm^3)	Frequency (kHz)	References
Dielectric elastomer (prestrained acrylic)	380^a 79^t	7.2	3.0	412	3.4	3.4	60-80	1	0.03	[12, 67]
Dielectric elastomer (unstrained acrylic)	7.5^a 7^t	0.16	3.0	17	0.0057	0.0057	-	1	0.03	[12]
Dielectric elastomer (prestrained silicone)	64^a 39^t	3.0	1.0	350	0.75	0.75	90	1	2-20	[12, 67]
Dielectric elastomer (unstrained silicone)	32	1.36	1.0	235	0.22	0.2	90	1	2-20	[12, 67]
Electrostrictive polymer (P(VDF-TrFE))	4.3	43	1000	150	0.49	0.92	$\sim$80	1.8	$>$10	[12, 19]
Liquid crystal elastomer	2	2	100	25	0.02	0.02	$\sim$75	0.97	0.1	[12, 13, 38]
Ferroelectret (polypropylene)	1.6	0.016	1^f	54	0.00065	0.00026	-	0.4^e	$<$50	[7, 8, 56, 94]
Piezoelectric ceramic (PZT)	0.1	50	50000	1.5	0.003	0.025	$>$90	7.8	$>$20	[91, 70]
Piezoelectric polymer (PVDF)	0.1	3	3000	30	0.0008	0.0015	$<$1	1.8	1	[39]
Shape memory alloy (Flexinol®)	5	100	$>$28000*	N/A	0.78	5	$<$10	6.45	0.01	[23, 39]
IPMC (Nafion)	$<$10	10-30	100-500	0.004-0.28	0.06-0.18	0.15-0.45	-	2.5	$<$0.1	[60, 79, 80]
Ionic gels (PAAM-PAA)	10	0.01	0.12^e	$\sim$0.008	0.0005	0.0005	-	$\sim$1	$<$0.001	[51]
Conductive polymer (PANi)	1.5	3.3	220^e	0.03	0.051	0.049	0.024	0.96	0.000003	[83]
CNT (electrolytic)	0.08	8.4	1200	$\sim$0.003	0.0025	0.0033	-	1.33	0.0001	[9]
CNT (aerogel)	1	3.2	320^e	$\sim$0.2	0.02	0.016	-	0.8	1	[2]
Magnetostrictive (Terfenol-D)	0.2	70	3500	N/A	0.008	0.07	$<$30	9.25	$>$1	[39, 25]
Electromagnetic (voice coil)	50	0.03	-	-	0.0015	0.0025	$>$90	8	20	[12]
Thermal (Al, δT=200K)	0.48	326	68000	N/A	0.58	1.56	$<$10	2.7	$<$0.001	[12, 55]
Electrostatic (integrated force array)	11	0.0082	0.075^f	65^e	0.001	0.0009	$>$90	0.84^e	-	[11, 43, 55]
Human muscle (skeletal)	$>$40	0.35	60	N/A	0.067	0.07	$>$35	1.04	$<$10	[39]

Table 2.1: Comparison of actuator materials. ^{a}Area strain. ^{e}Estimated value from calculations. ^{f}Effective modulus. ^{t}Thickness strain. *Modulus varies between 28-40 GPa for martensite and increases to 80 GPa for austenite [23].

in the direction of the applied field. If this voltage is increased, it will eventually cause the dipoles to realign with the new field, flipping their polarization direction. This behavior characterizes dielectric hysteresis seen in piezoelectrics [91].

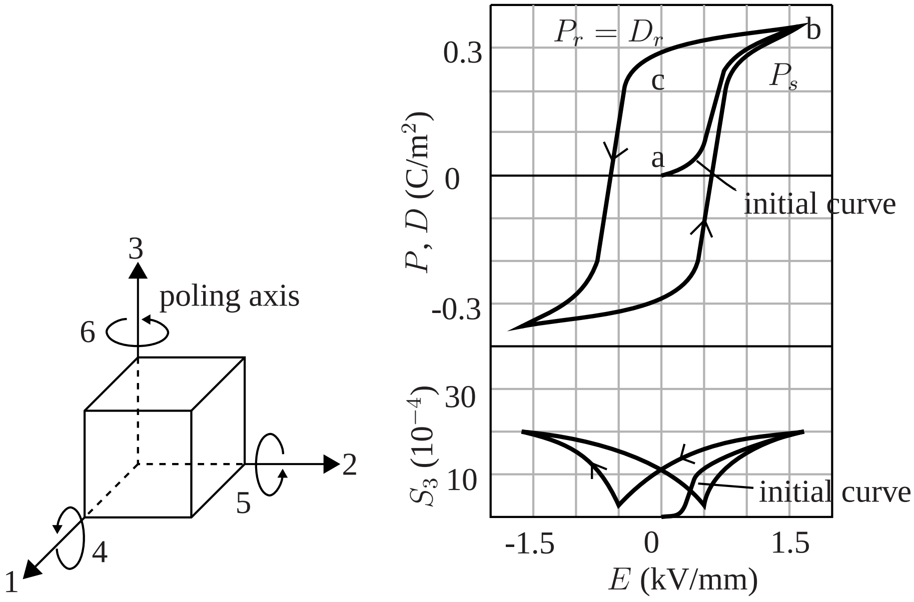

(a) (b)

Figure 2.1: (a) Reference axes for piezoelectric subscripts. (b) Example hysteresis curve for PZT [91]. Marked positions correspond to a. unpolarized, b. polarized to saturation and c. default state after polarization.

The charge and strain of a piezoelectric are coupled because of its ability to act as either a generator or actuator. The strain, S, is given by

$$S = s^E T + dE, \tag{2.1}$$

where s^E is the compliance ($s = 1/Y$) of the ceramic given a constant electric field, E, T is the applied stress, and d is the piezoeletric charge constant. The piezoelectric charge constant represents the materials ability to convert stress to induced polarization (units of coulombs per newton), or the induced strain per unit applied electric field (units of meters per volt). The dielectric displacement, D, is given by

$$D = dT + \epsilon^T E, \tag{2.2}$$

where ϵ^T is the permittivity under constant stress. All of the constants represent tensor quantities since piezoelectric ceramics are anisotropic [91]. For instance, we can choose the Z axis of a rectangular system to be the direction of positive polarization, and denote X, Y, and Z as 1, 2, and 3, respectively, with shear about these axes represented by 4, 5, 6, respectively (see Figure 2.1(a)). Then, constants can be written with subscripts referencing these values. For example, d_{33} is the induced polarization per unit applied stress in direction 3, and d_{31}, is the induced polarization in direction 3 for a stress applied in direction 1 [91].

The piezoelectric constant is usually used as a metric for determining the quality of a piezoelectric material, where the better materials typically have a higher d value. For reference, PZT has a d_{33} value of ∼650 pm/V [70]. The maximum strain in piezoelectrics is limited by the maximum electric field strength and mechanical strain limit. If the field is applied in the poling direction, then the maximum field is determined by saturation (i.e. all the domains are aligned). If the field is applied opposite to the poling direction, then the maximum is when depolarization starts to occur. For PZT, saturation occurs at ∼1.5 V/μm, and depolarization takes place at 0.3 V/μm [70]. If the stress is set to zero, $T = 0$, then the maximum strain is $S_3 = d_{33}E_3 = 0.02$ to 0.1%. The stiffness is around 50 GPa, so the stress is 10 to 50 MPa. The actuation speed of piezoelectric ceramics is high, with operating frequencies well into the kilohertz range.

Because of the low strains achievable with piezoelectric ceramics, large displacements can not be obtained with a single plate because it would necessitate very high fields. Therefore, most practical ceramic piezoelectric actuators use stacked sheets electrically connected in parallel to achieve larger displacements at low voltages (∼50 V). Another option is to use the ceramic as a bending actuator by attaching it to either a sheet of unactuated material (unimorph) or another sheet of piezoelectric material (bimorph) [91]. In the bimorph actuator, the piezoelectric plates are electrically connected such that one plate contracts while the other expands, causing bending. While the bending configuration can result in higher displacements than a stack actuator, the piezoelectric constant in the poling direction (d_{33}) is usually about twice as large as in the transverse directions (d_{31}).

2.2 Electroactive Polymers (EAPs)

Generally stated, electroactive polymers are polymers that demonstrate some physical change in response to an electric stimulus. These changes are driven by electric fields and coulomb forces in the case of Electronic EAPs, or they are the result of the movement of ions in the case of Ionic EAPs [57]. These two categories cover a wide variety of interesting polymers that can be used to create actuators.

2.2.1 Electronic EAPs

Piezoelectric Polymers

Piezoelectric polymers have a non-centro-symmetric structure that results in the polymer chains being polarizable [12]. Similar to piezoelectric ceramics, whose dipoles align with an applied electric field, piezoelectric polymers will change phases in order to align their dipoles with an applied electric field. The phase change results in a semi-permanent polarization of the polymer. The polarization is reversible by applying a high opposite electric field, or by heating the polymer above its Curie temperature.

The most common piezoelectric polymer material is poly(vinylidene difluoride) (PVDF). This material is widely used because it exhibits the best electromechanical responses at room temperature [19]. PVDF has four possible crystal structures, but the two most important to actuation are the non-polar α-phase and the highly polar β-phase. Both phases are stable at room temperature, and both can be turned into a piezoelectric material by proper poling [52]. The default α-phase can be turned into the β-phase by stretching the polymer at low temperature ($<$90°). This causes orientation of the chains, making the polymer polar [52]. The β-phase requires a lower poling field (50 V/μm) than the α-phase (100 to 300 V/μm) to show piezoelectric behavior, and the β-phase has a higher piezoelectric coefficient (d_{33}=30 pm/V) than the α-phase (d_{33}=10-15 pm/V) [52]. The maximum stress and strain for PVDF is 3 MPa and 0.1%, respectively, at 30 V/μm [39].

Electrostrictive Polymers

Electrostrictive polymers are characterized as having polar crystalline groups within an amorphous or flexible material. These materials take advantage of the paraelectric-ferroelectric transition to achieve higher strains than piezoelectric polymers. P(VDF-TrFE) can be turned into an electrostrictive polymer by introducing defects that decrease the crystallite size in solid PVDF [12]. Defects can be introduced by exposing the polymer to high-energy electron irradiation or by adding chlorinated monomer to the copolymerization process. The modified material solves some of the problems of the original polymer actuator, such as large hysteresis (see Figure 2.2(a)), a narrow transition temperature region, and a high transition temperature [37]. The defects lower the paraelectric-ferroelectric transition temperature to near room temperature, broaden the transition region, and lower the energy barrier between phase transformations, reducing the hysteresis. The improved polymer is termed a relaxor ferroelectric [37]. Relaxor ferroelectrics have shown strain in the thickness direction near 5% for materials with elastic modulii of 0.3-1.2 GPa, under electric fields near 150 V/μm [12]. Strains of 2% have been shown with lower electric fields of 13 V/μm by increasing the dielectric constant of the material to 400 [37]. These materials also possess electromechanical coupling factors in excess of 0.6 (normal and transverse directions) and an energy density up to 1.1 J/g [19].

In addition to adding defects to solid PVDF, it is possible to create electrostrictive polymers by grafting polar P(VDF-TrFE) crystal to a flexible elastomeric backbone, as shown in Figure 2.2(b). Because the hybrid polymer is part polar crystals and part elastomer, it benefits from both the electrostriction effect and the Maxwell stress effect seen in pure dielectric elastomer actuators. However, the relative contribution of the Maxwell stress effect is less than 5% [6]. Demonstrated strains are $\sim$4%, with stresses around 22 MPa for an electric field of 120 V/μm. The elastic energy density is 0.44 J/cm^3 [86].

Other examples of electrostrictive polymers are liquid crystal elastomers (LCEs). LCEs are similar to graft polymers in that they are composed of intrinsically polarized elements, called mesogens, grafted to an elastomer chain. The mesogens will align with an electric field to cause bulk stress and strain. LCEs have been used to produce strains up to 4% at fields of 1.5 V/μm and speeds of ∼100 Hz [12]. However, to reach the upper range of their energy density (∼0.02 J/g), stiffer LCEs (E=100 MPa) must be used, resulting in lower strains of 2% and a electromechanical efficiency of 75% [38].

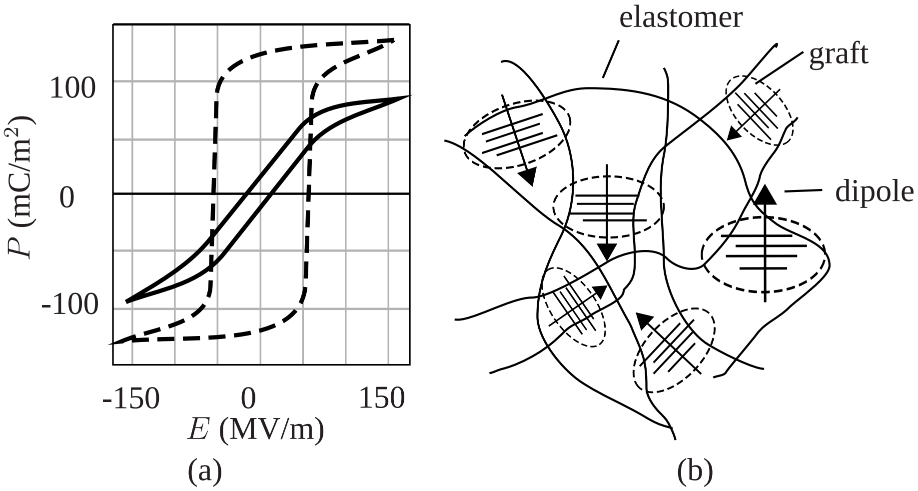

Figure 2.2: (a) Comparison of approximate hysteresis loops for a normal ferroelectric (dashed line) and a relaxor ferroelectric (P(VDF-TrFE)) (solid line) [19]. (b) Illustration of crystallized, polar polymers grafted to a flexible elastomer backbone.

Ferroelectrets

Ferroelectrets represent a class of polymeric actuators characterized by regions of trapped, permanent charge separation. Polymer electrets are made of highly porous polymers, such as polypropylene or poly(ethylene terephthalate), filled with a polarization gas [96]. The pores are typically lens-shaped voids that are formed by filler particles when the polymer is highly stretched. However, the stretching produces flat voids that result in stiff films with low electromechanical response [8]. This is because the electromechanical response is dependent upon the effective modulus of the material, and the effective modulus is dependent upon the relative density [7]. In general, the effective elastic modulus of a cellular material decreases with decreased density roughly as

$$Y_{eff} = Y_0 \left(\frac{\rho}{\rho_0} \right)^2 , \tag{2.3}$$

where Y_0 is the bulk modulus of the material and ρ_0 is the bulk density [31]. However, in ferroelectret cellular films, a minimum in elastic modulus is seen at a relative density between 0.3 to 0.6 [7]. The minimum occurs here because, as the density is decreased by continued gas pressurization, the voids become more spherical, resulting in a higher stiffness. Typical films have elastic moduli in the range of E∼1-10 MPa in the thickness direction [8].

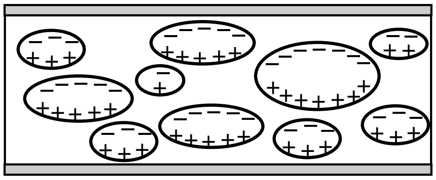

Figure 2.3: Illustration of trapped charge in a cellular polymer foam with bonded electrodes. A voltage applied to the electrodes will cause this structure to compress.

The permanent charge in the pores (see Figure 2.3) is induced by subjecting the porous films to high voltages (>5 kV) that cause dielectric breakdown [12]. The electrical discharges create permanent charge separation at the polymer-gas interface. The trapped charge density can be increased by filling the pores with gases that breakdown at higher field strengths [8].

Polymer electrets have properties similar to piezoelectrics. By attaching conductive electrodes to either side of the films, and applying a voltage, a change in film thickness can be induced. For an optimized film, the piezoelectric coefficient can be d_{33} >600 pm/V in the thickness direction [85]. Ferroelectrets also have a wide bandwidth ranging from a few hertz up to hundreds of kilohertz, making them function well as audio and ultrasonic transducers [85]. The maximum performance of ferroelectrets is governed by the breakdown field. If the actuator is continuously run at high fields, the piezoelectric coefficient will start to degrade [73]. Mellinger et al. found that for porous, polypropylene ferroelectret films of varying thicknesses and cell sizes, breakdown started to occur at a field strength of $\sim$54 V/μm [56].

Dielectric Elastomers

Dielectric elastomer actuators are capacitors that have a compliant dielectric and stretchable electrodes. When a voltage is applied across the electrodes, opposite charges on the electrodes attract each other, compressing the dielectric. However, because the dielectric is incompressible (Poisson's ratio of 0.5), it must expand in the transverse directions. The expansion in the transverse directions is aided by the natural proclivity of the like charges on either electrode to repel each other. This behavior is illustrated in Figure 2.4. The induced stress is called the Maxwell Stress, and can be represented by,

$$P_M = \epsilon_r \epsilon_0 \frac{V^2}{g^2}, \tag{2.4}$$

where ϵ_r is the relative permittivity of the dielectric, ϵ_0 is permittivity of free space, V is the voltage, and g is the thickness of the dielectric. Notice that this is exactly twice the magnitude of the electrostatic stress developed between two parallel plates with rigid electrodes. The factor of two is gained by having electrodes that can expand [12].

For free boundary conditions and strains less than 10%, the change in thickness follows from

Hooke's Law as,

$$S_y = -\frac{P_M}{Y} = -\frac{\epsilon_r \epsilon_0}{Y}\frac{V^2}{g^2}, \tag{2.5}$$

where Y is the elastic modulus of the dielectric and S_y is the strain in the thickness or y-direction. The strain in the transverse directions can be determined from the incompressibility constraint of the dielectric material [68],

$$S_t = (1 + S_y)^{-0.5} - 1. \tag{2.6}$$

Also of importance is the volumetric energy density of the actuator. For a film with free boundary conditions and small strains [66], the energy density is

$$e_a = P_M S_y = \frac{\epsilon_r^2 \epsilon_0^2}{Y}\frac{V^4}{g^4}. \tag{2.7}$$

Another typical metric is the elastic energy density, which is $e_e = 1/2e_a$.

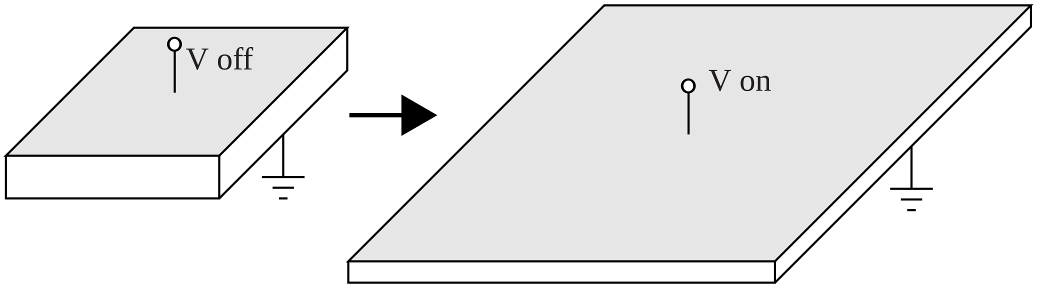

Figure 2.4: Illustration of dielectric elastomer with compliant electrodes compressing in thickness and expanding transversely under an applied voltage.

In practice, the strain of most dielectric elastomer actuators is greater than 10%. In this case, the assumption that g is the initial thickness g_0 no longer holds. For this case, the more complicated solution must be used [68],

$$S_y = -\frac{2}{3} + \frac{1}{3}\left(f(S_{y0}) + \frac{1}{f(S_{y0})}\right), \tag{2.8}$$

where

$$f(S_{y0}) = \left[2 + 27S_{y0} + \frac{(-4 + (2 + 27S_{y0})^2)^{1/2}}{2}\right]^{1/3}, \tag{2.9}$$

and

$$S_{y0} = -\frac{\epsilon_r \epsilon_0}{Y}\frac{V^2}{g_0^2}. \tag{2.10}$$

For the large deformations, the elastic energy density is calculated from [66]

$$e_e = Y[S_y - \ln(1 + S_y)]. \tag{2.11}$$

From these equations it is easy to see that the material properties of the dielectrics are very important to the actuator performance. It is not surprising then, that a lot of effort has been devoted to exploring different elastomers. Elastomers with Young's moduli ranging from 100 kPa up to 4 MPa have been tried as actuator dielectrics [12]. Materials such as polyurethane elastomers, thermoplastic elastomers impregnated with oligomeric oils, and even Dr. Scholl's gelactiv tubing have been tested as potential actuator dielectrics [12]. However, the two most widely used elastomers are still acrylic elastomers and silicone rubbers. Actuators made out of acrylic elastomers, such as 3M's VHB 4910, show the highest strains (380% in area), pressures (7.2 MPa) and energy densities (3.4 J/g) [12]. By contrast, the less viscoelastic silicones have a maximum strain of 63% in area, maximum pressure of 3 MPa and elastic energy density of 0.75 J/g [12].

The high performance values reported for elastomers are generally achieved by heavily prestraining the films (can be as high as 300% in some cases) [67]. The high prestrain enhances the breakdown strength of the materials. This allows an increase in the maximum applied field strength by as much as $\sim$8x in some cases , and in turn increases the energy density. The prestrain can be applied in one or two directions, stiffening the material in those directions and causing the material to preferentially actuate in the lower prestrain directions. Prestraining the material has also been shown to increase the mechanical efficiency and response speed, but it may cause a slight decrease in the dielectric constant [12].

Actuators that use acrylic elastomers suffer from a number of problems because of viscoelasticity. At low actuation speeds and static voltages, acrylic actuators will experience pull-in failures as a result of creep. For a constant applied voltage, the material will continue to thin under the Maxwell stress. As it thins, the electric field continues to increase until the field reaches the dielectric breakdown strength. The viscoelasticity is also responsible for attenuation of strain by as much as 90% at 10 Hz [71]. The pull-in failures and frequency-related attenuations can be partially offset by prestraining the actuator [12]. However, maintaining prestrain requires the use of bulky rigid frames that can significantly lower the energy density because of added weight. This limits the usefullness of prestrained actuators in micro-robotics.

Ha et al. has developed an interesting solution for the prestraining problem in acrylic elastomers [32]. Instead of using a frame to maintain the prestrain, they use an interpenetrating polymer network (IPN). The acrylic is first prestrained. Then, while it is prestrained, a monomer and initiator are sprayed onto the film and allowed to diffuse into the matrix. Next, the monomer is polymerized. When the prestrain is released, the IPN prevents the acrylic from returning to its initial zero-strain state, locking the prestrain into the film. The new material shows performance metrics near that of the mechanically prestrained film, but without the frame.

A problem for both acrylic and silicone elastomers is the need for very high voltages ($>$1 kV). The necessary voltage can be lowered by increasing the dielectric constant, or by making thinner films. Making thinner films is a good solution from the standpoint of maintaining dielectric breakdown strength and loss characteristics. However, thinner films are more susceptible to tearing if any defects are present.

Increasing the relative permittivity allows for higher Maxwell pressures and energy densities at lower electric fields. For pure elastomeric compounds, relative permittivities range from 2-7 [12]. The value can be increased by adding metallic filler particles to the elastomers. For example, Gallone et al. were able to increase the dielectric constant of a particular silicone elastomer from 7, with no particles, up to 24 by adding 30% lead magnesium niobate-lead titanate particles by volume [28]. Other groups have reported relative permittivities in excess of 4000 for polyurethane films loaded with graphite [14]. However, the addition of filler particles has the effect of increasing the elastic modulus, decreasing the ultimate stress and strain, and lowering the breakdown voltage. The lower breakdown strength can be a result of percolation occuring when the film is compressed during actuation. The particles also typically increase the dielectric losses of the material. The best results have been achieved by mixing a silicone elastomer with a highly polarizable polymer, poly(3-hexylthiophene) (PHT) [12, 16]. With a 1 wt.-% blend, a transverse strain of 7.6% with a field of 8 V/μm was achieved compared with only 1% strain at 0 wt.-%. However, this result is somewhat misleading because the added PHT only increased the dielectric constant from 4.6 to 5.6, but the elastic modulus decreased from 100 kPa to 20 kPa. From the Maxwell stress equations, it is clear that the change in modulus outweighed the slight change in dielectric constant.

One of the fundamental components of a dielectric elastomer actuator is the compliant electrode. Because the elastomeric materials are incompressible, a flexible electrode is necessary in order to see any significant strain. Therefore, developing reliable electrodes is another area of intense research. An ideal electrode should maintain high conductivity over large strains, be very compliant, survive repetitive expansion/contraction cycles, and be fault tolerant. The most common electrode materials are metallic paints, carbon grease, and graphite or carbon powders [12]. Carbon greases are the best choice for very large strain actuators because they are able to flow in order to remain continuous over large area changes. The powdered electrodes are easier to handle than the greases, but large strains can separate the particles enough to lose conductivity. The powders are very simple to apply to sticky acrylic elastomers [15].

Solid metal films can be used as electrodes if the surface of the elastomer has an appropriate pattern. Silver and gold films deposited on elastomers with rippled surface patterns have demonstrated strains of 22 to 33% before the film starts to crack [12]. Nanometer-sized clusters of metal ions can also be directly implanted into the surface of PDMS, and can remain conductive at strains up to 175%. This method allows actuators to be selectively patterned, but the patterned regions have an increased elastic modulus of 50-350% [75].

Another option for electrode material are thin layers of CNTs ($\sim$15 nm). CNT films can maintain conductivity at 200% area strains because their high aspect ratio results in percolation at very low concentrations [99]. CNTs are also somewhat robust to dielectric breakdown through the elastomer because, instead of creating a continuous short like carbon grease, the CNTs are burned away at the breakdown site. However, because of the sharp features of the CNTs, high fields can develop at exposed tips, causing discharging through the air. This kind of discharging will eventually degrade the electrodes, and the actuation strain will start to decrease.

The discussion so far has presented the results of actuators under ideal laboratory conditions, most of which do not represent useful actuator configurations. Practical actuators using dielectric elastomers have more modest performance. This is because of the added weight of passive components needed to maintain prestrains, and also because the maximum values reported above can not generally be sustained over numerous cycles without causing damage. Actuator devices either use the area expansion or thickness reduction to generate force outputs. Expansion type actuators include bending (unimorph and bimorph), stretched-frame, diaphragm, bowtie, bow, spider, spring roll and extender. Thickness type actuators include folded, spring and stacked [17]. Some of these actuator configurations are represented in Figure 2.5.

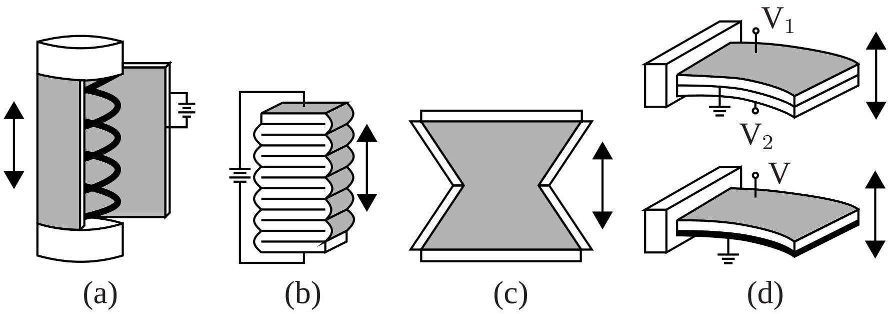

Figure 2.5: A sample of dielectric elastomer actuator configurations. (a) Spring roll actuator with elastomer peeled back to show spring. (b) Folded actuator. (c) Bowtie actuator. (d) Bimorph (top) and unimorph (bottom).

The spring roll and stacked actuators are a couple of the more useful actuator configurations because they can provide high linear strains and forces. The spring roll consists of a spring core and two end caps that hold the elastomer in place. It is fabricated by attaching the rolled elastomer to the end caps while the spring is compressed. Then, when the force is released, the spring provides a prestrain for the rolled film. The force output is set by the number of layers rolled around the spring. This device is capable of producing linear elongation of 31% in the active area and forces of 7.2 N ($\sim$60 kPa) for an actuator 45 mm in length, 12 mm in diameter and weighing 8 g [101]. Spring roll actuators have some problems with reliability because of stress concentrations at the end caps [12]. Patterning of the active area can allow the spring roll to bend by expanding isolated sections.

Stacked actuators use the thickness direction to provide displacement and forces. These devices consist of stacks of thousands of individual films, or a single continuous film folded many times. A linear strain of 10.5% and stress of 3.75 kPa at 10.75 V/μm have been achieved with a folded silicone elastomer [63]. The folded actuator is potentially easier to fabricate than a laminated stacked actuator. This is because in the folded device, there is only one electrode along a continuous strip that is folded up into an actuator stack. With a layered actuator, each individual layer needs to be properly electrically connected to the alternating layer.

2.2.2 Ionic EAPs

Ionic Polymer-Metal Composites (IPMCs)

Ionic polymer-metal composites typically consist of a polymer membrane on the order of 200 μm thick, coated on both sides with thin layers of metal [6]. The polymer membrane is composed of a poly-electrolyte with covalently-bonded, anionic side groups. The negatively charged matrix is balanced by adding mobile cations. When a voltage is applied to the electrodes of a hydrated IPMC, then the cations move toward the negatively charged electrode. The diffusion causes the negative side of the membrane to swell, making the actuator bend toward the anode. The initial diffusion creates a quick bending motion, but this is followed by a slow relaxation as the pressure adjusts. The actuation process is illustrated in Figure 2.6. The relaxation does not necessarily have to be in the unbending direction. For example, the two most widely used membrane materials have opposite relaxation behaviors. For Nafion-based IPMCs neutralized by alkali metals, the relaxation is in the direction of the cathode, and may even go past the starting position. For Flemion-based IPMCs, the relaxation is toward the anode, creating further bending [6].

IPMCs have the benefit of only requiring a few volts (1-3 V) for actuation, and have been shown to produce 3% strain and 30 MPa [12]. The actuation speed is dependent on ionic diffusion, so it can range from a few hertz up to a few hundred hertz. IPMCs have limited applications because they only actuate in a bending mode. However, their ability to work in wet environments has made them useful in swimming robots and medical devices [63].

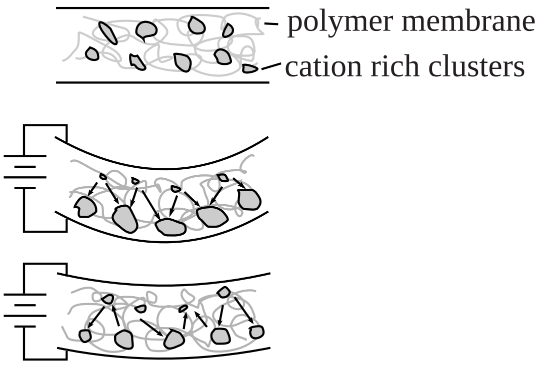

Figure 2.6: IPMC actuation. Top figure is the neutral state. Middle figure is the state just after a voltage is applied to the electrodes, causing cations to move toward the cathode. Bottom figure is after the pressure gradient causes flow towards the anode, relieving some stress.

Ionic Gels

Ionic gels are a type of hydrogel composed of a small fraction of crosslinked polymer filled with an electrolyte solution. Ionic gels are used as actuators by controlling the amount of solution that is absorbed or expelled from the polymer. In polyacrylic acid gels, the swelling is controlled by changing the pH either directly through the hydrating solution or by applying an electrical field. The electric field causes migration of hydrogen ions out of or into the gel, causing a pH change [12]. Actuation under a DC field tends to cause bending because of unequal ion diffusion rates throughout the gel. Because the principal mode of actuation is driven by diffusion, ionic gel actuators respond fairly slowly to stimuli. However, faster actuation may be possible with gels made by electro-spinning nanofibers [81]. The nanofibers offer a much higher surface area to volume ratio, allowing much faster actuation speeds [57].

Ionic gel actuators can be limited by their need to be hydrated. However, Liu and Calvert developed a clever work around that allows polyacrylimide (PAAM) and polyacrylic acid (PAA) to work in air [51]. Normally, when a voltage is applied across a hydrated PAA gel, water is expelled from the material and it contracts. This is not a reversible mode of actuation in air because the water is difficult to recover. Liu and Calvert solved this problem by layering PAA and PAAM gels. When water is expelled from the PAA, it is absorbed by the PAAM, so that when the voltage is removed, the water can be reabsorbed by the PAA. The contraction in area of the stiffer PAA (Y=650 kPa) forces the softer PAAM (Y=390 kPa) to contract as well, and the whole stack increases in thickness. This allows a reversible strain of 10% at 3 V. Unfortunately, the solvent migration is quite slow, taking 1 min to achieve the 10% strain.

Conductive Polymers

Conductive polymer actuators work by reversible redox reactions. The polymer is switched between the reduced and oxidized states by applying a small voltage ($\sim$1-2 V) across a conductive polymer in contact with an electrolyte solution [17]. While the polymer is in the oxidized state, excess charge causes the uptake of ions perpendicular to the polymer chain length [12]. The additional ions cause the polymer to expand. Then, when returned to the reduced state, the extra ions migrate away, allowing the polymer to relax.

Stresses range from 1 to 5 MPa for polypyrrole and polyaniline actuators. Strains range from 1 to 35%, with the highest strains coming from polypyrrole-based actuators [17]. However, while strains of a few percent take a few seconds to realize, maximum strains near 30% can take a few minutes to reach [17]. The mode of actuation is slow because it relies on the migration of ions, and some of the ions are very large and not very mobile. Also, because of the need for electrolytes, conductive polymer actuators need to be immersed in solution, or they must have proper encapsulation. Another notable downside is their very low efficiency of $\sim$1% [12].

2.3 Carbon Nanotubes

Baughman et al. showed one of the first examples of a Carbon Nanotube (CNT) based actuator [9]. Their actuator consisted of an unordered mat of single-walled carbon nanotubes (SWNTs), approximately 15-35 μm thick, immersed in a solution of NaCl. When a voltage ($\sim$1 V) was applied to the device, actuation occurred through an expansion of the carbon-carbon bond length as a result of charge injection (see Figure 2.7). This device achieved a maximum strain of 0.08% at less than 1 Hz [9]. The small strain is due to the fact that SWNTs tend to form bundles, so the bond length is only increased on the outer nanotubes. Maximum strains of 0.7% have been achieved since the initial work, but the theoretical limit of this type of actuator is a strain of 1% because the voltage is limited to ∼4 V before redox occurs in the electrolyte [6]. This material can produce high stresses (elastic modulus ∼1.2 GPa), but is fairly slow with strains severely tapering off at a few hertz [9].

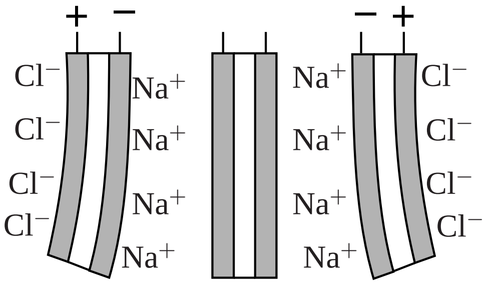

Figure 2.7: CNT actuator in aqueous solution of NaCl. Two gray regions are SWNT sheets bonded together by double-sided tape. The polarity of the applied voltage causes the ions to form a charged double layer on the SWNTs. The charge injection causes mechanical deformations in the SWNTs, making the cantilever bend [9].

CNT sheets pulled from multi-walled carbon nanotube (MWNT) forests can be used as actuators by suspending them over a distant ground plane and applying high voltages (>1 kV) [2]. These low density sheets (1.5 mg/cm^3) change dimensions as a result of repulsion between nanotubes due to charge injection. The thin sheets (∼20 μm thick, 25 mm long, 2 mm wide) expand in thickness by ∼200% and in width by ∼220%. The expansions in width and thickness are accompanied by a small strain in the length direction of ∼1%. Sheets can be densified by wetting them with ethanol and letting them dry. A sheet with a density of 0.8 g/cm^3 can generate a stress of 3.2 MPa in the length contraction direction. CNT sheets are much better at higher frequency than CNT mats, showing 30% strain at 1.1 kHz [2].

2.4 Shape Memory Alloys (SMA)

Shape memory alloy (SMA) actuators work by changing their crystal structure in response to temperature. At low temperatures they have a martensite structure, which is characterized by a monoclinic lattice. In two dimensions, this structure looks like a parallelogram. At high temperatures, the crystal structure changes to a cubic lattice, called austenite. There is hysteresis in the structure change because of internal friction between the two phases. The width of the hysteresis is typically 10-50°C [93].

The shape memory effect is seen when the material is deformed while cool, and then, upon heating, the material returns to its original shape (see Figure 2.8). This ability comes from the crystal structure of the alloy. In the martensite structure, the atoms naturally form rows of parallelograms slanted in alternating directions. The rows can be forced into the same orientation by deforming the structure with low stresses ($\sim$70 MPa) at low temperature. When the material is heated, the structural deformation is relieved, and the undeformed, high-strength austenite structure is recovered, generating stresses between 140 to 345 MPa [23]. However, repeatedly using the higher stresses can cause eventual failure of the material.

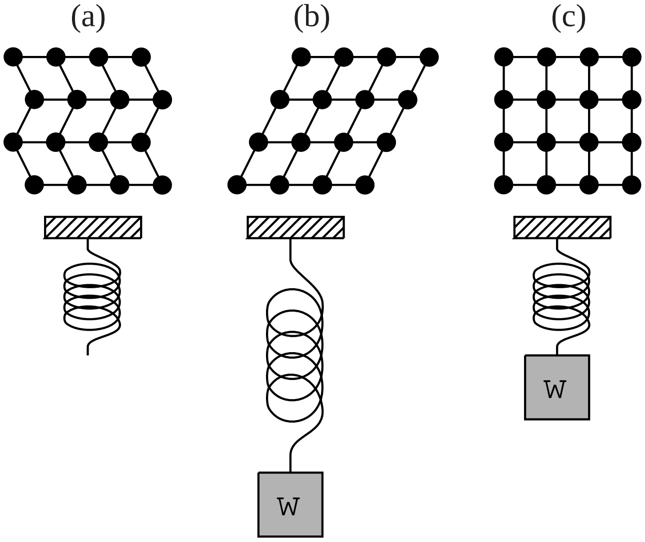

Figure 2.8: Top row shows crystal structure of the material during the different stages of SMA actuator use. (a) SMA spring in low-temperature, undeformed martensite state. (b) SMA spring in low-temperature, deformed martensite state. (c) SMA spring in high temperature austenite state.

There are a few different alloys that show this effect, but the most widely used alloys are composed mostly of nickel and titanium with small percentages of other metals. The nickel titanium alloys are generally referred to as Nitinol. These alloys are popular because they have high ductility, provide more recoverable motion, have excellent corrosion resistance, have stable transformation temperatures, have high biocompatability, and are able to be electrically heated for shape recovery [93].

Electrically actuated SMA works by resistive heating caused by passing current through the material. Because this is a thermal process, the actuation is fairly slow in ambient conditions ($\sim$10 Hz). The actuation speed can be increased by actively cooling with water or compressed air. Actuators with smaller dimensions also heat up and cool down faster. As a result, most actuators are made with thin wire, 25 to 500 μm in diameter, or thin films. The material strain recovery for nickel-titanium alloys has a fundamental limit of 8%. If the material is strained more than 8% in the martensite state, then dislocations will form and prevent full shape recovery. For actuators that will be used over multiple cycles, the strain should be kept between 4 to 5% [23]. To build up large displacement, SMA wire is usually shape set at high temperatures into a helical spring. The spring can then be used as either a contraction or extension actuator by stretching or compressing it, respectively, in the low temperature state.

The amount of current required to heat an SMA actuator above its phase transition temperature ($\sim$100°C) is dependent on actuator dimensions, ambient temperature and the properties of contacting materials. As an example, a 150 μm diameter wire at room temperature requires 400 mA to contract in 1 second, whereas a 25 μm diameter wire only needs 45 mA to contract in 1 second [23]. Higher currents can be applied to the wires to increase actuation speed, but this runs the risk of overheating the wire or reaching stress limits because of inertial effects from the load.

2.5 Thermal Actuators

Actuators can be fabricated by taking advantage of thermal expansion in a single material, or the thermal expansion mismatch between two different materials. Any block of material that changes dimensions upon heating can be used as an actuator. The change in length of a solid bar is

$$\delta L = L\alpha\delta T, \tag{2.12}$$

where L is the length, δT is the change in temperature, and α is the thermal expansion coefficient. The blocked force is then

$$F = YA\alpha\delta T, \tag{2.13}$$

where A is the cross sectional area [47]. For a centimeter cubed piece of aluminum (α=24 μm/(m·K) and Y=68 GPa [55]) subjected to a temperature change of 200K, the change in length is 48 μm or 0.48% strain, and the force is 32.6 kN or 326 MPa. This type of actuation can produce very large stresses, but the strains are fairly small. Higher displacements can be achieved by using a bimaterial cantilever configuration and taking the bending deflection as the output. Thermal actuation also suffers from slow recovery times because of the time necessary to cool the material. Efficiencies are also low because a lot of heat energy is lost to the environment. As a result, this simple mode of actuation does not represent a very practical artificial muscle technology.

2.6 Magnetic Actuators

2.6.1 Electromagnetic

Magnetic actuators rely on two primary mechanisms to generate forces and displacements. These are electromagnetism and magnetostriction. Electromagnetic actuators are typically composed of some configuration containing a current-carrying wire and a permanent magnet. The current carrying wire generates a magnetic field that interacts with the permanent magnet to generate a force. This is the mechanism behind electric motors. However, we will not consider electric motors here because they are size limited. An example of a linear electromagnetic actuator is the voice coil found in speakers. A voice coil is composed of current-carrying wires wrapped around a spring-supported magnet. The direction of the current flow can be changed to either repel or attract the magnet. Voice coils can have strains up to 50% and generate pressures in excess of 100 kPa with high effiencies [12]. However, electromagnetic actuators have the drawback of having constant power dissipation during static holds. This is because the coils must be supplied continuous current in order to maintain the magnetic field.

2.6.2 Magnetostrictive

Magnetostrictive actuators work through a change in material properties in the presence of a magnetic field. Magnetostrictive alloys have a reversible change in dimension when their internal magnetic domains align with a magnetic field. Pure nickel and iron contract with an applied field, but they only show strains of $\sim$0.003%. Rare earth materials, such as the popular Terfenol-D ($Tb_{0.27}Dy_{0.73}Fe_{1.9}$), expand in a magnetic field with a strain of 0.2%, a stress of 70 MPa and an energy density of 15-24 kJ/m^3 [25, 39]. Magnetostrictive actuators are fabricated by winding a wire around a cylinder of the alloy. Achieving maximum strains requires high magnetic fields, 100 kA/m, which leads to high resistive losses in the coils and thermal dissipation problems [39].

2.7 Electrostatic Actuators

2.7.1 Parallel Plate Actuator

Electrostatic forces have been used to create a number of different types of actuators. The most simple of these is the parallel plate actuator, shown in Figure 2.9, which consists of two conductive plates separated by a dielectric and supported by some spring elements. When opposite charges are applied to the plates, the attraction causes the plates to move together. The electrical energy stored in this system is

$$e = \frac{1}{2}CV^2, \tag{2.14}$$

where C is the capacitance and V is the voltage potential. If the fringing fields are neglected, the capacitance for a parallel plate configuration is

$$C = \frac{\epsilon A}{g}, \tag{2.15}$$

where A is the area of the plate, ϵ is the permittivity of the dielectric, and g is the plate separation. The force is given by

$$F = -\frac{\partial e}{\partial g} = \frac{\epsilon A V^2}{2g^2} = \frac{\epsilon A}{2}E^2, \tag{2.16}$$

where E is the electric field. Finally, the electrostatic pressure is

$$P = \frac{1}{2}\epsilon E^2. \tag{2.17}$$

It is apparent from these equations that the performance of electrostatic actuators is highly dependent on the gap spacing. As was seen with dielectric elastomer actuators, large voltages are necessary if large gaps are used, so gap spacing should be minimized.

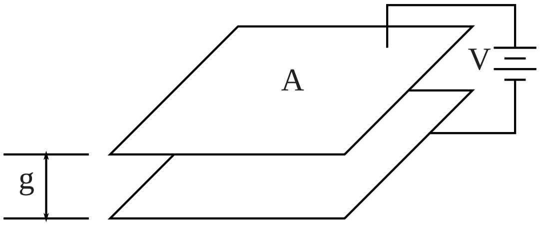

Figure 2.9: Parallel plate actuator.

Parallel plate actuators have found a number of uses as integrated components in silicon-based, opto-electronic devices [34] and high speed relays [59]. Silicon micro-machining techniques allow precise control of small gap spacings necessary for low voltage actuation. However, these particular silicon-based devices are not immediately applicable to artificial muscle applications because they are dependent upon bulky support structures, and they can only output forces of micronewtons over distances of micrometers. In order to be useful as a robotic actuator, it is necessary to put the actuators in series to scale up force and displacement to usable levels. A few examples of scaled up devices are present in the literature [11, 58]. These devices are composed of alternating, flexible electrodes joined by rigid elements. When a voltage is applied to the structures, they collapse in one direction, generating linear actuation.

Integrated Force Arrays (IFAs) created by Bobbio et al., shown in Figure 2.10(a) [11], is a device fabricated in the plane using micro-fabrication techniques. This results in an actuator sheet composed of numerous (1.5 million elements) very thin plates (2 μm). This device can generate an electrostatic pressure of ~8.2 kPa with an overall strain of 11% at 100 V [43]. The maximum strain possible in an actuator composed of many cells is

$$S = \frac{t_g + 2(t_m + t_p)}{2(t_g + t_m + t_p)}, \tag{2.18}$$

where t_g is the air gap size, t_m is the metal thickness and t_p is the plate thickness. If the metal and plate thicknesses are made very small, the strain approaches a maximum of 50% because of the rigid supports. The actual structure only achieved 11% strain because not all of the cells were working properly. The theory also shows that the plates will come into contact at small voltages because of pull-in. Pull-in occurs when the electric field starts increasing more rapidly than the mechanical restoring force, causing the plates to snap together. However, this leads to hysteresis in the actuation. Jacobson et al. predicted that for a given geometry, the pull in voltage should be 35 V, but the plates will not separate until the voltage is reduced to 8 V [43].

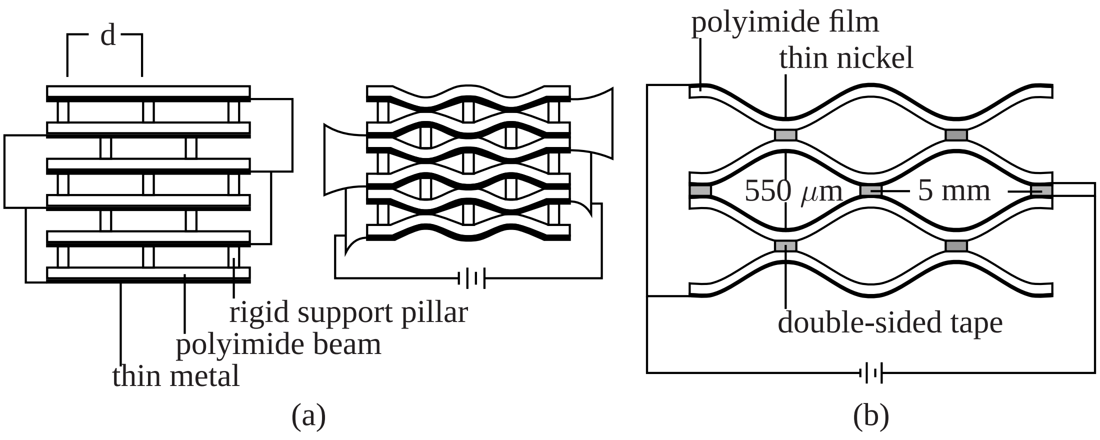

Figure 2.10: (a) Integrated force array. The polyimide beams are $t_p = 0.35$ μm thick, the metal layers are $t_m = 30$ nm thick, and the air gap between beams is $t_g = 1.2$ μm thick. The support spacing is $d = 22$ μm long. This actuator is only 2 to 4 μm thick into the page [11, 43]. (b) Macroscale, distributed electrostatic micro actuator. This actuator is composed of flexible 7.5 μm thick polyimide film coated with 12.5 nm of nickel. The double-sided tape is 25 μm thick. This actuator is 28 mm thick into the page [58].

Minami et al., created a similar structure to the IFA, called the Distributed Electrostatic Micro Actuator (DEMA), shown in Figure 2.10(b) [58]. They built the actuator at both a centimeter scale by stacking up metalized films, and a millimeter scale by using photolithography and electroplating. The macro model showed strains of 36% at 200 V (force was not measured). The structure in the macromodel takes advantage of very compliant films, and a variable gap spacing that allows the plates to zipper together. This is how they achieve large strains at low fields (E $\sim$0.36 V/μm in the center of the cells where the gap is $\sim$550 μm). The microscale model had less than $\sim$1% strain at 200 V, and an estimated stress of $\sim$420 Pa [58]. Even though the microscale actuator has smaller gaps (15 μm), it produces a much lower strain because of the higher stiffness of the metal structure.

2.7.2 Comb Drive Actuator

Comb drive actuators, shown in Figure 2.11, are another type of electrostatic actuator widely used in silicon devices. They are popular in MEMS because, for a given voltage, their force output remains constant with displacement, unlike parallel plate actuators. This greatly simplifies displacement control. Also, they experience less air damping than parallel plates and provide larger strokes [88]. If we examine a single finger of a comb drive, and we ignore the fringing fields, the capacitance between the inner finger and the outer fingers is

$$C = \frac{2\epsilon h x}{d} \tag{2.19}$$

where h is the height of the finger, x is the finger overlap, and d is the gap between fingers. As we did with the parallel plate actuator, we differentiate the energy with respect to the change in displacement to get the force,

$$F = \frac{\partial e}{\partial x} = \frac{\epsilon h}{d} V^2. \tag{2.20}$$

This force comes from the fringing fields at the tip of the finger drawing the finger in. For multiple fingers, the force scales linearly with finger number (number of single fingers with two fingers on each side). From this equation, we notice that the force is dependent on the gap between the fingers, and is proportional to the height of the fingers, which is representative of the overlap area. Also, as previously stated, the force is not dependent upon the displacement in x, meaning that there is no concern about pull-in instabilities. Comb drives typically have forces in the micro- to millinewton range, and displacements from 1 to 100 μm [102]. The corresponding stresses are in the kilopascal range, with operating frequencies in kilohertz range. In order to become a practical muscle-like actuator, work needs to be done on the suspension so that actuators can be placed in series to achieve high displacements. Alternatively, large overall displacements may be possible by using comb drives in conjunction with ratcheting mechanisms [10].

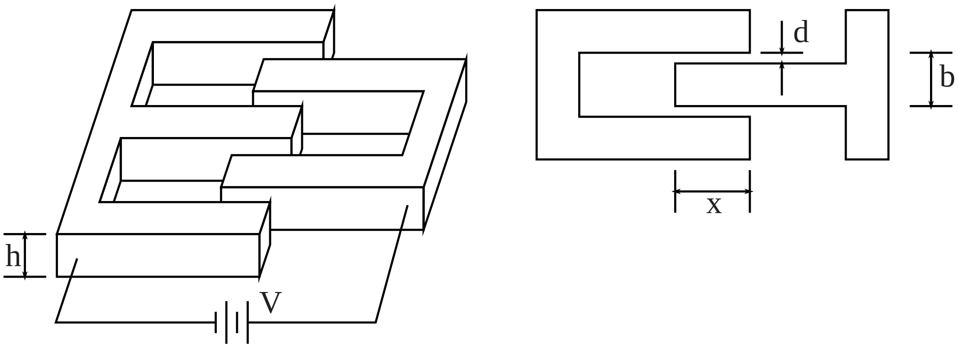

Figure 2.11: Comb drive actuator shown at an angled perspective, and detail of a single finger from the top view.

2.7.3 Electrostatic Induction Linear Actuator

Another type of electrostatic actuator is the electrostatic induction motor [61]. This is a linear actuator composed of a stator film and a slider film, shown in Figure 2.12. The stator film has a repeating pattern of parallel three-phase electrodes embedded in an insulating film [61]. The slider has an insulating layer backed by a high resistance coating. As positive and negative voltages are sequentially applied to the stator phases, an opposite charge is induced on the slider film. Because the slider has high resistivity, the charges are slow to decay. The stator phases are powered in a sequence that alternates between repulsion and attraction with the slider, causing the slider film to move with respect to the stator. The sheets can be made arbitrarily long to achieve specific stroke lengths, and they can be stacked in parallel to increase the available force. Linear sliding forces of 6 N/m^2 (force over total electrode area) have been achieved with a 12 μm thick film operating at a speed of 420 mm/s and ± 750 V [24].

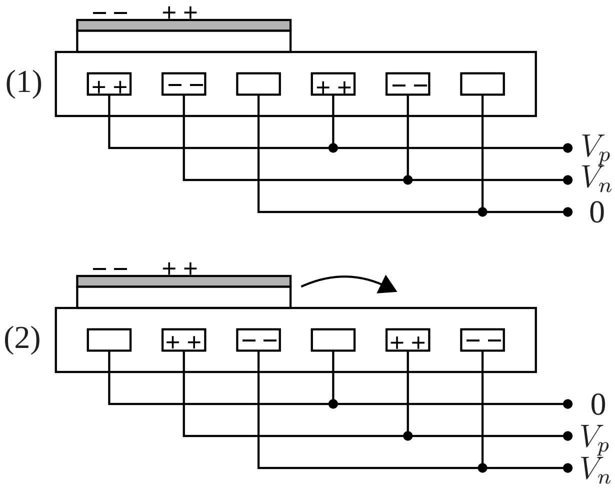

Figure 2.12: Linear induction motor. In (1) charges are induced on the slider by the rotor. In (2) the charge on the rotor is switched, causing it to repel the slider and force it over by one step.

2.8 Concluding Remarks

There is clearly no shortage of small-scale actuator technologies. However, not all actuators are equal as Table 2.1 clearly shows. Each type of actuator has a specific use where it excels, but there is not a good candidate for an all-purpose general actuator for small-scale robots. Some actuators are speed limited due to thermal (SMA) or ionic transport (IPMCs) issues. Other actuators are strain limited because they rely on crystallographic conformation changes (piezoelectric ceramics and SMA). Finally, some have limited lifetime and require bulky support structures (DEAs).

Electrostatic actuators can have fast response times ($>$1 kHz) that are typically limited by the mechanical properties of the suspension and the load (mass and stiffness). They can also have high strains. For a parallel plate actuator operating in compression, the strain could easily be $>$ 50%. Electrostatic actuators with rigid electrodes also generally have long lifetimes. Take for example, MEMs resonators that are continuously cycled at thousands of hertz for years. Stress and energy density can also be quite high if sufficiently small gaps are used. As will be shown in the next chapter, it may be possible to create an actuator capable of generating $>$17 MPa if the gap is below $<$1 μm.

The properties mentioned for electrostatic actuators are very appealing, but the challenge lies in creating a self-contained actuator device. MEMs structures require external supports that limit their uses to on chip actuation. DEAs are a type of monolithic, electrostatic actuator, but they fall short of ideal performance because of the dielectric elastomer material. The material introduces a number of problems, such as creep and electrode failures. However, the idea of having the dielectric also serve as a suspension is a great one. The following chapters will explore possible sandwiched suspensions that have a zero Poisson's ratio to allow the use of robust rigid electrodes and materials with low viscoelasticity. This will facilitate the development of low-density, energy dense actuators with high maximum stress and strain.

Chapter 3

Design and Modelling of Electrostatic Actuator

Any electrostatic actuator is composed of three fundamental pieces: the dielectric, the suspension and the electrodes. There are a number of choices for each of the components depending on the application. However, for all actuators some of the important considerations are energy density (both by volume and by mass), efficiency, force, strain and lifetime. For small-scale robot applications, the energy density is of particular importance because of size, power and weight limitations. The following sections will explore the design considerations for each component of the actuator so that these values are maximized.

To make this task tractable, we will only consider two example suspension designs and two example electrode designs. The two prospective suspensions are angled fibers and porous foam. They are chosen for examination because they both have small Poisson's ratios, and therefore allow the use of rigid electrodes. As already stated, rigid electrodes will contribute to the robustness of the actuator. The two suspensions are also purposely chosen to have a low density and fit between the electrodes, thereby limiting their impact on the actuator volume and mass. Because they are between the electrodes, they also act as the dielectric, so their impact on the breakdown strength must be considered.

The two electrode configurations that are examined, parallel plate and comb drive, were chosen because of their compatibility with the suspensions, and because they both have desirable but distinctly different performance advantages. For example, the comb drive provides a linear force-voltage relationship, but the parallel plate electrodes have a higher elastic energy density.

3.1 Dielectric

In the two suspension designs considered, the dielectric is a combination of the support structure material and a gas. This mixture will determine the maximum allowable electric field before breakdown and the dielectric losses.

3.1.1 Dielectric Breakdown in Air

Electrostatic actuator performance is dependent upon the electric field. Therefore, the maximum safe electric field is one of the limiting factors for electrostatic actuation. If the dielectric is a gas, electrostatic discharge may occur either through avalanche breakdown or as a result of field emission. The breakdown strength depends on the gas, so it may be desirable to use gases with a high breakdown strength. However, this will introduce the need for encapsulation. For air, the breakdown field is 3 V/μm under normal conditions [33]. However, because the molecules in air are free to move around, this value is influenced by the mean free path of the particles. In order to cause avalanche breakdown, electrons must gain enough energy so that they ionize the atoms that they collide with, initiating a cascade of current flow. The Paschen effect predicts that there is a minimum breakdown voltage when the gap gets small enough to prevent electrons from building up the necessary energy to cause breakdown. The Paschen equation is given by

$$V_b = \frac{Bpy}{\ln{(py)} + k}, \tag{3.1}$$

where p is the gas pressure, y is the gap between electrodes, and B and k are experimentally determined constants that depend on the gas and electrode material used [40]. For air with platinum electrodes, $B = 2737.5$ V/(kPa·cm) and k depends on the value of py ($k = 2.0583(py)^{-0.1724}$ for 0.0133$\leq$ py $\leq$0.2 kPa·cm, $k = 3.5134(py)^{0.0599}$ for 0.2$\leq$ py $\leq$100 kPa·cm, and $k = 4.6295$ for 100$\leq$ py $\leq$1400 kPa·cm) [40]. For the given constants, there is a minimum voltage of $\sim$330 V when $py = 0.14$ kPa·cm, corresponding to a gap of 14 μm at a pressure of 1 atmosphere (101 kPa), or an electric field of 24 V/μm.

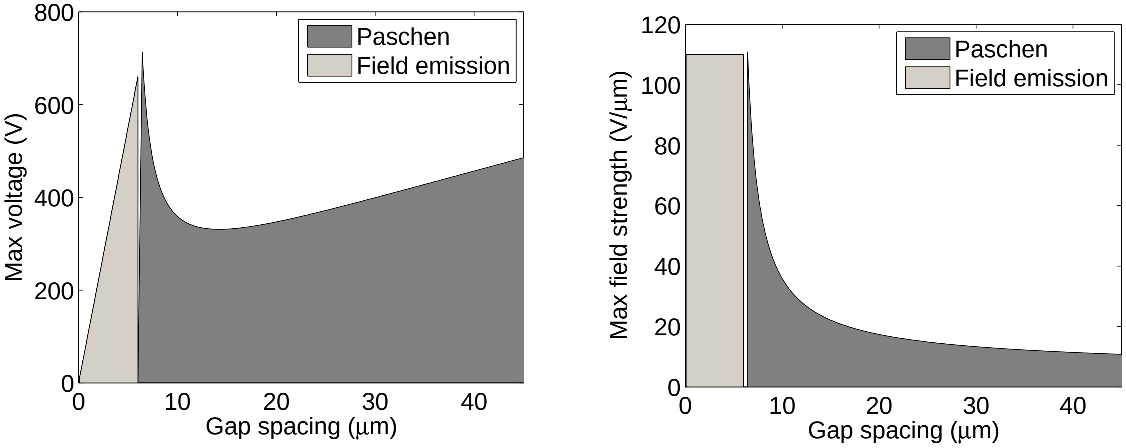

(a) (b)

Figure 3.1: Electrical limits based on Paschen effect and field emission in air. (a) Maximum voltage versus gap spacing. (b) Maximum field strength versus gap spacing. The shaded regions denote the safe design limits.

The Paschen model predicts that after the minimum voltage, the breakdown voltage increases sharply because the mean free path of air is on the same order as the gap size. However, experimental data shows that this effect is only valid for a small range of gap sizes. Eventually, the breakdown voltage actually decreases rapidly because of the onset of field emission. Slade found that as an iron needle approached a silver electrode, the Paschen effect lost relevancy when the gap reached 6 μm [82]. After this point, the breakdown voltage was linear with gap spacing, g,

$$V_b = Kg, \tag{3.2}$$

where K is an experimentally determined constant. For the particular case examined by Slade, K was between 65 and 110 V/μm. This constant represents the maximum electric field for gaps less than 6 μm. The K value will be dependent on the electrode material used and the surface roughness, but the reported values provide reasonable estimates. Figure 3.1 shows the complete breakdown limit as a function of gap size.

The work by Slade had a needle approach a bare electrode with an air gap in between. Other researchers have shown that the dielectric breakdown strength can be further increased by applying a thin insulator on atomically flat electrodes. Horn and Smith were able to achieve field strengths up to 2300 V/μm with silver electrodes coated in mica and silicon, and having an air gap less than 1 μm [36]. However, the maximum field decreased to 600 V/μm as the gap was increased to 3 μm. This value is higher than those reported by Slade due to the insulating layers and the atomic roughness of the surfaces. Any roughness can lead to charge concentrations that initiate breakdown [82]. The configuration of electrode-insulator-air-insulator-electrode is similar to the composition of actuators proposed in this document. Therefore, it is likely that the maximum electric field strength and electrostatic forces of an ideal actuator with nanometer-scale gaps and atomically-smooth, insulated electrodes could be quite high (> 500 V/μm and > 1.1 MPa).

3.1.2 Dielectric Breakdown in Porous Material

The breakdown strength of dielectrics that are a combination of air and solid insulators also needs to be examined because a number of the proposed designs consider such hybrid dielectrics as support structures. In dielectrics composed of a combination of air and solid material, such as foam, the dielectric breakdown limits are less straight forward to calculate than in either individual case. Typically solid materials have a much higher breakdown strength than air. For instance, in polymers the dielectric field strength ranges from 700 V/μm for low-density polyethylene up to 1200 V/μm for poly(methyl methacrylate) [42]. The large range is due to material properties such as molecular weight, crystallinity, and molecular polarity.

Researchers have shown that the introduction of gas filled voids lowers the dielectric breakdown strength of a solid material, with higher porosity leading to lower strengths [30, 56]. The size of the pores and their distribution determines how much the field strength is lowered [3]. Smaller pores have less of an effect than larger pores, as would be expected from the discussion in the previous section. However, the dielectric strength of a porous material is not simply the field strength of the largest pore as predicted by the Paschen effect. Mellinger and Mellinger disproved this hypothesis by looking at porous polypropylene [56]. In their experiments, they showed that the breakdown strength greatly exceeded the value predicted by the Paschen effect. For example, in a polypropylene foam with a maximum void size of 7.5 μm, the expected breakdown strength of an equally sized air gap was predicted to be $\sim$47 V/μm, but the actual field strength of the foam was $>$100 V/μm. One possible explanation for this effect is that the thin polymer walls of the cells provide a barrier that arrests avalanche breakdown. While the field may be high enough to initiate breakdown within the void, extra energy is necessary to continue the breakdown through the solid dielectric [42]. The cascade will have an easier time propagating if there is a high concentration of voids. This is verified by Gerson et al. who showed that regions with many pores will have lower strengths than more solid regions [30].

An absolute theory to describe this phenomenon is not available because of the numerous material and geometrical considerations. However, the experimental work done in this area shows that the maximum field strength for systems with hybrid air/solid dielectrics is generally higher than those predicted for air only.

3.1.3 Dielectric Losses

Even if full breakdown does not occur, losses can still arise because the dielectric material is not a perfect insulator. The loss can be modeled as a parallel RC circuit, where the capacitor is treated as ideal and the resistor represents the losses [78]. The capacitance value is

$$C = \frac{\epsilon' A}{g}, \tag{3.3}$$

where ϵ' is the dielectric constant ($\epsilon' = \epsilon_r \epsilon_0$) at frequency ω, A is the area and g is the gap size. The parallel resistance is

$$\frac{1}{R} = \frac{(\sigma_e + \omega\epsilon'')A}{g}, \tag{3.4}$$

where σ_e is the conductivity of the dielectric and ϵ'' is the loss factor.

Another typical way of representing the loss is by using the loss tangent, also called the dissipation factor [76],

$$\tan\delta_e = \frac{\epsilon''}{\epsilon'} = \frac{\sigma_e}{\omega\epsilon'}. \tag{3.5}$$

Air has a very small conductance, so it's loss tangent is near zero [76]. Certain polymers also have low dissipation factors. For instance, polyethylene ranges from 0.00003-0.00015 at kHz frequencies [74]. In the structures proposed, dielectric losses should be minimal since the dielectric is composed of a mixture of air and good insulating materials, such as thermoplastics.

3.2 Suspension

To achieve the maximum elastic energy density requires a structure that can have 100% strain. This is not very practical in terms of a realistic actuator because, no matter how thin the electrodes are, they will still have some finite thickness that must be taken into account. However, strains close to 100% can be achieved in some regions of an actuator that has very thin, compliant support structures located at the edges of the actuator. Although, having isolated supports limits the actuator to small areas or thick electrodes in order to avoid problems with uneven stress concentrations, localized pull-in failures and adhesion problems that could lead to hysteresis.

A better approach is to have distributed support structures. The supports can either be rigid or compliant, depending on if the electrodes are rigid or compliant. The structures from Bobbio et al. [11] and Minami et al. [58] are examples of rigid supports with compliant electrodes. Having rigid supports limits the maximum allowable strain of the actuator to be less than 50%, as shown in Section 2.7.1. Having flexible electrodes also results in non-uniform electrostatic forces and displacements across the plates for a fixed voltage. This can limit the elastic energy density because voltages need to be kept below the dielectric breakdown field strength for whichever region has the smallest gap. Therefore, the regions with small gaps will have the maximum energy density, but the nearby regions may be less optimal.

Dielectric elastomer actuators are an example of a system with compliant supports and compliant electrodes. The compliant support is the solid dielectric elastomer layer, and the compliant electrodes are composed of carbon powders, greases or carbon nanotube sheets. Because the elastomer is incompressible, it expands in area as it compresses in thickness. Therefore, the compliant electrodes are a necessity rather than a design choice. The ability to stretch allows for a factor of two improvement in the electrostatic pressure over solid electrodes, but this advantage is outweighed by the problems that arise from unreliable compliant electrodes.

The final option is an actuator that uses compliant supports and rigid electrodes. This option is appealing because rigid electrodes are generally more robust than the compliant alternatives used in dielectric elastomer actuators. Also, solid electrodes allow easy fabrication of stacked actuators in order to increase stroke length, and they provide stable surfaces for force outputs and electrical connections. Compliant supports offer the potential for strains in excess of 50%, as will be shown in the following sections.

While completely rigid electrodes (rigid in bending and stretching) can be advantageous compared to completely flexible electrodes (compliant in bending and stretching), there may be a middle ground where adding some flexibility to the electrodes could generate added functionality without degrading robustness. For instance, a continuous, thin metal film can not tolerate large stretching motions, but it could still function under bending. This could allow for actuators that can wrap around cylindrical surfaces. Discontinuous, patterned sheets could also provide flexibility, and produce surfaces that are continuously deformable through control of isolated actuator regions.

In order to allow the use of rigid electrodes, the distributed support ideally needs to have a Poisson's ratio of zero, so that motion is not restricted by the electrodes. This can be accomplished

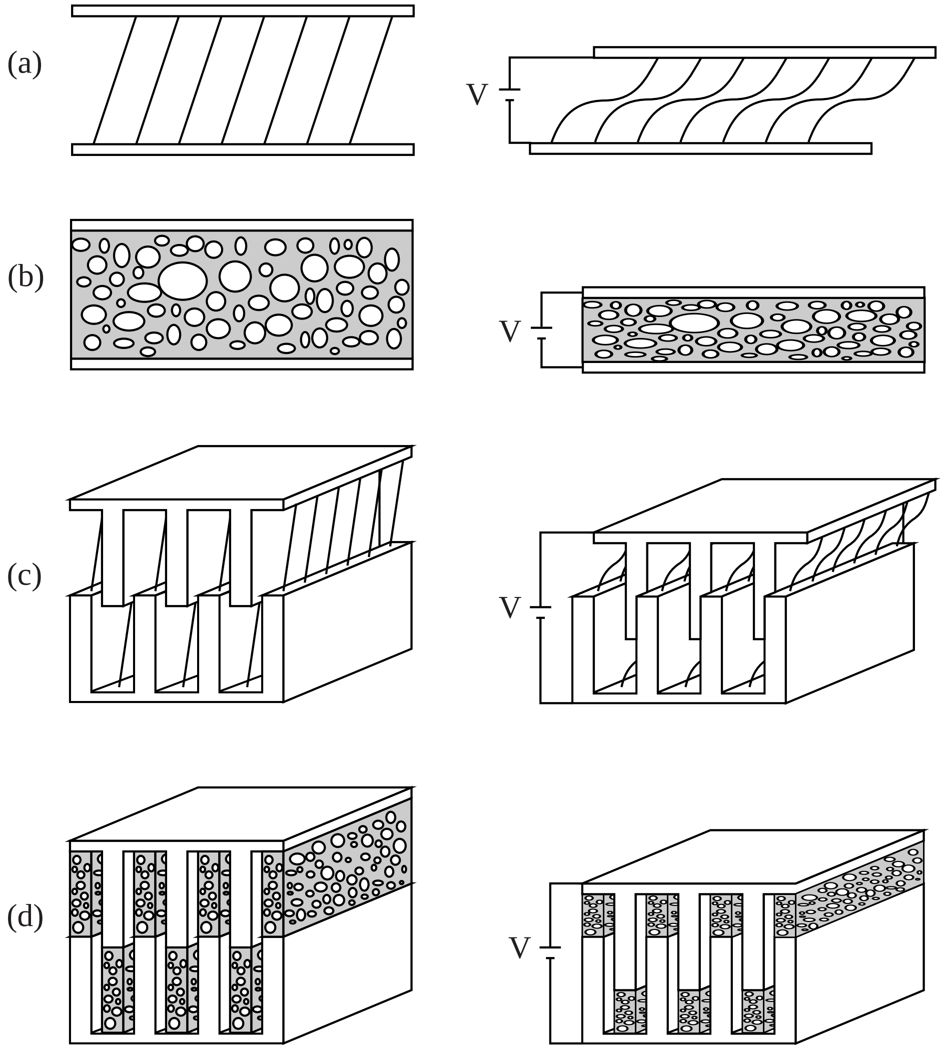

Figure 3.2: Electrostatic actuators using angled fibers and porous foam as support structures. (a,b) Parallel plate. (c,d) Comb drive. Drawings on left side show the actuators in their default state, and drawings on the right show the actuators compressing under electrostatic pressure.

by using either porous materials or arrays of discrete spring elements. Figure 3.2 has drawings showing how either support element could be used in parallel plate or comb drive actuators. The behavior and expected performance of either option are explored in detail in the following sections.

3.2.1 Ideal Stiffness

Before analyzing the suspensions in detail, it is useful to take a step back and consider the ideal stiffness desired from a suspension. With both suspension designs, it is possible to adjust the magnitude of the stiffness, and also to decide whether it should be linear or non-linear with displacement. The type of spring will affect the stability of the actuator and the power output.

Stability

First we consider the stability of of the system. Figure 3.3(a) shows the electrostatic force plotted with the spring force for the system shown in Figure 3.3(b). The units are arbitrary because we are just interested in the shape of the curves. The electrostatic force is

$$F_e = \frac{1}{2}\epsilon A \left(\frac{V}{g}\right)^2, \tag{3.6}$$

where ϵ is the permittivity, A is the area, V is voltage and g is gap size. The spring force is

$$F_s = k(g_0 - g) \tag{3.7}$$

for a linear spring, where g_0 is the initial gap size. For a buckling spring, the force is

$$F_s = \left\{ \begin{array}{ll} k_1(g_0 - g) & \text{for} \quad g \geq g_c \\ k_1(g_c - g) + k_2(g_0 - g_c) & \text{for} \quad g < g_c \end{array} \right\}, \tag{3.8}$$

where g_c is the buckling transition.

In Figure 3.3(a), the closed dots represent unstable points and the open dots represent stable points. The unstable points mark positions where, if the electrode is displaced any further, the spring restoring force will be smaller than the electrostatic force, so the plate will collapse to zero gap. The stable point marks the equilibrium position for the specific voltage. This is the position where the spring force and the electrostatic force balance. As the voltage is increased, eventually there will only be one crossover point between the electrostatic force and the spring force. This point represents the pull-in voltage. For the linear spring, it is found to be [78]

$$V_{PI} = \sqrt{\frac{8kg_0^3}{27\epsilon A}}. \tag{3.9}$$

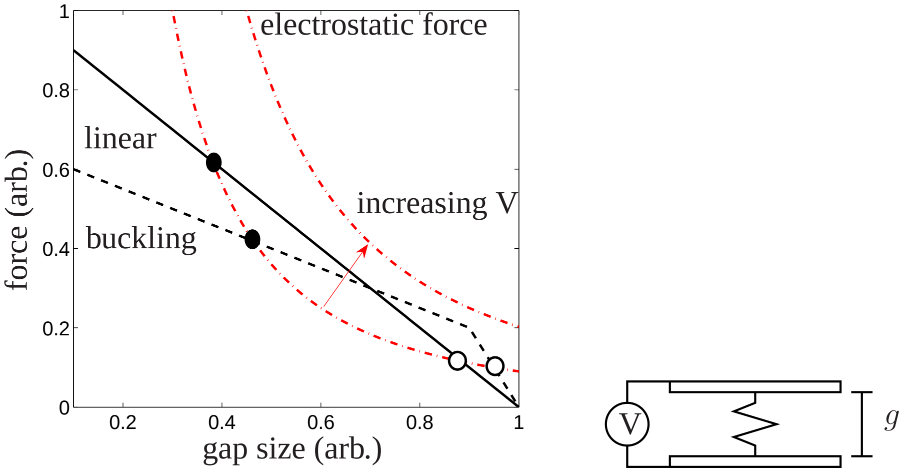

(a) (b)

Figure 3.3: (a) Spring force for linear spring and buckling spring plotted with electrostatic force for a parallel plate actuator with arbitrary units. The filled dots are unstable points and the open dots are stable points. The arrow shows the direction of increasing voltage. (b) Illustration of spring between parallel plates.

The pull in voltage corresponds to a gap size of

$$g_{PI} = \frac{2}{3} g_0. \tag{3.10}$$

For the buckling spring, the pull-in voltage will occur when $g = g_c$ if $g_c < 2g_0/3$, corresponding to a voltage of

$$V_{PI} = \sqrt{\frac{k_1(g_0 - g_c)g_c^2}{\epsilon A}}. \tag{3.11}$$

Otherwise, it will have the same pull-in voltage as the linear spring.

Static Operation

For static operation, the linear spring will provide a larger range of stable displacements, unless $g_c < 2g_0/3$, in which case they provide the same general behavior. However, a buckling type spring might be advantageous in situations where the actuator needs to be very stiff until a critical voltage is applied.

In theory it is assumed that the plates will collapse to zero gap, but in reality this is not the case. This is because the spring will have some finite volume that will eventually act as a hard stop for the plate. If the springs were designed to withstand the full collapse without plastically deforming, then the actuator could be used to provide a fast, stepping motion. Then, if a number of actuator layers were stacked, and if each layer were controlled separately, it could create a large linear actuator with discrete stepping motion. A patterned sheet of this type of actuator might make an interesting topological display.

Dynamic Operation

The full dynamic model will be discussed later, so for now, we will just mention a few brief spring stiffness considerations for dynamic operation. As the stability plot showed, the voltage determines the stable point of operation for the actuator. If we assume that the operating point is set by a DC offset voltage, and that the system is excited about this position by an AC signal. Then, if the spring is truly linear, the displacement will be very easy to predict. However, if this system is nonlinear, then the AC excitation could lead to undesirable behavior. Also, in a resonant mechanical system, the spring and the mass determine the resonant frequency of the system. As the spring stiffness is increased, the frequency also increases and vice versa. If the spring is non-linear, then the resonant frequency will change depending on the operating point. This could be a desirable trait if multiple resonant frequencies are required for a single system. Besides resonance, the spring is also important for impedance matching. When the actuator is driving a load, the maximum power transfer occurs when the impedance of the load matches the impedance of the source. Being able to control the spring stiffness to help match the load is important. Once again, having a non-linear spring complicates this procedure because the impedance will not only be a function of frequency, but also the operating point.

3.2.2 Viscoelastic Losses

Another consideration for suspensions are the loss mechanisms. The loss mechanisms will determine the damping of the structure. The main losses in the suspension will originate from material properties. Specifically, viscoelastic damping may be significant for certain materials, such as elastomeric foams.

The mechanical analog of dielectric loss is viscoelastic loss. Viscoelastic loss arises from internal friction as a material deforms [78]. Viscoelasticity is a property of all materials, however, for some materials, such as metals and quartz, there is little noticeable deviation from linear elasticity at room temperature [49]. However, if suspension elements are made from polymer materials, then viscoelasticity needs consideration.

Linear viscoelasticity can be modelled as a combination of springs and dashpots. The spring represents the linear elastic part of the material response, while the dashpot is the viscous component. Figure 3.4 shows some of the possible combinations and their displacement behavior over time for a constant force. The slow increase in displacement under a constant force is referred to as creep.

The parallel combination shown in Figure 3.4(a) is known as the Voigt-Kelvin model [49]. This model is characterized by a slow increase in the displacement from the instant of initial loading.

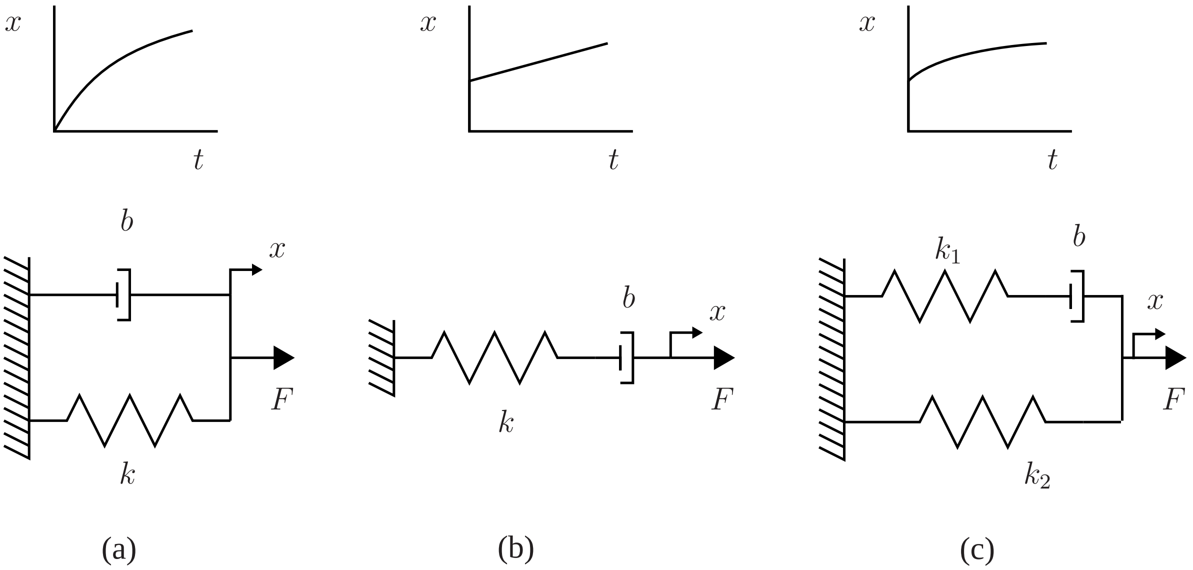

Figure 3.4: Models for linear viscoelasticity in a material, and plots showing approximate displacement behavior for a constant applied force. (a) Voigt-Kelvin model. (b) Maxwell model. (c) Combined Voigt-Kelvin and Maxwell model called the Standard Solid [72]

The differential equation describing this model is

$$\dot{x} = \frac{1}{k}\dot{F} + \frac{1}{b}F, \tag{3.12}$$

where the dots denote a derivative with respect to time.

The model in Figure 3.4(b) is the Maxwell model which puts the spring and dashpot in series, allowing the system to have a fast initial response followed by constant creep [49]. The differential equation for this system is

$$\frac{1}{k}F = x + \frac{b}{k}\dot{x}. \tag{3.13}$$

The value $\tau_r = b/k$ is the relaxation or creep time constant.

The final model is a combination of the two called the Standard Solid [49]. This model is more characteristic of an actual material. More components can be added to this model as needed to get a better fit to observed behavior. This has a differential equation of

$$(k_1 + k_2)\dot{x} + \frac{k_1 k_2}{b} = \frac{k_1}{b}F + \dot{F}. \tag{3.14}$$

As with dielectric losses, for dynamic operation the loss is usually given as a loss tangent [49],

$$\tan \delta_m = \frac{k''(\omega)}{k'(\omega)}, \tag{3.15}$$

where for the standard solid

$$k'(\omega) = k_2 + k_1 \frac{\omega^2 \tau_r^2}{1 + \omega^2 \tau_r^2} \tag{3.16}$$

and

$$k''(\omega) = k_1 \frac{\omega \tau_r}{1 + \omega^2 \tau_r^2}. \tag{3.17}$$

For the standard solid the relaxation constant is $\tau_r = b/k_1$. These equations show that the loss tangent decreases with increasing frequency.

Semi-crystalline materials, such as polyethylene, do not have considerable viscoelastic losses, but they are still present. Osman et al. [64] found that the loss tangent for high density polyethylene varies from 6 at 0.0016 Hz to $<$0.5 at 160 Hz.

3.2.3 Porous Supports

Porous supports represent a simple solution for creating distributed compliance because the magnitude of the stiffness is easily tailored by adjusting the porosity, as will be shown in the following analysis. Also, there are a number of well established methods for creating porous foams, including the use of blowing agents or phase separation [31]. In polymers, blowing agents can be used to introduce bubbles into a liquid polymer by thermal or chemical decomposition. Then, the liquid is solidified by cross-linking or cooling to lock in the cellular structure. This process is well understood, so that porosity, cell size, and cell structure (opened or closed) can be precisely controlled. However, blowing agents usually produce pores that are a few microns in size. This might be too large for very small gap actuators. To achieve pore sizes on the order of 100 nm, more complicated phase separation methods are necessary [31].

For linear actuators, we are interested in a porous structure that is subjected to uniaxial compression. There is some variation between materials, but a typical stress strain curve for a cellular structure in compression consists of three regions: linear elastic, plateau and densification. For small strains ($<$5%), porous foam shows linear elasticity due to cell wall bending and stretching. For larger strains (between 5% to 80% depending on density), the stress of the foam plateaus because of cell wall buckling. Finally, at high strains ($>$80%), the strain increases sharply because the cells are densified into a solid-like material. The precise size and behavior of each region depends on the properties of the cellular material, and whether or not it is an open cell foam, meaning that the fluid in cells is free to flow between cells, or if it is a closed cell foam, meaning that the fluid is trapped in the cells.

The approximate behavior of different foam types in compression is shown in Figure 3.5. Foams made of brittle materials, such as ceramic foams, experience unrecoverable damage in

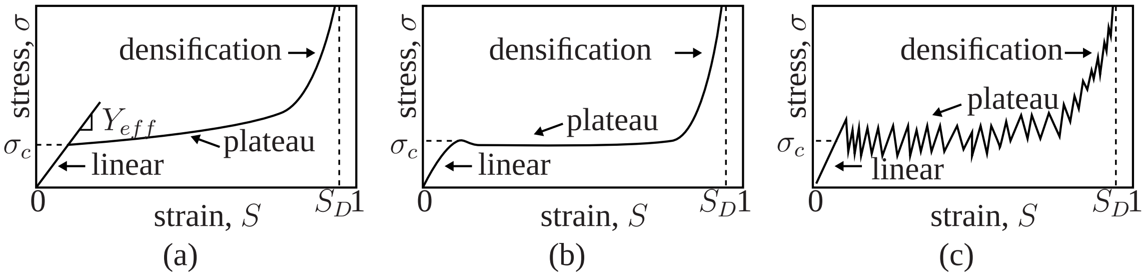

Figure 3.5: Example compressive stress-strain behavior for different cellular foams. (a) Elastomeric foam, where plateau region is from elastic buckling of cell walls. (b) Polymeric foam that shows a plateau region as a result of plastic yielding of cell walls. (c) Brittle foam with jagged plateau region resulting from brittle fracture of cell walls [31].

the plateau region as a result of brittle crushing of cellular structures. Polymer foams can also become damaged during the plateau region if the stress within the cell walls reaches the yield stress of the bulk material. For example, Zhang et al. found that polypropylene foams had 20% unrecoverable strain after being compressively strained to 80% [100]. By contrast, elastomeric foams, such as polyurethane, are fully resilient from compression [100]. This makes elastomeric foams a good candidate for high-strain, actuator support structures. However, viscoelastic losses could be significant with an elastomeric material, and lead to some of the same problems as DEAs.

There are a number of models to describe the behavior of each region. A simple model proposed by Gibson and Ashby [31] will be considered in the following sections.

Linear Elastic

The stiffness of foam in the linear elastic region depends on if the cells are open or closed, and the relative density of the foam ρ_f/ρ_s, where ρ_s is the density of the solid and ρ_f is the density of the foam. For open cell foams with low density ($\rho_f/\rho_s < 0.1$), the stiffness comes from cell bending, but as the density increases, there is more of a contribution from extension and compression of the walls [31]. At low strain rates, the fluid within the cells does not affect the stiffness unless it is highly viscous. For closed cells, the stiffness comes from cell walls bending, compressing and stretching, and from compression of trapped fluid. The relative effective elastic modulus, Y_{eff}, for open cell foams is

$$\frac{Y_{eff}}{Y_s} = \left(\frac{\rho_f}{\rho_s}\right)^2, \tag{3.18}$$

where Y_s is the Young's modulus for the solid material [31]. The modulus for the closed cell foam is

$$\frac{Y_{eff}}{Y_s} = \phi^2 \left(\frac{\rho_f}{\rho_s}\right)^2 + (1-\phi)\frac{\rho_f}{\rho_s} + \frac{p_0(1-2\nu_f)}{Y_s(1-\rho_f/\rho_s)}, \tag{3.19}$$

where ν_f is the Poisson ratio of the foam, p_0 is the pressure in the cells, and $(1-\phi)$ is percent of solid material contained in the cell faces [31]. The Poisson's ratio is completely dependent on the foam cell structure, ranging from -0.1 to 0.5, and it does not show any dependence on relative density. A Poisson ratio of near zero is typical of low density foams in compression [100].

Both of the effective modulus equations are only valid for foam samples that can be treated as a continuous material, meaning the cell size is roughly 20 times smaller than the smallest sample dimension [31]. In actuator use, if the cell size starts to approach the gap size, then more detailed analysis that considers the specific foam structure needs to be performed. For example, the single-level, fibrillar structures discussed in detail in the next section are typical structural elements seen in continuous foams.

Plateau - Yielding

As the foams are compressed, they eventually reach a critical yield stress. The yielding is followed by a plateau region whose length is dependent upon the relative density of the foam. Lower density materials have longer plateau regions, and vice versa. The onset of yielding and the shape of the plateau region depend on whether the foam is elastic or plastic, and whether it is open or closed cell.

For open cell elastic foams with density $\rho_f/\rho_s < 0.3$, the elastic yield stress, σ_{el}, is approximately

$$\sigma_{el} = 0.05 Y_s \left(\frac{\rho_f}{\rho_s}\right)^2 . \tag{3.20}$$

This equation states that the yield stress occurs at 5% strain. This value may change depending on the specific foam, but it is consistent with a number of experiments [31]. For lower density foams, $\rho_f/\rho_s < 0.3$, a correction factor is added to account for higher stiffness [31],

$$\sigma_{el} = 0.03 Y_s \left(\frac{\rho_f}{\rho_s}\right)^2 \left(1 + \left(\frac{\rho_f}{\rho_s}\right)^{1/2}\right)^2 . \tag{3.21}$$

Similarly, for closed cell elastic foams

$$\sigma_{el} = 0.05 Y_s \left(\frac{\rho_f}{\rho_s}\right)^2 + p_0 - p_{atm} \qquad \text{for} \quad \rho_f/\rho_s < 0.3 \tag{3.22}$$

$$\sigma_{el} = 0.03 Y_s \left(\frac{\rho_f}{\rho_s}\right)^2 \left(1 + \left(\frac{\rho_f}{\rho_s}\right)^{1/2}\right)^2 + p_0 - p_{atm} \qquad \text{for} \quad \rho_f/\rho_s > 0.3, \tag{3.23}$$

where p_{atm} is the atmospheric pressure [31].

Plateau - Post Yielding

The post buckling behavior also depends on whether the cells are open or closed. For open cell elastic and plastic foams, the post buckling behavior is essentially flat until densification. As it approaches densification, the stress increases very quickly. This behavior is given by

$$\sigma = \sigma_{el} \qquad \text{when} \quad S \leq S_D\left(1-\frac{1}{D}\right)+S_{el} \tag{3.24}$$

$$\sigma = \frac{\sigma_{el}}{D}\left(\frac{S_D}{S_D-S}\right)^m \qquad \text{when} \quad S > S_D\left(1-\frac{1}{D}\right)+S_{el}, \tag{3.25}$$

where D and m are constants for specific foams, and S_D is the densification limited strain discussed in the next section. As an example, Gibson and Ashby found $m = 1$ and $D = 1$ for a certain type of polyethylene foam [31].

For closed cell elastic foams, the stress increases with further strain because work needs to be exerted in order to compress the trapped fluids. After buckling, the Poisson ratio is essentially zero, so the stress for a closed cell foam increases as

$$\sigma = 0.05Y_s\left(\frac{\rho_f}{\rho_s}\right)^2+\frac{p_0 S}{1-S-\rho_f/\rho_s}, \tag{3.26}$$

where s is the strain. This equation may not apply to closed cell foams whose cells may rupture at yielding. If this is the case, then the foam will behave similarly to an open cell foam [31].

Densification

Gibson and Ashby [31] report the onset of densification for elastic foams as occuring at strains of

$$S_c = 1-\frac{1}{0.3}\frac{\rho_f}{\rho_s}. \tag{3.27}$$

This equation says that an elastic foam with $\rho_f/\rho_s > 0.3$ starts densification immediately, and therefore, does not have a noticeable plateau region.

The compression limit of a foam material is reached when all the cells have collapsed to form a solid material. This state is called densification, and it will occur at different strains depending on the the relative density of the material. Naturally, a highly porous structure will be able to reach larger absolute strains than a less porous material. For both open and closed cell structures, the strain limit is approximately

$$S_D = 1-1.4\left(\frac{\rho_f}{\rho_s}\right). \tag{3.28}$$

For actuator applications using rigid electrodes, the S_D value represents a fundamental strain limit because the material will start acting like a solid, meaning that the Poisson's ratio can no longer be assumed to be near or equal to zero.

Actuator Use

The stress strain behavior for an elastic foam with $m = 1$ and $D = 1$ and different relative densities, ρ_f/ρ_s, is plotted in Figure 3.6 using the equations reported here. From this plot we can estimate the behavior of an actuator that uses the foam as the compliant support structure. For low relative densities, such as $\rho_f/\rho_s = 0.1$, a parallel plate actuator would be able to achieve nearly 70% strain just by overcoming the elastic yield stress. If we assume an elastic material such as a silicone rubber with a Young's modulus near 1 MPa, the elastic yield stress is only, $\sigma_{el} \approx 600$ Pa, which for a relative permittivity of 1 equates to an electric field of ~12 V/μm. This is well below the limit calculated in Section 3.1.1, meaning that the actuator could potentially reach even higher strain. In fact, at a field strength of 110 V/μm, the maximum strain reaches 85% which is very close to the densification limit of 86%. An actuator with this suspension would collapse as the yield stress is reached, but the maximum strain would be limited to the densification strain, S_D.

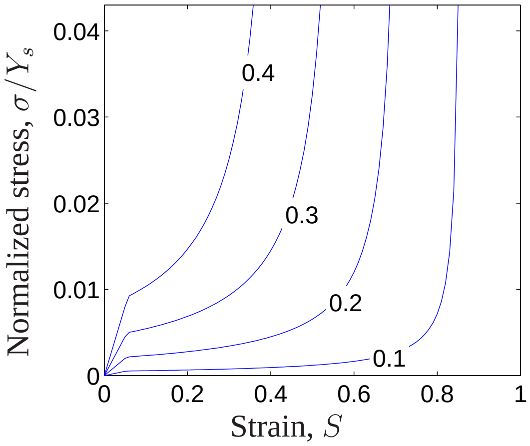

Figure 3.6: Normalized stress as a function of strain for an elastic open cell foam with $m = 1$ and $D = 1$. The values on the lines are the relative densities ρ_f/ρ_s.

3.2.4 Angled Fiber Supports

Open celled porous foams are essentially multilayer arrays of randomly oriented fibers. When the overall dimensions of the foam are much larger than the individual fiber elements (~20x larger), the foam acts like a homogeneous material. However, for electrostatic actuators that require very small gaps, this means that the cell size must be even smaller in order to get uniform behavior. This can present some serious fabrication challenges.

Easier fabrication, and greater control of structural properties, can be obtained by reducing the system to a single layer of highly ordered fibers. Specific properties can be easily prescribed by changing the fiber orientation, dimensions and material. The cross-sectional dimensions can also be changed in order to provide desired directional stiffness properties. For instance, in a comb drive actuator, the supports need to be compliant in the finger length direction, but stiff in the finger width direction to avoid stiction. This could be accomplished by using fibers with a rectangular or oval cross-section.

Angled fibers are a good choice as a support structure because they provide a more gradual stress profile than vertical fibers or foams, which both buckle at small strains. Figure 3.2(a) shows a sketch of an array of angled fibers acting as supports for a parallel plate actuator. Angling also allows the creation of very long compliant fibers that can still fit in the small gaps necessary to achieve high electric fields. Furthermore, there are a number of potential fabrication processes available to create arrays of angled micro- and nanofibers in different materials, including molding and bending of polymers microfibers [1, 44, 50], and etching of silicon nanowires [69].

Problem Definition

Determining the stiffness of an array of angled cantilevers starts by examining a single element. Consider the free body diagram in Figure 3.7(a). We will assume that the fiber length does not change as a result of loading, and because the fiber is thin with respect to the length, we will also neglect shear forces. Therefore, the change in fiber shape upon loading is purely a result of bending. It is also assumed that the number of fibers per unit area are low, so that fibers do not run into each other. Finally, the force at the tip of a fiber is a concentrated force that comes from the electrostatic pressure on the plate divided by the number of fibers, $F = P_e/\rho$, where ρ is the areal fiber density.

To satisfy equilibrium conditions, the force on the fiber tip results in an equal and opposite reaction force at the fiber base. Also, because the fiber is part of an array, and the connecting plates are assumed to be rigid, the fiber ends can not rotate, so they must be able to support a moment. These moments must be equal and opposite to prevent rotation of the plates with respect to each other.

If the fiber has a uniform cross section and a constant inclination along its length, then the inflection point will be at the midpoint of the fiber. At the inflection point the curvature is zero ($d\theta/d\xi = 0$), so the moment is also zero ($M = YId\theta/d\xi = 0$). This allows us to break the fiber in half, so that each half is a fiber with one fixed end and one free end. A single half is shown in Figure 3.7. The shape of the total fiber can be found by combining the solution of the fiber in Figure 3.7(b) with a free end fiber rotated 180° and joined at the tips. Finally, to make the solution of one half easier, we can rotate it such that it is a vertical fiber with an angled load as shown in Figure 3.7(c).

The fiber bending problem is described by the Euler-Bernoulli theory of beam bending [72], which states that the moment at any point along the beam is proportional to the change in curvature

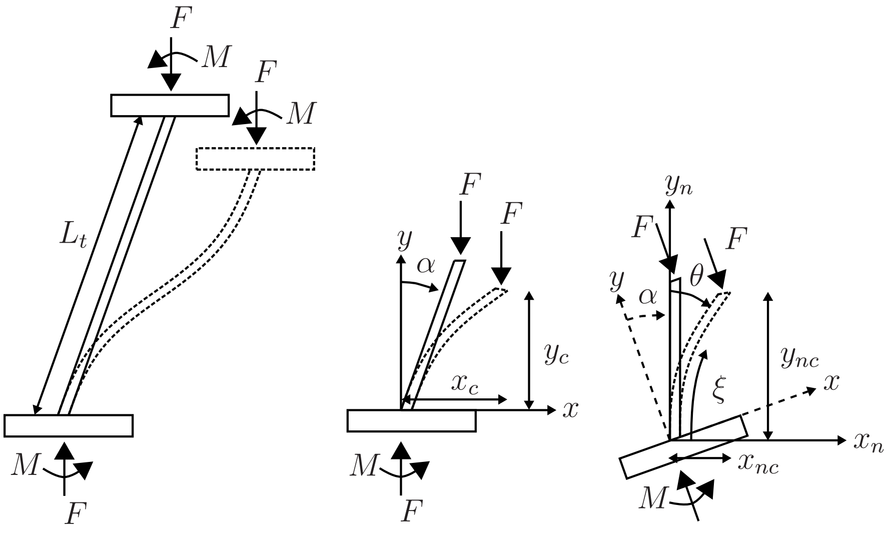

(a) (b) (c)

Figure 3.7: (a) Single angled pillar bending under electrostatic force, F. Because the fiber is part of a uniform array, the tip is allowed to translate but not rotate, so it must support a moment, M. (b) Half of a total fiber. There is no moment on the tip of the fiber because if the fiber is symmetric, the inflection point ($M = YId\theta/d\xi = 0$) should be at the middle of the fiber. The initial angle from vertical is α, and the final position of the endpoints are x_c and y_c. (c) Fiber rotated to allow formulating the problem as a vertical fiber with load angled at α from vertical. The position along the fiber is represented by ξ, and the angle at points along the fiber with respect to vertical is $\theta(\xi)$.

caused by the load. This relationship is summarized as

$$M = YI\frac{d\theta}{d\xi}, \tag{3.29}$$

where Y is the Young's modulus and I is the area moment of inertia, which is $I = \pi R^4/4$ for a circular fiber with radius R. The derivative of the angle θ with respect to position along the fiber, ξ, is equal to the inverse of the radius of curvature, ρ_c, or

$$\frac{d\theta}{d\xi} = \frac{1}{\rho_c}. \tag{3.30}$$

For the particular situation in Figure 3.7(c), the moment at any point along the fiber is described by

$$M = YI\frac{d\theta}{d\xi} = F_{xn}(y_{nc} - y_n) + F_{yn}(x_{nc} - x_n) = F\sin\alpha(y_{nc} - y_n) + F\cos\alpha(x_{nc} - x_n), \tag{3.31}$$

where $x_{nc} = x_n(\xi = L)$, $y_{cn} = y_n(\xi = L)$, and $L = L_t/2$.

We will examine two solutions for equation 3.31. The first is the case where displacements are relatively small, (less than 10% of the length), so that simplifications can be made. This method produces a simple linear model that is useful for quick approximations of fiber array stiffness. We will also examine the complete solution from the theory of elastica. The elastica method describes the complete nonlinear behavior of the fibers. This model will provide insights into performance limits in the high strain regime.

Small Displacements

For small displacements, we use the standard linearization where the square of the slope, is assumed small enough to neglect [27]. Then,

$$\frac{d\theta}{d\xi} = \frac{\frac{d^2x_n}{dy_n^2}}{1 + \left(\frac{dx_n}{dy_n}\right)^2} \approx \frac{d^2x_n}{d^2y_n}. \tag{3.32}$$

We also assume that the length of the moment arm at the tip does not change with deflection since displacements are small. Then, $y_{nc} = L$ and the second term in equation 3.31 drops out. The starting equation is then

$$\frac{d^2x_n}{dy_n^2} = \frac{F}{YI}\sin\alpha(L - y_n). \tag{3.33}$$

We can solve this by direct integration by using the following boundary conditions,

$$x_n(\xi = 0) = y_n(\xi = 0) = 0 \quad \text{and} \quad \left(\frac{dx_n}{dy_n}\right)_{\xi=0} = 0. \tag{3.34}$$

We find that the x_n position of the tip is

$$x_n(\xi = L) = \frac{FL^3}{3YI}\sin\alpha. \tag{3.35}$$

To find the vertical displacement back in the original axes, we notice that

$$\Delta y = x_n(\xi = L)\sin\alpha = \frac{FL^3}{3YI}\sin^2\alpha \tag{3.36}$$

Then, the fiber stiffness in the y direction is

$$k_y = \frac{3YI}{L^3\sin^2\alpha}. \tag{3.37}$$

Finally, the total fiber stiffness in the y direction is

$$k_{ty} = \frac{k_y}{2} = \frac{3YI}{2L^3 \sin^2 \alpha} = \frac{12YI}{L_t^3 \sin^2 \alpha}. \tag{3.38}$$

Similarly, the stiffness in the x-direction due to an applied force in the y-direction can be found following the same steps. The result is

$$k_{txy} = \frac{k_{xy}}{2} = \frac{3YI}{2L^3 \sin \alpha \cos \alpha} = \frac{12YI}{L_t^3 \sin \alpha \cos \alpha}. \tag{3.39}$$

The two stiffnesses, k_y and k_{xy}, have the opposite behavior as α is varied. Increasing α causes k_y to decrease and k_{xy} to increase.

For the small displacement model, the stiffness of a single fiber is constant for all deflections. This makes it easy to determine an effective modulus of an array of angled fibers. The strain of a compressed fiber in the y-direction is

$$S_y = \frac{2\Delta y}{L_t \cos \alpha}. \tag{3.40}$$

The stress is

$$\sigma_y = \rho k_{ty} 2\Delta y, \tag{3.41}$$

where ρ is the fiber density per area. Finally, the effective modulus in the y-direction is

$$Y_{eff,y} = \frac{\sigma_y}{S_y} = \frac{12\rho YI}{L_t^2} \frac{\cos \alpha}{\sin^2 \alpha}. \tag{3.42}$$

Similarly, an effective modulus in the x-direction as a result of stress in the y-direction is

$$Y_{eff,xy} = \frac{\sigma_y}{S_x} = \frac{12\rho YI}{L_t^3 \sin \alpha \cos \alpha} L_x, \tag{3.43}$$

where L_x is the length of the actuator in the x-direction (direction of fiber angling). For large area actuators, $Y_{eff,xy}$ will be large and S_x will be very small.

By knowing the effective modulus of the fiber arrays, the strain as a result of the electrostatic pressure can be determined easily from Hooke's law,

$$S_y = \frac{P_e}{Y_{eff,y}}. \tag{3.44}$$

Large Displacements

For large displacements, the solution to equation 3.31 is found by employing elastica theory. Frisch-Fay provides a concise solution to this problem by employing elliptic integrals [27]. The position of points along the beam are

$$x_n = \sqrt{\frac{YI}{F}}\left\{2p\cos\alpha(\cos m - \cos n) - \sin\alpha[F(p,m) - F(p,n) + 2E(p,n) - 2E(p,m)]\right\} \tag{3.45}$$

$$y_n = \sqrt{\frac{YI}{F}}\left\{2p\sin\alpha(\cos m - \cos n) + \cos\alpha[F(p,m) - F(p,n) + 2E(p,n) - 2E(p,m)]\right\}, \tag{3.46}$$

where $F(\bullet,\bullet)$ and $E(\bullet,\bullet)$ are the incomplete Legendre elliptic integrals of the first and second kind, respectively (see [27] for a complete definition). The value of p is found by solving the following set of equations,

$$m = \sin^{-1}\left(\frac{\sin(\alpha/2)}{p}\right) \tag{3.47}$$

$$L = \sqrt{\frac{YI}{F}}[K(p) - F(p,m)], \tag{3.48}$$

where $K(p) = F(p,\pi/2)$ is the complete elliptic integral of the first kind. Once we know p, we can find the angle at the end of the fiber, $\theta(s = L) = \theta_0$, from

$$\theta_0 = 2\sin^{-1}(p) - \alpha. \tag{3.49}$$

By knowing the angle at the two ends of the beam, we know the entire range of θ values, so we can find the n and s values,

$$n = \sin^{-1}\left(\frac{\sin((\theta+\alpha)/2)}{p}\right) \tag{3.50}$$

$$\xi = \sqrt{\frac{YI}{F}}[F(p,n) - F(p,m)]. \tag{3.51}$$

The above equations describe the complete solution for half of the fiber. To get the entire shape, we simple rotate the solution by 180° and add it to the tip positions, x_{nc} and y_{nc},

$$x_{nt}(\xi) = \left\{\begin{array}{lll} x_n(\xi) & \text{for} & 0 \le \xi < L \\ 2x_{nc} - x_n(L_t - \xi) & \text{for} & L < \xi \le L_t \end{array}\right\} \tag{3.52}$$

$$y_{nt}(\xi) = \left\{\begin{array}{lll} y(\xi) & \text{for} & 0 \le \xi < L \\ 2y_{nc} - y_n(L_t - \xi) & \text{for} & L < \xi \le L_t \end{array}\right\}. \tag{3.53}$$

To get the fiber coordinates in terms of the original axes, the positions are multiplied by the rotation matrix,

$$\begin{bmatrix} x \\ y \end{bmatrix} = \begin{bmatrix} \cos\alpha & \sin\alpha \\ -\sin\alpha & \cos\alpha \end{bmatrix} \begin{bmatrix} x_n \\ y_n \end{bmatrix}. \tag{3.54}$$

Figure 3.8(a) shows an example of the fiber shape when loaded with increasing force. As the fiber deflects, it makes an s-shape because of the fixed ends. Figure 3.8(b) shows the fiber tip position (x_c, y_c) during compression for different initial angles, α. The figure shows that the smaller the α, the higher the possible x displacement. The plots in Figure 3.8 are for fibers with radius $R = 1\ \mu$m, total length of $L_t = 100\ \mu$m, density of $\rho = 4.854 \times 10^9$ m^{-2}, and Elastic modulus of $Y = 200$ MPa. These values are chosen because they are similar to fabricated structures seen in the next chapters, however, the behavior can be generalized to other types of fibers.

The required stresses to achieve high strain seen in Figure 3.8(a) are quite reasonable for electrostatic actuation. For example, consider the curve for the fiber with $\alpha = 45°$. A stress of only 500 Pa is necessary to achieve 70% strain. This amount of stress can be generated electrostatically with a field of only 10 V/μm. Considering the discussion of field strength limits in Section 3.1.1, this is a reasonable value even at the large gap ($\sim 70\ \mu$m) that would be required for a fiber with $L_t = 100\ \mu$m.

The fiber strain in the y-direction is

$$S_y = \frac{L_t \cos\alpha - 2y_c}{L_t \cos\alpha}. \tag{3.55}$$

The mean stress on a fiber array is related to the fiber density, ρ,

$$\sigma_y = \frac{F}{A} = \rho F. \tag{3.56}$$

An effective elastic modulus can be found from Hooke's Law,

$$Y_{eff} = \frac{\sigma_y}{S_y} = \frac{\rho F L_t \cos\alpha}{L_t \cos\alpha - 2y_c}. \tag{3.57}$$

This equation shows that, unlike the small deflection case, the effective modulus is not a constant value. Figure 3.8(c,d) compares the y-direction stress strain curves for the small-displacement, linearized model and the large-displacement, elastica model. The linearized model matches the elastica model well in regions with small y-deflections. These regions are defined by small α values and small strains S_y, or for large α values and large strains S_y. In fact, for $\alpha = 85°$, the curves are almost identical between $S_y = 0$ and 1. Another interesting feature is the buckling-like behavior of fibers with small angles. The curve for $\alpha = 5°$ in Figure 3.8(d) has a threshold stress that needs to be overcome before significant strains can be achieved. However, if more linear behavior is desired, higher α values can be used.

The maximum strain of an array of angled fibers is determined by a few criteria. The first is the elastic limit of the material. If an actuator is to withstand a number of actuation cycles, the

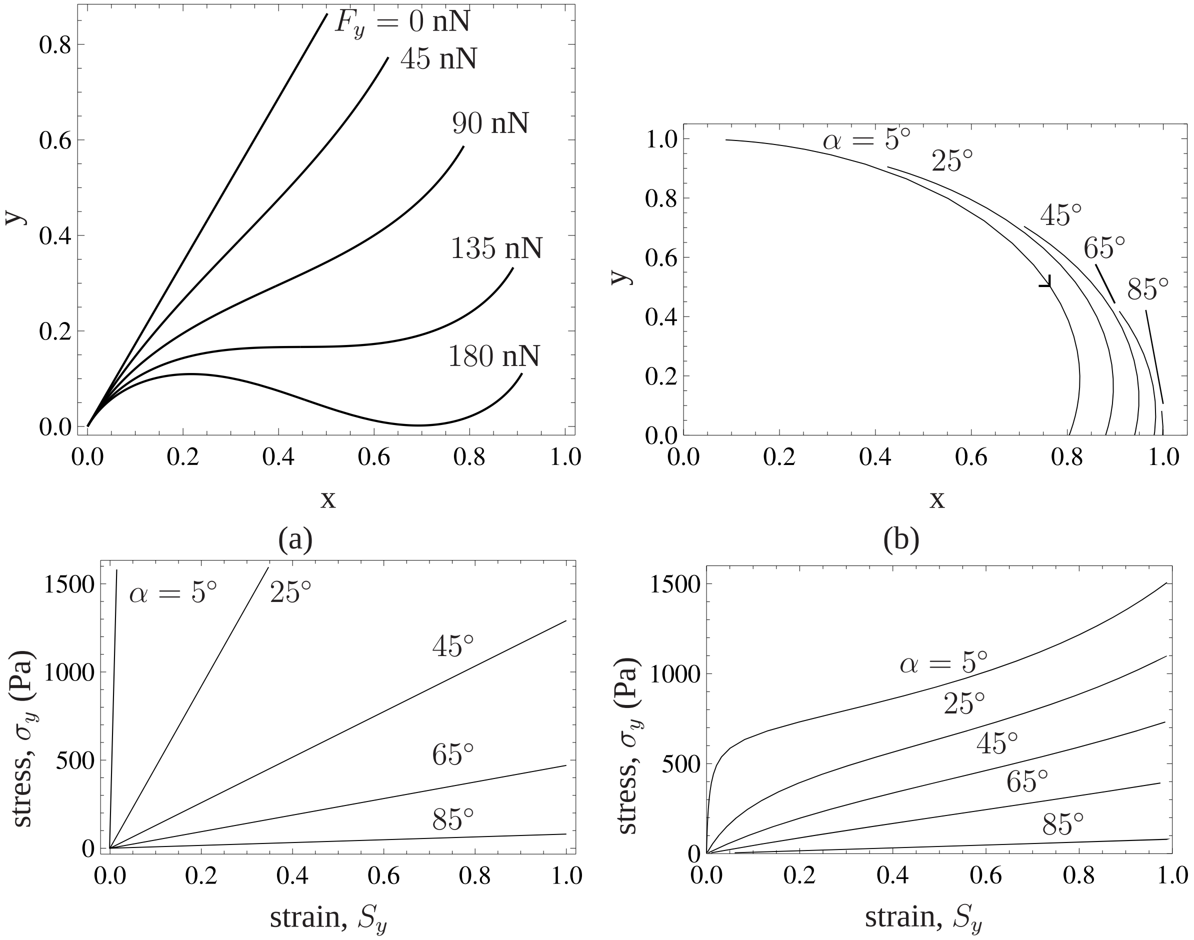

(a) (b)

(c) (d)

Figure 3.8: Plots for low density polyethylene (LDPE) fibers with radius $R = 1$ μm, total length of $L_t = 100$ μm, density of $\rho = 4.854 \times 10^9$ m^{-2}, and Elastic modulus of $Y = 200$ MPa. (a) Shape of a fiber with initial angle of $\alpha = 30°$ compressed by an increasing force, F_y. Position normalized by length. (b) Fiber tip position, normalized by length, as tip is loaded with an increasing force, F_y. (c) Stress-strain curves in the y direction from the linearized, small displacement model. (d) Stress-strain curves in the y direction from the large-displacement, elastica model.

stress should be kept below the plastic yield stress of the material. In the elastica model considered above, the maximum stress from bending occurs at the outer edge of the fiber where the moment is the highest,

$$\sigma_{max} = \frac{M_{max} r}{I}, \tag{3.58}$$

where r is the fiber radius. The maximum moment is located at the base of the fiber, so from equation 3.31,

$$M_{max} = F y_{nc} \sin\alpha + F x_{nc} \cos\alpha \tag{3.59}$$

Figure 3.9(a) shows the maximum bending stress divided by the bulk elastic modulus, σ_{max}/Y, versus strain, S_y, for different angles α. The yield stress for polymers is approximately 5% of the elastic modulus [55], which is represented by the dashed line. The figure shows that for higher initial angles, the maximum stress in the fiber never reaches the yield stress, meaning that these fibers should be able to withstand 100% strain in the y-direction without becoming deformed. The fibers with smaller α values are limited to smaller strains. For example, when $\alpha = 5°$, the maximum strain is ∼50% before yielding occurs. The maximum strain for different fiber arrays will vary depending on the radius-to-length ratio, R/L_t. As R/L_t increases, the maximum strain will become smaller, and as it decreases, the maximum strain will become larger. The elastic strain limit should be considered when designing the actuator so that it is within the stability region determined by the spring stiffness and electrostatic forces. Otherwise, inadvertant plastic deformation could occur.

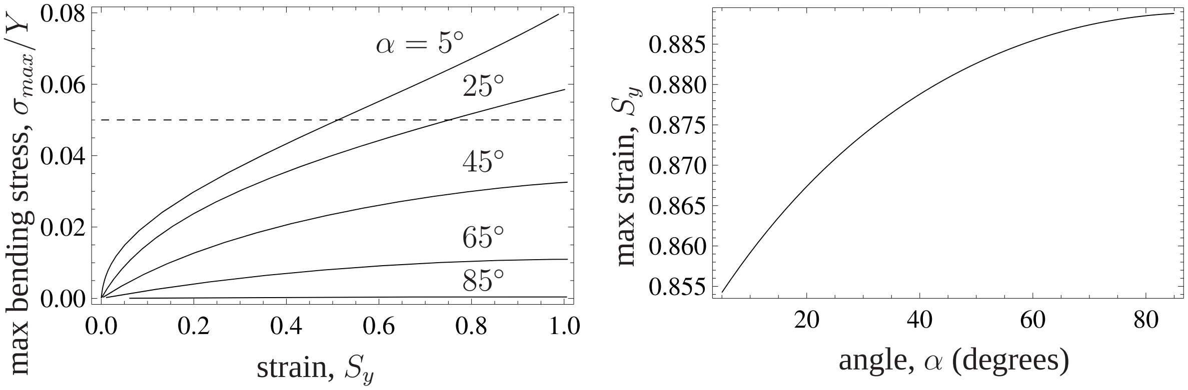

(a) (b)

Figure 3.9: Plots for fibers with radius $R = 1$ μm, total length of $L_t = 100$ μm, density of $\rho = 4.854 \times 10^9$ m^{-2}, and Elastic modulus of $Y = 200$ MPa. (a) Maximum bending stress versus strain in the y direction. (b) Maximum strain in the y direction when outer radius of fiber comes in contact with the electrodes plotted versus initial fiber angle, α.

The other criteria are geometrical considerations. Because the fiber is confined between two plates, none of the points along the fiber can have a negative y position. For simplicity, it will be assumed that the max strain occurs once a point along the fiber reaches $y = 0$, or when

$$y_{max} > 2y_c, \tag{3.60}$$

where y_{max} is the maximum y-position along the fiber. Figure 3.9(b) shows the maximum strain in the y-direction before the outer radius of the fibers come into contact with the plates. The maximum strains are quite high, ranging from 85 to 89% for angles from $\alpha = 5°$ to $85°$. In reality, the array may be able to strain even further, but it is difficult to predict the shape of the fibers once they become confined.

Another geometrical constraint is imposed by adjacent fibers. In dense arrays, this could greatly limit the strain of the fiber array because of jamming and adhesion between contacting fibers. This problem can be avoided in arrays with regular patterns and sufficient spacing by angling the fibers in the direction that provides the most space for bending. Random arrays will encounter more problems from interfiber interactions, but for simplicity, it is assumed that fibers are able to slide past one another.

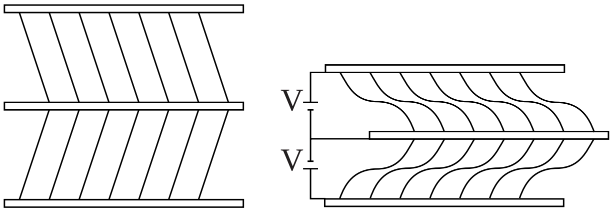

Figure 3.10: Drawing of alternating parallel plate actuator supported by angled fibers. The drawing on the left is the default state with no voltage applied, and the drawing on the right shows the bending of the fiber supports in response to the electrostatic force. The alternating design allows for pure linear compression.

So far, only the deflection in the y-direction has been discussed in detail. However, as Figure 3.8(b) shows, the x-deflection can be quite significant for small α. The deflection in the x-direction can be used as an additional output, or it can be removed by adding structural elements on the ends of the arrays that prevent the plates from moving in the x direction. However, restricting the x motion will result in a stiffening of the array. A better solution to achieve purely linear motion in the y direction is through alternating layers as shown in Figure 3.10. In this configuration, the x displacement is effectively canceled out, but the stiffness of a single layer is unaffected.

3.3 Electrodes

The distributed support structures outlined above are general spring elements that can be used with a number of electrode configurations. Their use has already been highlighted in parallel plate and comb drive actuators. Other electrode configurations are possible, such as the bending configuration shown in Figure 3.11. However, this type of actuators is impractical because is produces small strains, and it relies on the strength of one thin strip of material. Therefore, only the parallel plate and comb-drive configurations are considered here because they can produce large strains, and they can have multiple layers to increase the robustness, force and stroke of the total actuator.

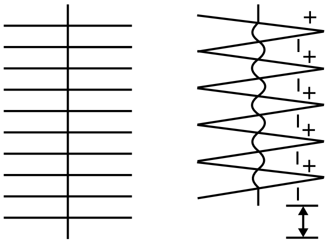

Figure 3.11: Drawing of bending strip actuator. The horizontal bars are alternating electrodes supported by a thin strip. When alternating charge is applied to the electrodes, the bending induced in the support strip causes the actuator to contract, as shown in the drawing on the right.

There are a number of trade offs between the parallel plate and comb drive designs including fabrication, control and performance. The following sections provide an in-depth discussion of the potential trade-offs.

3.3.1 Squeeze-Film Damping

Squeeze-film damping is the result of viscous drag from gas flow between moving plates. When electrodes are pushed together, any trapped gas must be pushed out from between the plates, and when the plates are separated again, a vacuum is created that pulls fluid back into the cavity. Because the proposed designs have open cavities, they will be subject to squeeze-film damping losses if they are not operated in vacuum.

For a plate actuator that has a large plate size relative to the gap size, the damping is related to the length, L, and width, W, of the plates and the position of the moving plate with respect to the fixed plate, y. It is also a function of the viscosity of the fluid, μ, and the velocity of the moving plates, $\dot{y}$. The damping force for small displacements is [20]

$$F_{sf} = \frac{16cW^3L\mu}{y^3}\dot{y}, \tag{3.61}$$

where $\dot{y}$ is the time derivative of the plate position y, and

$$c = 1 - 0.6\frac{W}{L} \text{ for } 0 < \frac{W}{L} < 1. \tag{3.62}$$

The above relationship is only valid for certain assumptions. First, it is assumed that the change in pressure of the fluid does not result in a change in temperature [78]. This assumption can be made because the dimensions of the devices are such that any heat can be rapidly dissipated. Another condition is that the Reynolds number is small,

$$\frac{\omega g_m^2 \rho_f}{\mu} << 1.0, \tag{3.63}$$

where ρ_f is the density of the fluid. The gap size g_m is the mean value of the air film thickness during oscillations. For small displacements, $g_m \approx g_0$. This condition may not hold at high frequencies or large gaps, but for a parallel plate actuator with a gap of $g_0 = 50\ \mu$m running at a frequency of 250 Hz ($\mu \approx 1.8 \times 10^{-5}$ kg/(m·s) for air at 25°C [4]), the Reynolds number is 0.25 [84].

Another condition is the no-slip boundary condition that is met when the Knudsen number is small. The Knudsen number is defined as the ratio of the mean free path of the gas particles to the film thickness, $K_n = \lambda/g_m$ [90]. When the mean free path of the gas reaches one percent of the film thickness, slip-flow conditions can arise, causing the damping effect to decrease [84]. Veijola et al. [90] developed a simple expression to represent this change as an effective viscosity,

$$\mu_{eff} = \frac{\mu}{1 + 9.638 K_n^{1.156}}. \tag{3.64}$$

This equation shows that the effective viscosity of the gas decreases as the Knudsen number increases. The mean free path of air at room temperature and atmospheric pressure is approximately 90 nm [84], so the effect of damping can be reduced by decreasing the gap size below 9 μm.

For large displacements, but small density changes, equation 3.61 can be modified to represent the higher damping forces. This is done by multiplying equation 3.61 by

$$f_D = \left(1 - \frac{\Delta y}{g_m}\right)^{-3/2}, \tag{3.65}$$

where Δy is the plate displacement [84].

Finally, a useful number for squeeze-film damping is the squeeze number,

$$\sigma_d = \frac{12 \mu W^2}{g_m^2 P_m} \omega = \frac{\pi^2 \omega}{\omega_c}, \tag{3.66}$$

where P_m is the mean gas pressure and ω_c is the cutoff frequency. The squeeze number is used to determine the behavior of the damping. At low frequencies relative to the cutoff frequency, the squeeze number is small and the system acts like a purely resistive damping element. For a square plate at low damping numbers the damping coefficient reduces to

$$b = \frac{0.42 A^2 \mu}{g_m^3}, \tag{3.67}$$

where A is the plate area [4]. At high frequencies ($\omega > \omega_c$), the gas film acts like a spring with spring constant

$$k = \frac{P_m A}{g_m}, \tag{3.68}$$

and the damping falls as $1/\sigma_d^{0.4}$ [4]. The cutoff frequency for a square plate 5 mm by 5 mm and air gap size of 50 μm at atmospheric pressure is near 73 kHz, so operation at the 0.1-10 kHz range would experience mostly losses from air damping.

The choice of electrodes will affect the squeeze-film damping. Solid electrodes easily trap air because the only openings are at the edges. For large plates, this can mean significant damping losses. Therefore, it may be necessary to make holes in the electrode to limit this effect [5]. For a parallel plate the holes mean losing active electrode area, but for the comb-drive configuration, most of the electrostatic force comes from the combs, so it may be possible to remove electrode material at the bottoms of the troughs without greatly affecting the force.

3.3.2 Force Control

In terms of ease of control, the comb drive actuator is preferable to parallel plate because, as shown in Section 2.7.2, the gap does not change with displacement. This means that a constant voltage will provide a constant electrostatic force regardless of the position along the stroke.

A parallel plate actuator, on the other hand, has to have a varying voltage with displacement in order to maintain a constant force. Using a constant voltage in the parallel plate configuration can also lead to breakdown and pull-in instabilities because the electric field and force continue to increase as the gap becomes smaller. Alternatively, a constant force can be maintained by using charge control,

$$F = \frac{Q^2}{2\epsilon A}. \tag{3.69}$$

Charge control can still result in pull-in instabilities due to parasitic capacitances, but it can greatly increase the stable range of a parallel plate actuator [77].

3.3.3 Performance - Stress, Strain and Work Density

As shown in Section 3.1.1, designing a device with gap sizes in the field emission regime (< 6 μm) allows for the highest electric fields, and therefore, the highest stress, strain and energy density. The limits of these values for parallel plate and comb drive actuators are compared below.

Stress

The maximum stress is simple to calculate for the parallel plate design. Plugging the maximum electric field, E_{max} into equation 2.17,

$$\sigma_y = \frac{F}{A} = \frac{1}{2}\epsilon E_{max}^2, \tag{3.70}$$

and assuming a relative dielectric constant of 1, the maximum stress is between $\sigma_y = 19$ and 54 N/m^2 for $E_{max} = 65$ to 110 V/μm.

The maximum stress of a comb drive actuator is slightly more difficult to calculate because of the area. The area of a comb drive is equal to

$$A = 2(b + d)h, \tag{3.71}$$

where b is the finger width, d is the gap between fingers, and h is the height of the fingers (see Figure 2.11). This area assumes that the comb drive is a repeating structure consisting of one finger and half the area of the two adjacent fingers. Combining the area with equation 2.20 gives the stress

$$\sigma_x = \frac{F}{A} = \frac{\epsilon V^2}{2d(b + d)} = \frac{\epsilon}{2}\left(\frac{d}{b + d}\right)E_{max}^2. \tag{3.72}$$

This equation shows that the maximum stress depends on the ratio $d/(b + d)$. If the finger width b goes to zero, then the maximum stress is the same as for the parallel plate actuator. However, because the finger will always have some finite width, the maximum stress achievable with the comb drive will always be less than for a parallel plate actuator.

Strain

The ideal maximum strain for either actuator configuration depends on geometrical limits. Assuming very thin plates, the strain of a parallel plate actuator is given by

$$S_y = \frac{\Delta y}{y_0}, \tag{3.73}$$

where y_0 is the original gap size and Δy is the change in gap size. The maximum strain would be close to 100% if the spring elements were completely compressible. However, as was shown in the support section, even low density foams ($\rho_f/\rho_s = 0.1$) have a maximum strain of ~86%.

The comb drive configuration starts off with a maximum ideal strain half that of the parallel plate configuration. If the fingers are allowed to move between the two extremes of tips barely intermeshed, to tips touching the opposite electrode, then the maximum displacement is approximately the length of a finger, L. This means that, in the rest configuration, the total length of the actuator is $2L$. As the fingers are pulled in, the overlap is represented by x, so the strain is

$$S_x = \frac{x}{2L}, \tag{3.74}$$

where, because of geometrical constraints, $x_{max} = L$. In reality, the allowable strain will be limited by the support structures, as is the case for parallel plates, and also by non-idealities of the electric field behavior when the fingers are at the extreme positions.

Work Density

In general, work is defined as the applied force over the displacement, which for a constant force is simply

$$W = Fd. \tag{3.75}$$

The force and displacement are usually dependent upon the size of the actuator, so a good way to normalize this value, for comparison purposes, is to divide by the volume of the actuator. For a parallel plate actuator, with a constant electric field, the work is

$$W = \frac{\epsilon A}{2} E^2 \Delta y. \tag{3.76}$$

Dividing this value by the volume, v, of the actuator gives

$$\frac{W}{v} = \frac{\epsilon A \Delta y}{2 A y_0} E^2 = \frac{1}{2} \epsilon S_y E^2. \tag{3.77}$$

This value is maximized when the initial gap, y_0, equals the final displacement, Δy, or, in other words, when the strain, S_y, is 100%. As already noted, achieving 100% strain will be impossible with support structures between the plates. Assuming an air dielectric, $\epsilon = 8.85 \times 10^{-12}$ F/m, and the maximum electric fields found in Section 3.1.1, $E = 65$ to 110 V/μm, then the maximum work per volume is $W/v = 19 S_y$ to 54S_y kJ/m^3.

The available work per volume for a comb drive actuator is easy to calculate. The force is constant for a given voltage,

$$F = \frac{\epsilon h}{d} V^2. \tag{3.78}$$

As noted above, the displacement, x, has a maximum of the length of a finger, L, so the total volume of the unactuated structure is twice the length times the area

$$v = 2LA = 2(b+d)(2L)h. \tag{3.79}$$

Then, the work per volume is

$$\frac{W}{v} = \frac{\epsilon h x V^2}{2d(b+d)(2L)h} = \frac{\epsilon V^2}{2d(b+d)} S_x. \tag{3.80}$$

If we substitute the electric field into the equation, it becomes

$$\frac{W}{v} = \frac{\epsilon}{2}\left(\frac{d}{b+d}\right) S_x E^2. \tag{3.81}$$

This equation is interesting when compared to the result for a parallel plate actuator. It shows that even as the finger width becomes very small, the highest work per volume ratio expected is still only half the value for an ideal parallel plate. This factor of two lower value is due to the maximum S_x =50% strain achievable with a comb drive compared with 100% for the parallel plate. In practice, because the finger width will be some finite value, the maximum energy density is decreased even further. If the finger width is on the same order as the finger spacing, then the energy density is reduced by another factor of two.

The ideal parallel plate configuration has the highest possible energy density per volume of any electrode configuration. Other configurations, like the comb drive, introduce more unactuated volume (electrodes), while reducing the possible strain of the actuator.

3.4 System Model

Now that we have looked at the components of the actuator, we are ready to consider the entire actuator system shown in Figure 3.12. The actuator has the following governing equation,

$$F_e = \frac{\epsilon A V^2}{2(g_0 - y)^2} = m\ddot{y} + b\dot{y} + ky, \tag{3.82}$$

where m is the mass, k is the spring stiffness, b is the damping and y is the displacement [53]. This system is difficult to analyze with standard techniques because of the non-linearity. It can be numerically integrated with a differential equation solver, but this removes a lot of the insight into the mechanics of the system. Another solution is to linearize around an operating point to estimate small signal behavior. The system equation can be linearized as follows,

$$F_e = \frac{2ky_0}{V_0}\delta V = m\delta\ddot{y} + b\delta\dot{y} + (k + k_e)\delta y, \tag{3.83}$$

where y_0 and V_0 are the operating point values and

$$k_e = -\left(\frac{2\alpha}{1-\alpha}\right) k, \tag{3.84}$$

where $\alpha = y_0/g_0$ [53]. The spring constant k_e represents the effective spring softening that occurs as the plates approach the pull-in instability [78].

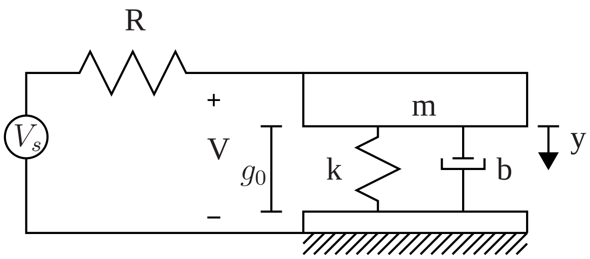

Figure 3.12: Drawing of complete actuator electromechanical system.

A transfer function can be developed from the linearized equations by taking Laplace transforms. The resulting transfer function is,

$$\frac{\delta Y(s)}{\delta V(s)} = \frac{2ky_0}{V_0(s^2m + sb + k + k_e)}. \tag{3.85}$$

However, because of the series resistor, a transfer function from V_s to V is also necessary. This is

$$\frac{\delta V(s)}{\delta V_s(s)} = \frac{1}{1 + sC_0R} = \frac{1}{1 + s\epsilon AR/(g_0 - y_0)}. \tag{3.86}$$

This equation will be used later for comparison with experimental data. With the equations linearized, we can treat the mechanical portion of the system as a mass-spring-damper with a force source. This allows standard techniques, such as Bode plots to analyze the system response at different frequencies.

Some other quantities of interest are the resonant frequency and the quality factor. The spring stiffness and mass will determine the resonant frequency [78],

$$f_0 = \frac{1}{2\pi}\sqrt{\frac{k}{m}}. \tag{3.87}$$

The resonant frequency will shift lower as the operating point, y_0, increases because of the electrical stiffness. The quality factor can also be determined if the damping is known,

$$Q = \frac{2\pi f_0 m}{b}. \tag{3.88}$$

So far, the model only shows the unloaded actuator. When a load is added to the system, the characteristics will change due to the added springs, dampers and masses. In the loaded system, ideally it is desirable to transfer as much power as possible from the source to load. To achieve maximum power transfer, the actuator impedance should match the load impedance [62]. If these values are complex, meaning they contain both loss elements (dampers) and energy storage elements (springs and mass), then the complex source impedance, Z_S, should be equal to the complex conjugate, Z_L^*, of the load impedance. Components will likely need to be added or removed, or the operating frequency will have to be shifted in order to match the two impedances. It may also be possible to take advantage of how the stiffness changes with the operating point for linear and non-linear spring.

3.5 Concluding Remarks

This chapter has demonstrated the potential performance of an actuator with a distributed suspension. The theoretical models are encouraging because they show that as the gap is made very small, it may be possible to achieve very high electric fields, ($>$ 2000 V/μm), and high strains ($>$50%) are also possible. These two numbers translate to an elastic energy density of more than 4.4 J/g. This is comparable to the best dielectric elastomer actuators (3.4 J/g), but without the drawbacks of the elastomeric dielectric. Furthermore, the estimated energy density assumes an average density of 1 g/cm^3, but it may be possible to do better than this if the electrodes have low density and are very thin (possibly CNT sheets). For example, the relative density of the structure would be determined by,

$$\rho_r = P_e \rho_e + (1 - P_e) P_s \rho_s, \tag{3.89}$$

where P_e is the fraction of the volume that is electrode and P_s is the fraction of the remaining volume that is support structure. The ρ values are densities. A very low mass would further increase the specific elastic energy density. Therefore is makes sense to pursue this design further.

In the next sections we will fabricate and test a micrometer-scale prototype. For the prototype, we choose to use angled microfibers between parallel plate electrodes. We choose the angled microfibers because, although both fiber arrays and foam are able to provide the necessary high compliance (> 80% strain) and near zero Poisson's ratio, the porous supports present potential performance issues for future electrostatic actuators with nanometer-scale gaps. In order for a foam between two 100 nm-spaced electrodes to show uniform behavior, the pore size needs to be less than 5 nm. Whereas, uniform behavior can be achieved with angled fibers with a length greater than the gap spacing. The porous foam also requires highly viscoelastic materials in order to achieve high elastic strains, but angled fibers can reach high elastic strains simply by increasing the fiber angle.

The parallel plate electrode configuration is chosen because it has a higher elastic energy density than the comb-drive. Also, the parallel plate structure is much simpler to fabricate than the comb drive structure, which requires numerous challenging micro-fabrication steps.

Chapter 4

Fabrication

Angled micro- and nanofibers are of interest to a wide variety of applications, ranging from synthetic gecko adhesives [1, 50] to field emission sources [18]. Because angled micro- and nanofibers have such a broad range of uses, there is a correspondingly large variety of fabrication techniques that have been developed to produce them. Figure 4.1 gives an overview of some of the techniques, and Table 4.1 provides some characteristic dimensions of fabricated fiber arrays. Table 4.1 only has values of actual fabricated arrays from the references listed. However, most of the techniques could be used to produce a wider range of values than those explicitly noted. For example, the mold drawing technique (shown in Figure 4.1(b)) was only used to produce vertical fibers, but it is easy to imagine adding a lateral force during the pulling step to create a wide range of angled fibers.

For actuators, a desirable fabrication technique is one where it is easy to control the aspect ratio, radius, angle and density of the fiber arrays. Having access to a number of materials also makes a process more versatile because fabrication limitations on size can be accommodated by adjusting material properties. Also, the ability to create uniform fibers over large areas is necessary to facilitate easy fabrication of layered actuators. The techniques highlighted in Figure 4.1 can be broken down into three general categories: direct growth, etching/molding, and thermo-mechanical deformation. Each of the categories has advantages and disadvantages in terms of the actuator fabrication criteria. These differences are discussed in depth below.

All of the fabrication methods are able to control the fiber spacing through various means. For example, an etching/molding technique such as nanosphere lithography (Figure 4.1(e)) controls the spacing by using larger particles than necessary and etching them down before metal deposition. The amount that the particles are etched determines the spacing between SiNWs. In direct growth methods, such as carbon nanotube (CNT) growth (Figure 4.1(h)), the CNT spacing is set by the metal catalyst deposition. The remaining methods control spacing through mask or mold definition.

Some of the techniques are for one specific material, but many can be generalized to a class of materials. For instance, the direct growth technique is tailored only for CNTs, but by using CNT arrays as a master template for molding, a variety of other materials could be used. The

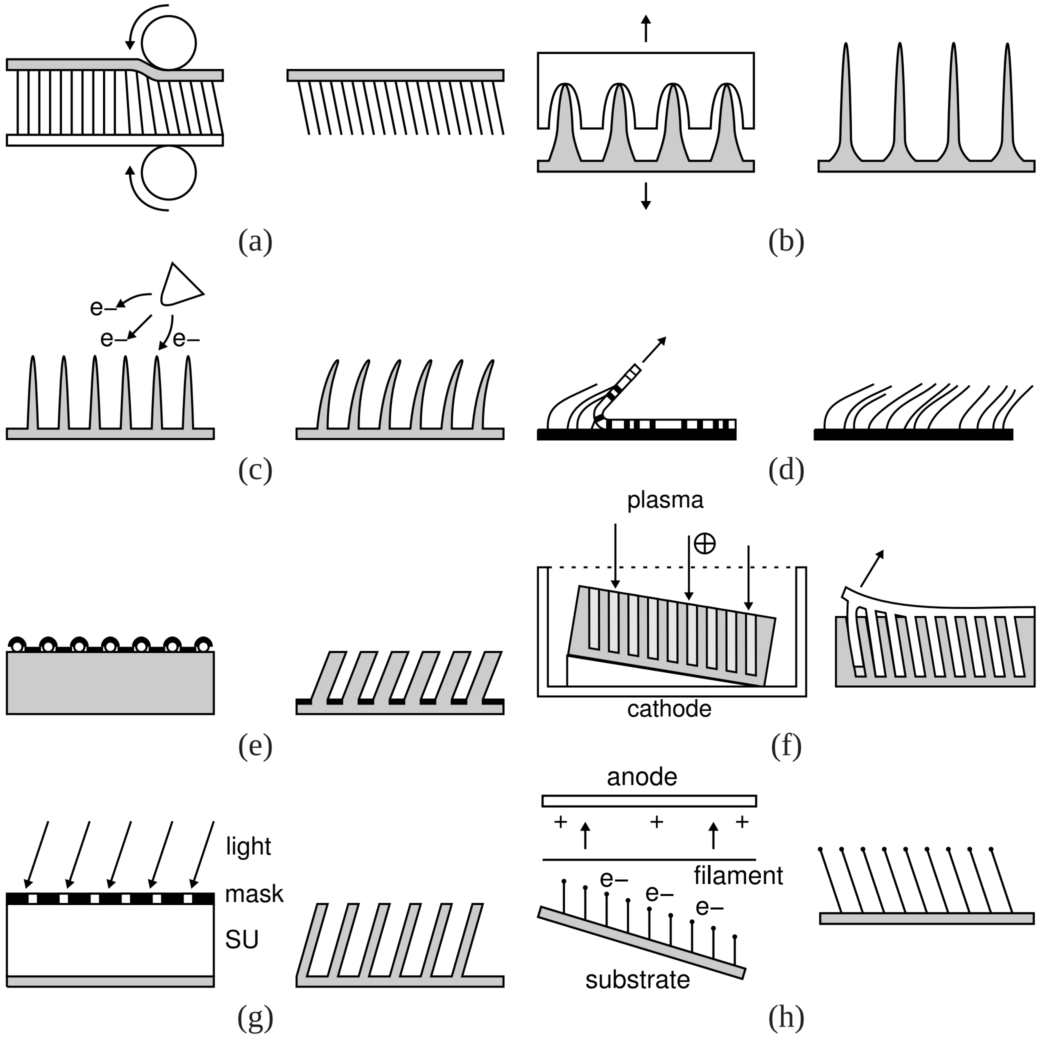

Figure 4.1: (a) Heated rolling of vertical polypropylene (PP) fiber array against glass [50]. (b) Drawing of thermoplastic fiber arrays by separating polyurethane mold at elevated temperature [46]. (c) Bending of polyurethane fibers by exposure to electron beam [48]. (d) Fiber pulling by peeling of a thin mold filled with a thermoplastic. (e) A pattern of holes in a thin silver layer is formed by nanosphere lithography. Then metal-induced etching of a silicon (113) wafer produces angled silicon nanowires [69]. (f) Fabrication of polysilicon mold with angled holes by tilted plasma etching. The dashed line represents the Faraday cage that forces the plasma ions to be perpendicular to the cathode. The mold is used to make polyurethane fiber arrays [44]. (g) SU-8 photoresist is exposed through a mask of holes by angled, collimated UV-light. The developed angled fibers can be used for making molds [1]. (h) Angled carbon nanotubes (CNTs) fabricated on nickel by angled, dc, plasma-assisted, hot-filament chemical vapor deposition (HFCVD) [18].

Fabrication method	Aspect ratio	Radius (μm)	Angle	Material	Reference
Heated rollers (Figure 4.1(a))	30	0.3	0°,45°	PP	[50]
Mold drawing (Figure 4.1(b))	18-25	0.04	0°	PMMA, PS	[46]
E-beam irradiation (Figure 4.1(c))	10-12.5	0.04-0.05	0°-30°	PUA	[48]
Mold peeling (Figure 4.1(d))	$>$45	1-2	5°-70°	HDPE	
Nanosphere lithography (Figure 4.1(e))	12	0.1	0°,30°	Silicon	[69]
Plasma etching (Figure 4.1(f))	6.9	0.2	0°-60°	PUA	[44, 45]
UV lithography (Figure 4.1(g))	$<$20	2-12.5	0°-25°	PU	[1]
HFCVD (Figure 4.1(h))	$>$40	0.05-0.1	0°,45°,90°	CNT	[18]

Table 4.1: Comparison of fabricated micro- and nanofiber arrays. Aspect ratio is defined as length/diameter. Angle is measured from vertical (0°). Abbreviations: HDPE - high-density polyethylene, PMMA - poly(methyl methacrylate), PP - polypropylene, PS - polystyrene, PUA - polyurethane acrylate, PU - polyurethane, CNT - carbon nanotube.

deformation techniques are limited to deformable materials. For stretching, these materials must be able to withstand very large strains without breaking. Most materials become more deformable at elevated temperatures, but for metals and ceramics the required temperatures are very high ($>$400°C). Therefore, thermoplastic polymers are typically used because they can be deformed at relatively low temperatures ($<$200°C), and they can even withstand high elongation at room temperature ($>$500%). Thermoplastics also have a wide range of available elastic moduli from 200 MPa (LDPE) to 3 GPa (PS) [31].

In terms of ease of fabrication, direct growth methods are the simplest techniques because they require the fewest number of steps. The hot filament chemical vapor deposition (HFCVD) technique for producing angled CNTs [18], shown in Figure 4.1(h), is useful because it has good control over fiber dimensions and angles. CNTs can have diameters of a few nanometers for single walled CNT up to hundreds of nanometers for multi-walled CNTs and bundles of CNTs [65], and lengths can be in the tens of microns [18]. For actuators, the diameter would likely be kept small to accommodate the very high elastic modulus of CNTs which is near 0.9 TPa for multiwalled nanotubes [22]. The need to tilt the growth substrate could be a disadvantage by limiting the area of the array that can be fabricated (also a problem for tilted plasma etching in Figure 4.1(f)). This is because high tilts would require large CVD chambers and high electric fields as a result of the large distance between the high and low edges of the substrate. Also, there may be uniformity issues because of large differences in the filament-to-substrate distance across the sample.

Etching/molding techniques such as those shown in Figure 4.1(e-g) can be used to produce fibers with very precise dimensions. However, each process has some limitations on feature size, aspect ratio, and angle. For instance the angled UV lithography process in Figure 4.1(g) is limited by diffraction to angles less than 60°, and it is limited by the wavelength of UV light and the SU-8 photoresist properties to aspect ratios less than 20 and diameters greater than 2 μm [1]. Silicon nanowires (SiNWs) from nanosphere lithography (Figure 4.1(e)) are limited to particular angles because of preferential etching along different crystallographic planes. For a (113) wafer, the resulting SiNWs have an approximate 30° angle [69]. The dimensions of the SiNWs are determined by etch time and the size of the particles used to pattern the metal layer. The wires can range from nanometers to microns, but larger diameters and lengths can result in increased non-uniformity of wire dimensions [69]. The angled plasma etching technique in Figure 4.1(f) can have diameters in the hundred nanometer range [44] and aspect ratios greater than 20 if the Bosch process is used [92]. However, because the silicon holes are used as a mold, the aspect ratio can not be too high. Very high aspect ratios introduce challenges for demolding unless the mold is sacrificed.

Techniques that use thermo-mechanical processing are typically a post-processing step because they rely on prefabricated arrays or molds. The methods shown in Figure 4.1(a-d) could use some of the previously mentioned fabrication techniques to create an array ready for deformation. In fact, the original vertical fibers subjected to e-beam irradiation (Figure 4.1(c)) are made using a plasma-etched silicon mold [48]. In deformation techniques, the angling is done as a last step, so a single mold can be reused to produce a number of fiber arrays with different angles and dimensions. This is advantageous over some of the other techniques where a specific mold or pattern is required for each different fiber array.

The stretching deformation techniques (Figures 4.1(b,d)) are more versatile than the bending deformation methods (Figures 4.1(a,c)) because the fiber dimensions and aspect ratios are only partially dependent upon the original template used to produce the fiber array. As the fibers are stretched, the length is increased while the diameter is decreased, so the aspect ratio is increased. Being able to increase the aspect ratio gives the stretching methods a significant advantage over other techniques because very high aspect ratios ($>$100) are difficult to achieve through etching and molding. Also, as was shown in Chapter 3, higher aspect ratios are necessary to create very compliant structures.

Of the stretching techniques, the mold drawing method in Figure 4.1(b) ideally will have the highest uniformity because the entire array is created at the same time. However, pulling an entire array at once presents some practical challenges for creating large areas. First, keeping the mold perfectly parallel with the fiber array requires extremely precise alignment of the pulling apparatus and the substrate. Second, depending on the fiber density, the forces necessary to pull an entire array at once can become very large as the area increases. For example, consider a material like HDPE which has a yield stress of 20 MPa, and suppose the areal fiber density is 10%. At room temperature, it would take 200 N/cm^2 to yield all the fibers at once. The mold peeling method eliminates both of these problems because the fiber stretching occurs within a small strip. This means that alignment only needs to be maintained over a line instead of a plane, and this is automatically achieved because the portion of the mold being pulled is still bonded to the substrate. Also, because only a strip is being deformed, the peeling force is a function of width rather than area. These reasons make the peeling method more practical than drawing over the whole mold, and they are why this method is chosen to create the compliant fibers for actuators explored in this document.

4.1 Fabrication in Comb Drive Actuator

It is apparent how all of the discussed fabrication methods could be used to create suspensions for actuators with parallel-plate type electrodes. However, it is less obvious how this technology might be used to generate distributed supports within a comb-drive actuator. The following is a hypothetical process that combines a fiber pulling technique with a micromolding method to create perfectly aligned combs with distributed fiber supports.

Comb drive actuators are typically fabricated by standard silicon micromachining techniques [87]. However, this approach is only useful for creating very thin actuators as shown in Figure 2.11. This scale of actuator is perfect for small on-chip resonators, but not for creating large, layered, muscle-like actuators similar to those shown in Figure 3.2. The greatest challenge to fabricating large area comb drive actuators is creating two combs that perfectly intermesh. Creating each side separately and intermeshing them later requires that both sides are absolutely perfect. Any defect in the pattern could prevent the actuator from coming together correctly. If the combs are rigid, this could ruin the whole actuator, and even if they have some flexibility, defects create large dead zones where no actuation occurs.

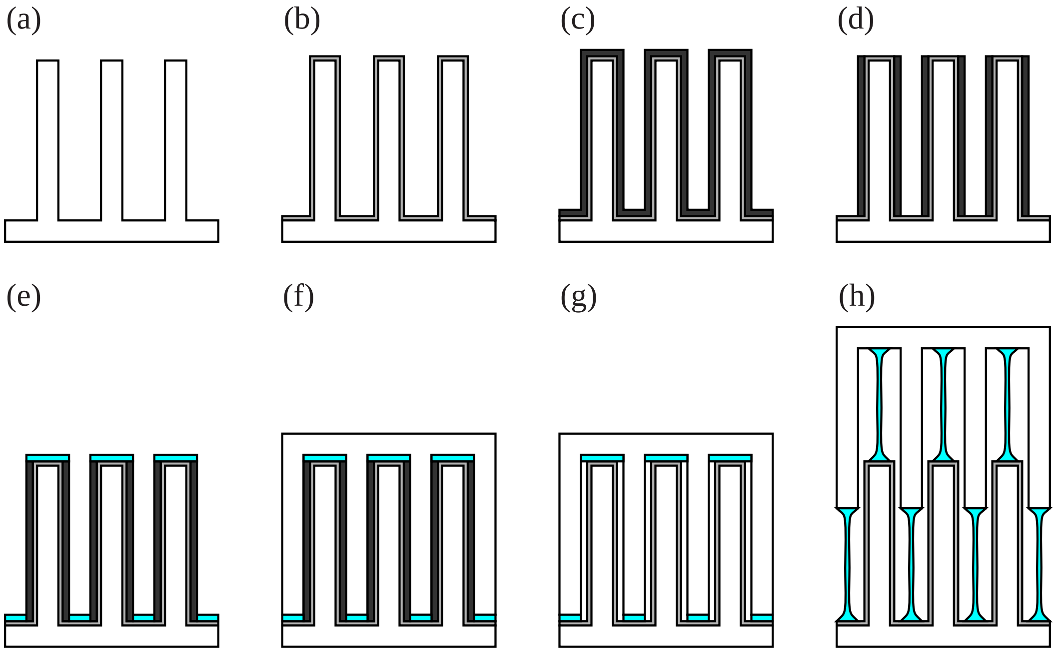

Figure 4.2: Possible fabrication of comb drive actuator shown from the cross section of the fingers. For large area sheets, the fingers could extend far into the page (see Figure 3.2(c)), and the pattern could repeat to either side. (a) Start with one side of the comb already fabricated. (b) Deposit a thin conformal insulation layer. (c) Deposit a conformal sacrificial layer. (d) Perform a directional etch to remove the sacrificial layer at the tips and troughs. (e) Directionally deposit a polymer onto the tips and troughs. A masking step will be required so that polymer dots rather than strips are deposited. (f) Form the top electrode by depositing a conductive material into the bottom comb. (g) Etch out the remaining sacrificial material. (h) Stretch the combs apart to form the support fibers. Shearing the combs into the page while pulling will create angled fibers like in Figure 3.2.

An alternative approach is to create one side of the comb and then use it as a mold to create the second side. This ensures that the two sides intermesh perfectly regardless of defects. A generic process is outlined in Figure 4.2 from the viewpoint of the finger cross section. For large area sheets, the fingers extend into the page (see Figure 3.2(c)), and the pattern repeats to either side. The first step is to form one side of the comb. High aspect ratio fingers could be fabricated by patterning rows of carbon nanotubes or through deep reactive ion etching (DRIE). Then, deposit a thin conformal insulation layer, such as parylene. Next, a conformal sacrificial layer is deposited. A directional etch (such as DRIE) is used to remove the sacrificial material at the tips and troughs of the comb. After the etch, a polymer for supports is directionally deposited into the holes in the sacrificial material. A masking step will be required before or after the polymer support deposition, so that discrete dots are deposited rather than strips that are the length of the trough (into the page). The top comb is then formed by depositing a conductive material into the mold formed by the bottom comb. After the top electrode has been deposited, the remaining sacrificial material is fully etched away. Finally, the combs are pulled apart to set the default position of the actuator by curing the polymer through thermal or chemical means. Shearing the combs with respect to each other into the page will form angled fibers as shown in Figure 3.2. Clearly, this is not a simple process. There are a number of difficult steps, such as the conformal deposition and the precise stretching steps.

The process outlined for fibers could easily be adjusted to create foam supports. If the polymer support layer is deposited with blowing agents, then the comb stack in Figure 4.2(f) could be heated to cause the foam to expand. Then, the sacrificial layer could be etched, and the stretching step would not be necessary because the foam expansion would set the default position. As with the angled fiber approach, this process would be very challenging. A low energy coating on the sacrificial layer would probably be necessary to allow the combs to slide without breaking during foam expansion.

4.2 Methods and materials

High-aspect-ratio, pulled fibers are used as the support structure for the parallel-plate, electrostatic actuators characterized in the Chapter 5. The pulled fiber supports are fabricated by peeling high-density polyethylene (HDPE) from a polycarbonate (PC) mold as outlined in Figure 4.4.

The process starts by UV laser ablation (Coherent MATRIX-355 nm laser) of copper on flex circuit material (Dupont Pyralux AC182500E, 18 μm of copper on 25 μm of polyimide). The laser ablates 10 μm spaced lines across the copper surface using a galvanometer running at a speed of 200 mm/s. The laser pulses at 20 kHz with a pulse duration of $<$20 ns and an average power of $\sim$1.7 W. The roughened copper has a peak-to-peak height of approximately 1 μm. The purpose of the roughness is to allow better bonding of the HDPE to the copper. Otherwise, the HDPE delaminates during fiber pulling.

Next, 9 μm thick HDPE film (Film-Gard high-density painter's plastic) is laminated to the roughened copper using a ChemInstruments Hot Roll Laminator. The laminator provides 2.75 MPa

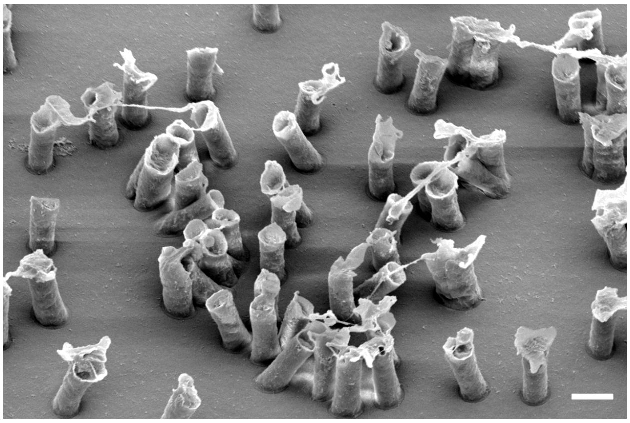

Figure 4.3: SEM of unpulled fibers. The filter was etched off in methylene chloride. The fibers are approximately 5 μm in diameter and 13 μm in length. Scale bar is 10 μm.

of pressure at a speed of 1 mm/s and 175°C. Using the same lamination settings, a 13 μm thick PC filter (Millipore Isopore membrane filter) is filled with HDPE. The filter has 5 μm diameter pores at a density of 4.84×10^9 m^{-2}, measured optically. The filter has a smooth side and a rough side. The smooth side is laminated against the HDPE to lower the necessary peeling force. Also, the pores in the filter have a slightly tapered shape, where the opening on the smooth side is slightly smaller than on the rough side. Therefore, by forcing the HDPE into the side with the smaller opening, the fiber is better anchored in the pore, allowing further stretching during peeling. Figure 4.3 shows an SEM image of the undeformed fibers, where the PC filter was etched away in methylene chloride instead of peeled off.

The 5 μm pore size was chosen for its low fiber density, thin membrane, and the relatively large fiber sizes. The micron-scale fiber size makes fabrication characterization and verification easy, but it still provides useful information for validation of the expected actuator performance outlined in Chapter 3. The low fiber density is necessary to achieve low compliance with the large fiber diameters. Finally, the thin membrane lowers the stiffness of the film, so that it can bend easily when pulled at sharp angles.

The fiber pulling setup is shown in Figure 4.5. The sample is glued (Loctite 406) to a glass slide attached to a resistive heater. The resistive heater is powered by a DC power supply (BK Precision 1760A) controlled by a temperature controller (Omega CN1504-TC). The temperature controller is set to a specific value during peeling, but it fluctuates $\pm 3^\circ$ during operation because of the slow response time of the heating element. A tab made out of a strip of printer paper is glued to the PC membrane and clamped to the linear xy-stages (Zaber Technologies T-LSR150B, 0.5 μm resolution, 150 mm range, 0.00465 mm/s minimum speed, 20 mm/s maximum speed). Before pulling, the tab is positioned to have a prescribed peel angle, θ_{peel}. Then, the stages are run at a constant speed at a set pull angle, θ_{pull}. The stage pull angle is exactly half the peel angle, $\theta_{pull} = \theta_{peel}/2$. The reason that the two angles are not equal is because the position of the peel

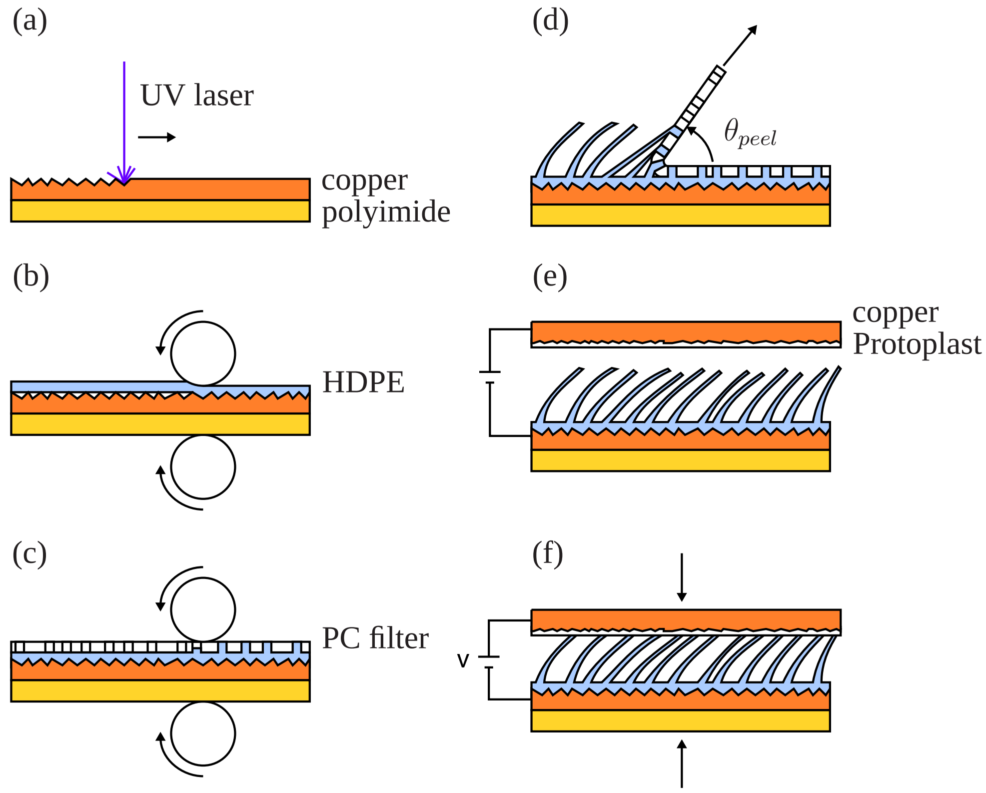

Figure 4.4: Parallel plate actuator fabrication by mold peeling. (a) Roughen copper surface of flex circuit using 355 nm UV laser ablation. (b) Laminate 9 μm thick HDPE film to roughened copper at 175°C, 2.75 MPa and 1 mm/s. (c) Laminate HDPE into 13 μm thick polycarbonate (PC) filter with 5 μm diameter pores at a density of 4.84×10^9 m^{-2}. (d) Peel filter off at a set temperature, speed and angle, θ_{peel}. (e) Attach leads to the top and bottom electrodes. (f) Bond top copper plate, spin-coated with Protoplast, to tips of fibers by applying light pressure at 80°C.

front changes as the tab is pulled (see Appendix A for more details).

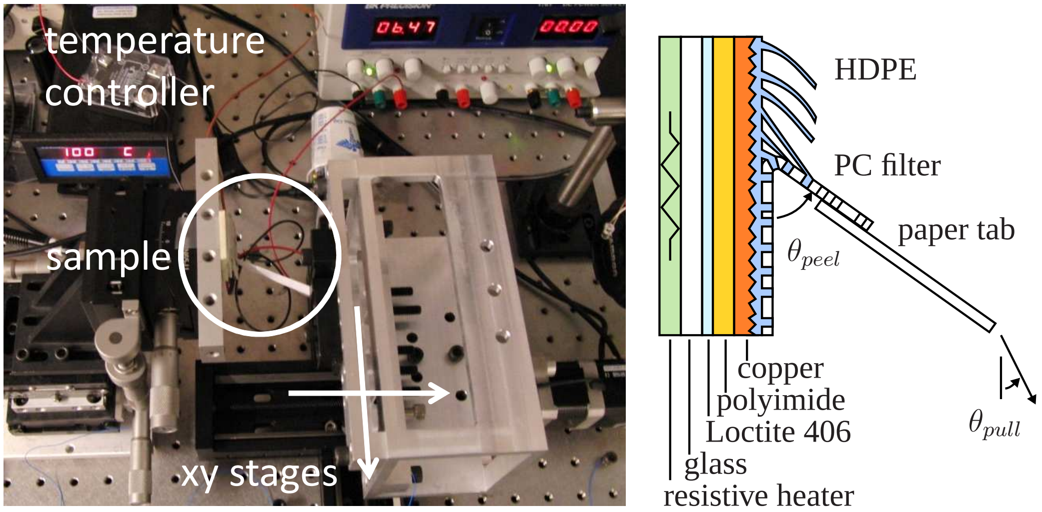

Figure 4.5: Picture of fiber pulling setup with illustration of sample area. The sample is fixed to the table, and the tab is attached to the x y stages.

Before bonding the top electrode to the fibers, thin copper leads (MWS Wire Industries 44 gauge wire) are soldered to the electrodes. This must be done before the plates are attached, so that the soldering iron does not melt the fibers. Next, the actuator is completed by bonding the top electrode to the fibers. To get the top electrode to attach to the tips of the fiber arrays, a low-temperature thermoplastic by the trade name Protoplast (WFR/Aquaplast Corp.) is used. Protoplast is a polycaprolactone-based polymer with a melting temperature of 76°C. The low temperature allows bonding of the top plate to the HDPE fibers without causing any thermal deformation. To make sure that the Protoplast does not flow between the fibers, and to avoid adding a thick dielectric layer between the electrodes, a thin layer of Protoplast (<1 μm) is used. To get the thin layer, the Protoplast is dissolved in methylene chloride (4.35 wt%), and then spin-coated onto the top electrode for 9 seconds at 600 rpm followed by 30 seconds at 3400 rpm. The top electrode is made of rough copper shim (Somers CopperBond extra thin foil (XTF) 5 μm copper film on 35 μm copper carrier). Finally, the sample is placed on a hot plate at 80°C, and the top electrode is pressed onto the fiber tips by the weight of a piece of glass. Care must be taken to avoid any pressure concentrations, or the fibers will get crushed and the top plate will be bonded to the substrate, creating a capacitor instead of an actuator.

4.3 Fabrication results

Angled fiber arrays were created by peeling the filter off at angles between 0° and 90°, at temperatures of 25°C (room temperature) and high temperature (90°C or 100°C), and at a constant speed of 0.1 mm/s. The SEM images in Figure 4.6 are for fibers that were pulled at 100°C. It is difficult to discern much difference between the fibers pulled at room temperature, but there are clear qualitative differences between the fibers pulled at room temperature and those pulled at 100°C. First, the fibers pulled at elevated temperature are longer, as would be expected. Also, the fibers pulled at high temperature appear to be less curved than those pulled at room temperature, with the notable exception of those pulled at $\theta_{peel} = 0°$, whose tips are parallel to the substrate.

It is difficult to measure angles in the SEM images because of the tilted viewing angle, and the unknown rotation of the sample with respect to the pulling direction. Therefore, for a more quantitative description of the fibers, the fiber angles and lengths were measured manually from side view microscope images (Nikon Eclipse L150 microscope with infinity corrected 10x objective, and PAXcam 5 digital camera with 2592x1944 resolution (∼0.24 μm/pixel)). Two example images are shown in Figure 4.7(c,d). Figure 4.7 shows how the fiber angle and length vary as a function of the peeling angle. The angle and length is measured by connecting a line between the base and tip of a fiber. This neglects the curvature of the fiber, so it only provides approximate fiber dimensions.

As the error bars show in Figures 4.7(a,b), there is a significant amount of variation in the measured values. This is partially from the low number of fibers measured because, as shown in Figure 4.7(c,d), only 5-15 fibers are in focus in the side view images. Also, there is a significant amount of variation due to the randomness of the polycarbonate molds. Because the pores in the mold are randomly distributed, there are some pores that are merged together, resulting in larger radius fibers that behave differently during stretching than fibers with the nominal radius. Furthermore, there are likely defects within the polymer film or polycarbonate mold surface that lead to fibers peeling out at different points.

For the length measurements, the error is too large to come up with any specific length trend due to peeling angle. However, there is a difference of approximately 10 μm in the average length over all pulling angles for fibers pulled at room temperature ($L_{avg} = 56\ \mu$m) versus those pulled at 90°C ($L_{avg} = 66\ \mu$m).

For the fiber angles, there is a noticeable trend between the peeling angle, θ_{peel} and the fiber angle α. The linear fits give the following relationships,

$$\alpha = -0.35\theta_{peel} + 41 \qquad \text{for} \quad T = 25°\text{C} \tag{4.1}$$

$$\alpha = -0.67\theta_{peel} + 65 \qquad \text{for} \quad T = 90°\text{C}. \tag{4.2}$$

These fits show that the higher temperature pulling provides a wider range of possible fiber angles (∼5°-65°) than the room temperature pulling (∼10°-41°).

4.4 Modeling

The experimental results do not provide much insight into the mechanics of the fiber peeling process. In order to generalize this process for use with different materials and molds, it is necessary

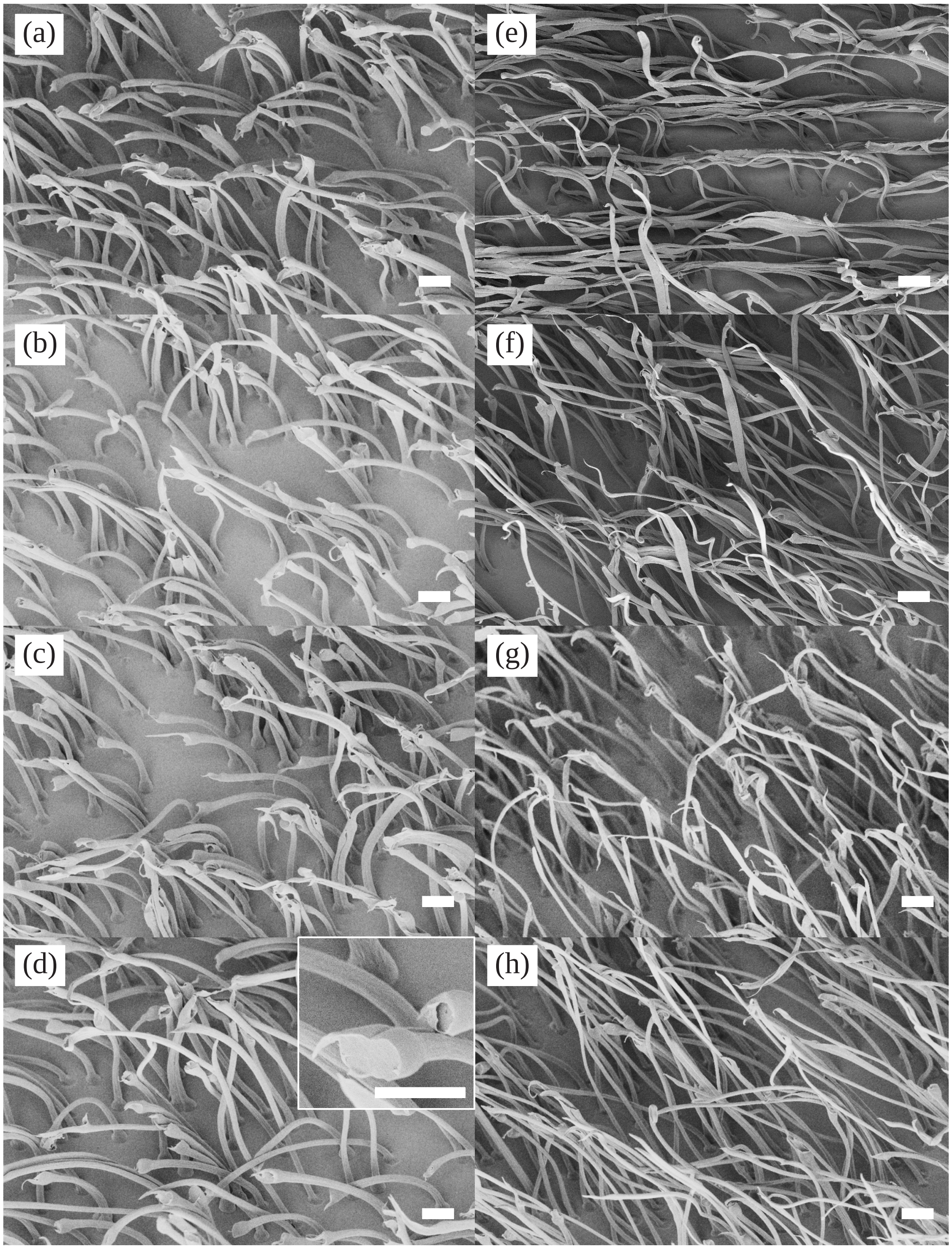

Figure 4.6: SEM images of fibers pulled at 0.1 mm/s and (a-d) 25°C (e-f) 100°C. Peel angles, θ_{peel}, are (a,e) 0° (b,f) 30° (c,g) 60° and (d,h) 90°. Scale bars are 10 μm. SEMs were taken at a 45° tilt. A close up of a necked fiber tip is shown in (d).

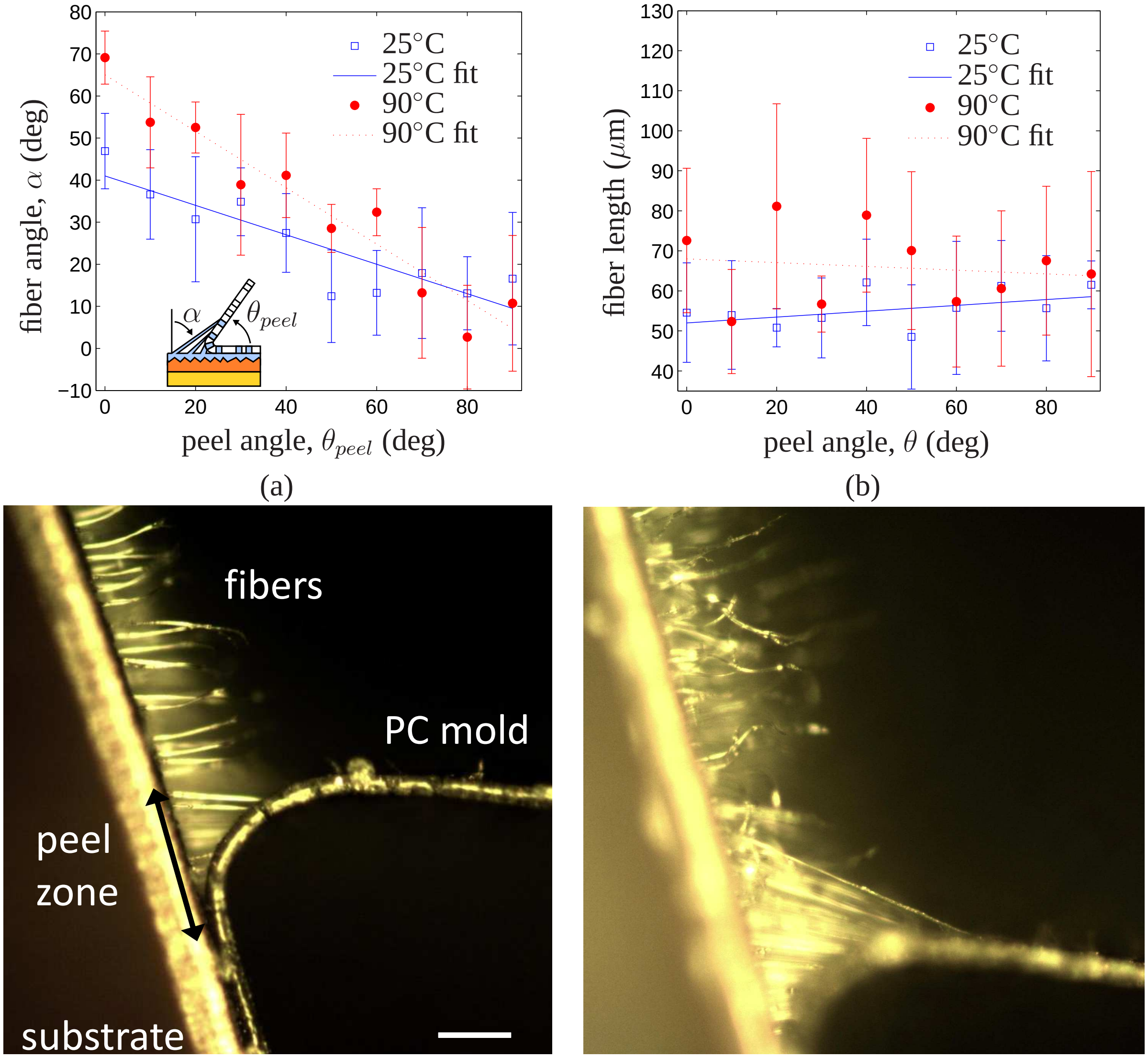

(a) (b)

(c) (d)

Figure 4.7: Results for fiber peeling at various angles, 25°C (room temperature) and 90°C, and at a constant speed of 0.1 mm/s. The plotted values are measured by drawing a line from the fiber base to tip. (a) Fiber angle, α, versus peel angle, θ_{peel}. (b) Fiber length versus peel angle. The lines represent linear fits to the data. (c) Image of fibers being peeled at $\theta_{peel} = 70°$ and 25°C. (d) Image of fibers being peeled at $\theta_{peel} = 70°$ and 90°C. These are representative microscope images used for measuring fiber angles and lengths. The scale bar is approximately 40 μm.

to develop models that can explain the effects of the various process parameters on the fiber array dimension. The following section develops a model to outline the limits of the fiber radius and length.

4.4.1 Radius and length limit

When amorphous or semi-crystalline polymer fibers, such as polyethylene, are pulled from a mold, they either become elongated as a result of necking (cold drawing), or they emerge from the mold undeformed. The criteria for deciding whether or not a fiber will neck or demold is the relationship between the draw force, F_d, and the mold release force, F_m. If $F_d < F_m$, then the fiber will start to neck, but if $F_d > F_m$, the fiber will demold. Figure 4.8 illustrates these two scenarios. The fibers are shown being pulled vertically for simplicity. In actual mold peeling, the fibers would be at an angle, and in some cases, the fiber tip still in the mold may be at a different angle to the rest of the fiber being pulled. In Figure 4.8(a), the fiber emerges from the mold undeformed, and in Figure 4.8(b), the fiber stretches until the release force and the draw force are equal, allowing the fiber to pull out of the mold. By comparing the stresses for a particular mold/material combination, the maximum length can be determined.

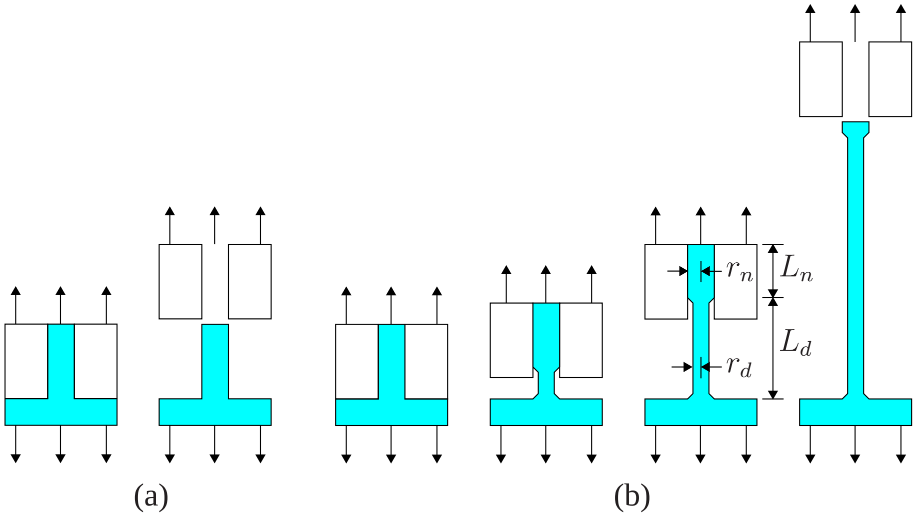

Figure 4.8: Illustration of possible fiber pulling scenarios. (a) Fiber is pulled out of the mold undeformed. (b) Fiber is necked until the drawing force and release force balance, allowing the fiber to pull out of the mold.

The draw force is proportional to the draw stress, σ_d, which is the pressure necessary to initiate necking. Once necking starts, the true stress within the necked region increases until all the polymer chains within that region are aligned. When all the chains are aligned, the radius of the necked region remains constant, as shown in Figure 4.9(a). The ratio of the drawn radius to the original fiber radius is defined as $n = r_d/r_0$. The radius ratio, n, changes for different drawing parameters and materials. For example, a faster drawing speed will result in a smaller n [41]. For set conditions, the minimum fiber radius will be

$$r_{min} = nr_0. \tag{4.3}$$

For a constant drawing speed, the necking propagates into the undeformed section of the fiber for a constant stress, σ_d [41, 54]. Figure 4.9(b) shows the engineering stress profile versus elongation (current length/original length) seen for a fiber being necked. After necking initiates, the stress decreases because the radius of the fiber drops but the stress stays constant (a plot of true stress would not show a drop).

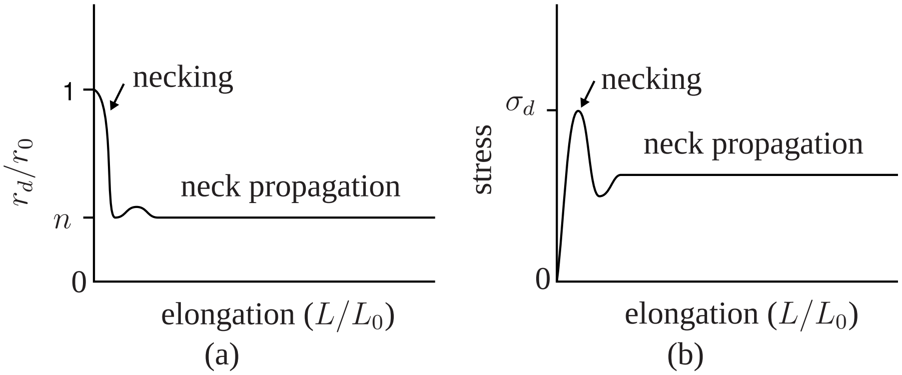

Figure 4.9: Illustration of (a) normalized radius and (b) stress versus elongation.

A side effect of creating fibers by cold drawing is that the drawn fibers have a higher yield stress than unpulled fibers (40 MPa versus 10 MPa) [54]. This is a result of strain hardening from aligning the polymer chains. Because the chains are aligned, a higher stress is required to cause the fibers to yield more. Therefore, a stretched fiber array should be able to achieve higher actuated strains than an unstretched array.

While the draw force is constant throughout pulling, the release force decreases in proportion to the surface area of the portion of the fiber still in contact with the pore. It is assumed that the neck only propagates in the pore direction because it would take more force to pull material out of the substrate. Therefore, as the fiber gets longer, the size of the fiber plug in the mold gets smaller. As a result, the drawing force eventually overcomes the pull out force. This occurs when

$$F_d = \sigma_d \pi r_d^2 = F_m = \tau L_n 2\pi r_0, \tag{4.4}$$

where σ_d is the draw stress, τ is the interfacial shear stress, r_d is the drawn radius and L_n is the pore plug length.

Equation 4.4 can be used to determine the expected length of drawn fibers if a few additional assumptions are made. First, it is assumed that the transition region between the necked and undeformed portion of the fiber is small enough to be ignored. Secondly, the material is assumed to be incompressible, so that the volume of the stretched fiber is the same as that of the unstretched fiber,

$$V = L_0 \pi r_0^2 = L_n \pi r_0^2 + L_d \pi r_d^2. \tag{4.5}$$

The first assumption may not be true for certain drawing conditions. For example, Hutchinson and Neale found that the size of the transition region is dependent on the elongation rate, where slower speeds correspond to longer transition regions [41].

Combining Equations 4.4 and 4.5 and substituting $r_d = nr_0$, gives the following expression for the fiber length,

$$L = \frac{L_0}{n^2} + \frac{1}{2} m r_0 (n^2 - 1), \tag{4.6}$$

where $m = \sigma_d/\tau$ is the mold drawing ratio. As expected, this equation shows that the fibers get longer as the radius ratio, n, and mold drawing ratio, m, get smaller. In the limit, the maximum fiber length occurs when the interfacial shear stress is high enough to keep the fiber in the pore until the entire original fiber length has been stretched to the draw radius,

$$L_{max} = \frac{L_0}{n^2}. \tag{4.7}$$

It is clear that the n value is important for determining the length that a fiber can reach. The n value varies between materials because of factors such as crystallinity, and it varies with test parameters such as temperature. In the literature, it is usually not reported directly, but it can be approximated from the draw ratio, λ, which is the elongation value where drawing switches to yielding. Therefore, using the incompressible criteria,

$$n = \frac{1}{\sqrt{\lambda}}. \tag{4.8}$$

As an example, polyethylene has a draw ratio of $\lambda = 5.3$ (can stretch to over 500%) corresponding to $n = 0.43$, and polycarbonate has $\lambda = 1.7$ so $n = 0.77$ [54].

The maximum fiber length in Equation 4.7 is the limit for the peeling arrangement used in the results section because the top of the pore is open. However, if polymer was molded on both sides of the filter, then there would be a strong enough support to continue stretching the fiber beyond the draw strength. After the entire fiber is drawn, the required stress to continue stretching increases to the yield stress of the material [54]. Further elongation will eventually result in the fiber breaking somewhere along its length. If it could be controlled to break toward the tip, then longer fibers with smaller radii could be fabricated.

The proposed theory can be compared with length and radius measurements taken from SEMs of drawn fibers. Figure 4.6(d,h) shows SEMs of fibers pulled at $\theta_{peel} = 90°$ and 25°C and 100°C. It is evident from these images that the fibers are indeed deforming in the manner proposed above. The plug shape at the tip of the fibers can be easily identified in most of the fibers pulled at room temperature. However, for the high temperature sample, there are less plug-shaped fibers. This is

θ_{peel}	T (°C)	L (μm)	${L_0}^a$ (μm)	${r_0}^b$ (μm)	r_d (μm)	n	m
90°	25	57.9±15.8	13±1	2.46±0.04	1.16±0.18	0.47	0.99
90°	100	88.2±23.0	13±1	2.46±0.04	0.93±0.32	0.38	1.7

Table 4.2: Data taken from SEMs shown in Figure 4.6(d,h). The value for m is calculated from the length and radius data using Equation 4.6. [a]Measured thickness of PC filter using Mitutoyo ID-C112T spring-loaded caliper. [b]Measured from optical image of PC filter. For polyethylene, Masud et al. reported a value of $n = 0.43$ [54].

probably due to a decrease in the draw stress, allowing the fibers to stay in the pores until the entire fiber has necked. Table 4.2 presents data taken from the SEM images in Figure 4.6, and uses this data to back out the mold drawing ratio m. Only one peeling angle is considered because there was not a strong correlation between angle and fiber length from the the data in Figure 4.7(b).

The data in Table 4.2 produced an m value of 0.99 for room temperature and 1.7 for 100°. These values seem reasonable based on numbers reported for polyethylene in the literature. Draw stress ranges from $\sigma_d = 10 - 13$ MPa [29, 54] and the interfacial shear stress for various polyethylene composites ranges from $\tau = 2 - 9$ MPa at room temperature. The value of m would therefore be expected to be in the range of 1-6. As temperature goes up, the draw stress decreases [29], and the shear stress likely decreases as well, so a large change is not seen in the m value. Instead, the increase in n as a result of temperature is responsible for the large change in length between the two samples. The n value probably decreases because the polymer chains become more mobile at higher temperatures.

The draw force can also be approximated by looking at the force necessary to peel the filter at 90°. This can be done by measuring the length of the peel zone, L_p, (see Figure 4.7). The peel zone is measured from where the filter starts to pull away from the sample, until the base of the outermost fiber being stretched. Then, knowing the fiber density, ρ, the sample width, w, and the fiber radius, r_0, the peeling force is

$$F_p = \rho \pi r_0^2 L_p w \sigma_d. \tag{4.9}$$

This equation assumes that all the fibers within the peel zone have reached the steady-state draw stress.

Table 4.3 shows the measured data and the calculated draw stress. The peel force was measured using the setup shown in Figure 4.5 by attaching the peel tab to a six-axis force-torque sensor (ATI Nano-43), and peeling at 0.1 mm/s. The calculated draw stresses (16.2 MPa at 25°C and 4.2 MPa at 90°C) are very close to those reported by Gent and Madan (∼15 MPa at 25°C and ∼5 MPa at 90°C) [29], adding further confidence to our analysis.

θ_{peel}	T (°C)	L_p (μm)	w (mm)	ρ^a (m^{-2})	${r_0}^a$ (μm)	F_p (N)	σ_d (MPa)
90°	25	88.6±14.1	5	4.84×10^9	2.46±0.04	0.66±0.02	16.2
90°	90	139.5±16.5	5	4.84×10^9	2.46±0.04	0.27±0.01	4.2

Table 4.3: Data taken from side view optical images like those shown in Figure 4.7. The value for σ_d is calculated using Equation 4.9. ^{a}Measured from optical image of PC filter.

4.5 Concluding remarks

The mold peeling method for producing high-aspect-ratio, angled microfibers shows promising results. Fibers with lengths between 50-90 μm, radii of 1-2 μm and angles between 0° and 70° were produced, at low peeling forces of 0.54 to 1.32 N/cm. It was shown that there is a clear trend between mold peeling angle and fiber angle. Also, there is a good understanding of how the fiber radius and length can be controlled by adjusting the material, mold and process parameters. However, more tests with other molds and polymers need to be performed to verify the model that was presented. Also, there needs to be more analysis of how the mold stiffness and thickness affect the fiber angle.

Chapter 5

Characterization and Testing

In this Chapter, the samples fabricated in Chapter 4 are characterized and compared against the theoretical models presented in Chapter 3. They are subjected to static and alternating electrical signals to measure their peak performance in these two operating modes. The actuator limitations and deviations from theory are also discussed.

5.1 Test Setup

Tests are performed on the samples fabricated in Chapter 4 using the testing apparatus shown in Figure 5.1. Displacements are measured with an MTI-2100 Fotonic sensor (MTI Instruments, 40 nm y resolution and 30 nm x resolution, 100 μm linear range and sampling rate up to 500 kHz). The sensor measures displacements by monitoring the amount of light transmitted between two fiber optic probes. Therefore, before displacement testing can be performed on the samples, a tab is needed on the top electrode to block the light. A tab is cut from a sheet of 3 mil stainless steel shim stock using the same UV laser mentioned in Chapter 4. The tab is 5 mm wide and 5 mm tall. The x-axis probe is positioned toward the base of the tab, and the y-axis probe is positioned at the top of the tab. The short tab was chosen to have a resonance peak near 2382 Hz ($f = H/(2\pi L^2)\sqrt{Y/\rho}$, with $Y = 193$ GPa, $\rho = 8000$ kg/m^3 and $H = 76.2$ μm [26, 55]). Our interest will be in frequencies below 1000 Hz, so the resonance of the tab should not interfere.

The sample is powered using a TRek PZD700 piezo driver amplifier (voltage gain of 300 V/V up to 1.4 kV). The input to the amplifier is either a 0-5 V DC signal generated by the analog output of a Quanser Computing Q8 real time control board, or an AC signal from a BK Precision 4084 function generator. The BK Precision generator is controlled through RS-232 communication. A 380 kΩ resistor is placed in series with the sample to limit the current if breakdown occurs. The resistor will not limit the actuator response at low frequencies due to charging time because the actuator capacitance is in the picofarad range ($\tau = RC \approx 2$ μs, cut-off frequency is $f_c = 1/(2\pi\tau) \approx 80$ kHz).

The current and voltage supplied by the amplifier are recorded along with the MTI position data using the analog-to-digital inputs of the Quanser Q8 board. The Quanser board is controlled by MATLAB xPC Target running on a standalone computer. The sampling rate of the Quanser Q8 boards is 16.7 kHz, which is 3x the highest driving frequency used.

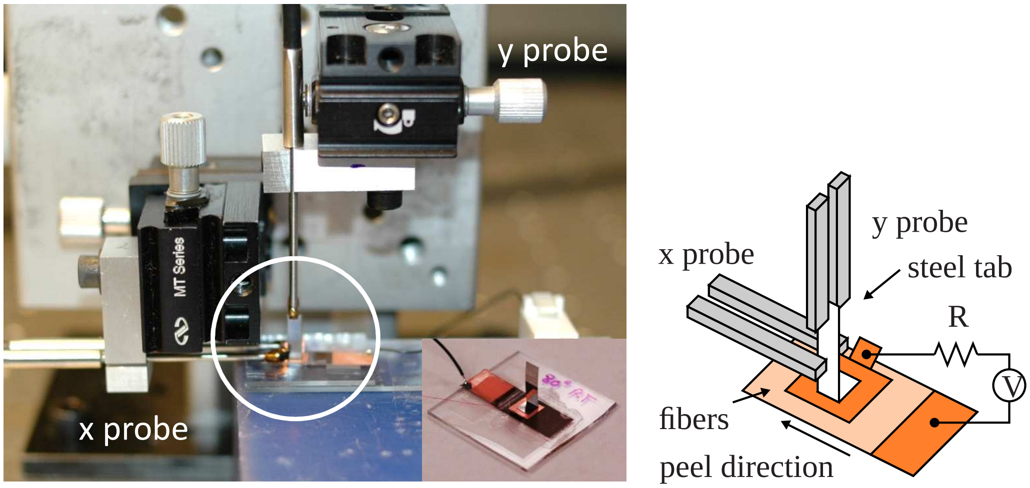

Figure 5.1: Picture of actuator test setup with illustration of sample area. The sample is attached to a high voltage source, and motion in the y and x direction are measured with fiber optic displacement sensors. The x probe is aligned with the peeling direction of the sample.

5.2 Breakdown Limit

The dielectric breakdown strength of the actuators was tested by increasing the applied voltage until the source current jumped. Table 5.1 reports the average values found by testing twenty different actuator samples. Half of the samples were fabricated at 25°C and half at 90°. Each set of ten were made by peeling at angles between 0° and 90° at 10° increments. The electric field was calculated by dividing the applied voltage by the gap. The gap for each sample was measured optically at the center of the top electrode using a Nikon Eclipse L150 microscope. The gap values ranged from 43 to 90 μm, with a mean size of 63 μm. The mean gap sizes depending on fabrication temperature are 58 μm for sample made at 25°C and 68 μm for samples made at 90°C. This is consistent with mean fiber lengths, (56 μm for 25°C and 66 μm for 90°C), measured in Chapter 4.

No definitive correlation was found between breakdown strength and fiber angle or fabrication temperature. Also, there was no apparent correlation with the gap size, contrary to what would be expected from the discussion of the Paschen effect in Chapter 3. However, assuming an air gap of the mean measured gap size, the Paschen effect predicts a surprisingly close value, $E = 9.4$ V/μm, to mean measured electric field at breakdown, $E = 9.7$ V/μm.

	Mean	Standard Dev.	Minimum	Maximum
Gap size (μm)	63	13	43	90
Voltage (V)	598	137	356	904
Electric field (V/μm)	9.7	2.2	5.1	13.9
Electric field Paschen (V/μm)	9.4	-	-	-

Table 5.1: Voltage and electric field at breakdown. Twenty samples were tested. The electric field predicted by the Paschen effect assumes an air gap the size of the mean measured air gap [40].

While the mean value matches well with the Paschen theory, this may only be coincidental considering that the full set of data has no apparent trend. The most likely explanations for a lack of a trend come from examining the actuator structure. Breakdown is most likely to occur where the electrodes are the closest, where the insulation is the thinnest, or where there are defects. Because the gap was only measured at one location (the center of the sample), it is likely that it does not represent the point with the smallest gap. Also, due to fabrication defects, the insulation is not uniform across the whole sample, creating weak points where breakdown can occur at lower than expected fields. Finally, the top electrodes do not have insulation covering their edges, and the sharp corners may provide a point of high field concentration perfect for initiating breakdown. In fact, Figure 5.2 shows a microscope image of an actuator corner where breakdown occurred.

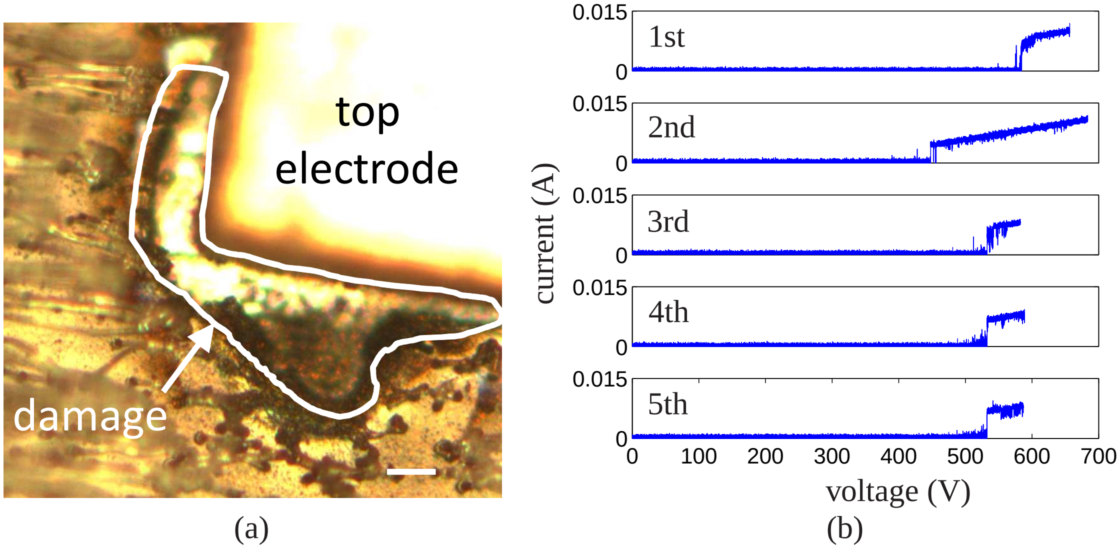

(a) (b)

Figure 5.2: (a) Picture of dielectric breakdown zone near the corner of an electrode. A pit is apparent in the polymer layer. The scale bar is approximately 15 μm. (b) Plot of current versus voltage for sequential DC voltage sweeps. Breakdown occurs when the current jumps up from zero.

When breakdown occurs, the actuator acts like a short circuit, and current is free to flow between the electrodes. Figure 5.2 shows the measured current during sequential DC voltage sweeps for an actuator made by peeling at an angle of 10° and 90°C. The gap between the electrodes is approximately 57 μm. In the first sweep, breakdown does not occur until 582 V, but in the second sweep, breakdown happens at only 446 V. The initial breakdown destroys the insulation between the electrodes, and this creates a weak point that is able to breakdown at a lower voltage. However, the third sweep shows that the breakdown increases from the second sweep to 532 V. The breakdown strength remains close to this value for the following two sweeps. The recovery may be a result of defect removal. If a defect is present (such as a sharp asperity), it is more likely to experience breakdown than the rest of the sample, and, when breakdown occurs, the asperity undergoes major destruction [82]. By destroying the weak point, the breakdown strength is able to recover and stabilize.

Even though the actuator is somewhat tolerant of breakdown, it should be avoided because complete recovery of the original breakdown strength is unlikely. This means that the maximum electric field, and, hence, the maximum displacement and force are lowered. Also, if there is widespread physical damage inflicted on the fiber supports, other performance issues could arise, such as a change in stiffness.

5.3 Capacitance

The capacitances of the actuators were measured using an Excelta TM-200 R-C-L meter (0.1 pF resolution). A control sample was also measured to find the relative dielectric constant of the polyethylene film. The control was fabricated in the same manner as the actuator samples, except the fiber making steps were skipped, and the top plate was bonded directly to the flat polyethylene layer. Illustrations of the control and actuator samples are shown in Figure 5.3.

By measuring the capacitance of the control sample, the relative permittivity of the polymer insulation layer, composed of 9 μm of polyethylene and 1 μm of Protoplast, can be calculated from the following equation

$$\epsilon_r = \frac{gC}{\epsilon_0 A}, \tag{5.1}$$

where C is the measured capacitance, g is the gap thickness, $\epsilon_0 = 8.85 \times 10^{-12}$ F/m is the permittivity of free space, and A is the electrode area. This equation assumes that the capacitance comes from the parallel plate model that ignores the effects of fringing fields. This is a valid assumption because the plate dimensions are much greater than the gap thickness. The area of the top electrode is 5 mm by 5 mm and the gap is only 10 μm. There is some additional area in the form of a tab that sticks off the side of the electrode. However, this is not used in calculations because it is bent up from the sample so that it has a much larger gap than the rest of the electrode (see Figure 5.1). The measured capacitance of the control sample is 48.8 pF. Combining the values results in a relative permittivity of $\epsilon_r = 2.2$. This is close to values found in the literature, where the dielectric constant can vary from 2.26-2.36 depending on polymer density (higher density results in higher

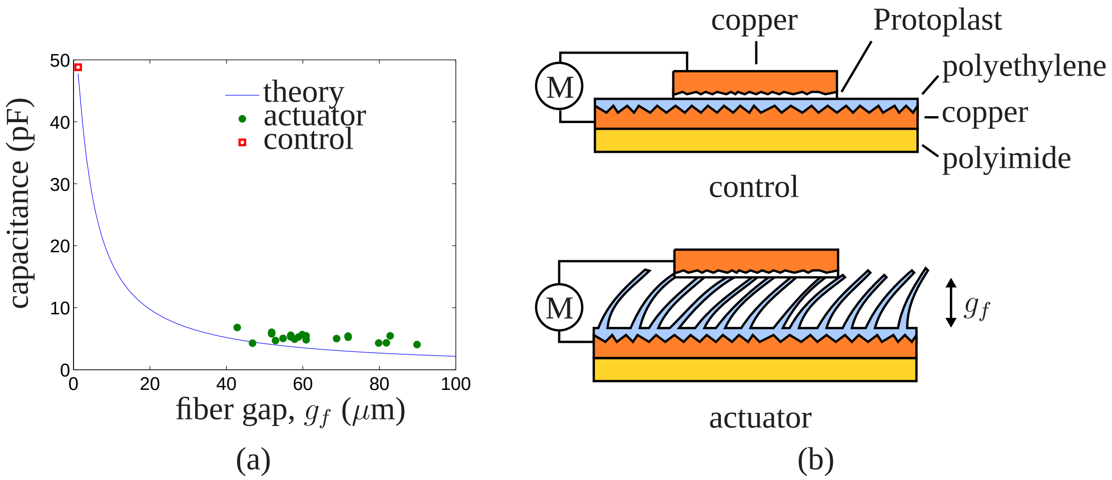

Figure 5.3: (a) Plot of capacitance using equation 5.7. (b) Illustration of samples that were tested. The top electrode has an area of 5x5 mm, and the bottom electrode is 7x25 mm. The polyethylene layer is 9 μm thick and the Protoplast layer is 1 μm thick. The samples are shown connected to a capacitance meter.

permittivity) [21].

By knowing the dielectric constant of the polymer, predictions of actuator capacitance as a function of gap thickness can be made if a proper model is used. There are two states that must be considered when developing an actuator capacitance model. One is the fully compressed state, where the fibers are completely pressed into the bottom electrode. In this state, the dielectric is assumed to be only made up of polymer. This is represented by the control sample. The other state is when the dielectric is composed of a mixture of polyethylene and air. The two states can be linked together by assuming that the total capacitance is a series combination of two representative capacitors, C_i and $C_{fa} = C_f + C_a$. The capacitor that represents the insulating layers, C_i, has a constant value of

$$C_i = \frac{\epsilon_0 \epsilon_r A}{g_i}, \tag{5.2}$$

where g_i is the thickness of the polyethylene insulation.

The capacitance of the fiber/air mixture can be further separated into two capacitors in parallel, C_f and C_a. Each capacitor represents a portion of the total electrode area, A. The amount of area taken by each material is proportional to their respective volume fractions. The total volume is

$$v_t = g_f A, \tag{5.3}$$

where g_f is the fiber gap size. The volume taken up by fibers is a constant value given by

$$v_f = \rho \pi r_0^2 L_0 A, \tag{5.4}$$

where ρ is the areal fiber density, r_0 is the original fiber radius of the mold and L_0 is the length of the holes in the mold. The mold values can be used because it is assumed that the volume of material does not change during stretching. The fiber capacitance is then

$$C_f = \frac{v_f}{v_t}\frac{\epsilon_0\epsilon_r A}{g_f} = \frac{g_m}{g_f}\frac{\epsilon_0\epsilon_r A}{g_f}, \tag{5.5}$$

where $g_m = \rho\pi r_0^2 L_0$ is the thickness of a block of material with area A that would be needed to generate the fiber volume. As a result, g_f must be greater than or equal to g_m. The minimum thickness, g_m, is also subtracted from the total gap thickness of the control sample (10 μm) to estimate the insulation thickness g_i. This is because the fiber volume is taken from the original polyethylene layer.

The volume of the capacitance composed of air decreases as g_f decreases, so the capacitance from air also decreases,

$$C_a = \frac{v_t - v_p}{v_t}\frac{\epsilon_0 A}{g_f} = \left(1 - \frac{g_m}{g_f}\right)\frac{\epsilon_0 A}{g_f}. \tag{5.6}$$

When the actuator is completely compressed, the capacitance from air goes to zero.

The total capacitance is

$$\frac{1}{C} = \frac{1}{C_i} + \frac{1}{C_f + C_a}. \tag{5.7}$$

The line in Figure 5.3 is plotted from this equation using the following values: $\rho = 4.84 \times 10^9$ m^{-2}, $r_0 = 2.5$ μm, $L = 13$ μm, $g_m = 1.24$ μm and the values mentioned above. The theoretical curve predicts capacitance values approximately 1-2 pF below those measured (actuator values ranged from 4-7 pF). The difference is probably due to parasitic capacitances in the leads attached to the actuators.

At large gaps and small displacement, the capacitance can be approximated from the standard equation for a capacitor with an air gap,

$$C = \frac{\epsilon_0 A}{g_f}. \tag{5.8}$$

This is because, when the gap is large, the smaller capacitance of the air dominates the total capacitance.

5.4 DC Testing

5.4.1 Displacement vs. Electric Field

Twenty samples in total were tested multiple times. The set of samples was made by varying the peel angle by 10° between 0° and 90° at temperatures of 25°C and 90°C. The samples were subjected to a voltage that increased at a rate of 100V/s while the x and y displacements were recorded. The electric field was determined by dividing the applied voltage by the measured gap size (measured optically prior to testing).

Figures 5.4(a,b) show plots of this experiment for one of the samples with the highest recorded displacements (sample peeled at 10° and 25°C). Most samples were unable to reach this level of displacement either because of dielectric breakdown or high stiffness. The displacement curves for this sample also show theoretical displacement curves using the equations for small displacements from Chapter 3,

$$Y_{eff,y} = \frac{\sigma_y}{S_y} = \frac{12\rho Y I}{L_t^2}\frac{\cos\alpha}{\sin^2\alpha}, \tag{5.9}$$

where $I = \pi r^4/4$,

$$\Delta y = \frac{1}{2}\frac{\epsilon_0 g_0 E^2}{Y_{eff,y}} \tag{5.10}$$

and

$$\Delta x = \Delta y \frac{\cos\alpha}{\sin\alpha}. \tag{5.11}$$

The small displacement equations are suitable for this analysis because the maximum deflection of 2 μm is much smaller than the fiber length of 56 μm. The fiber values used were taken from Chapter 4, $\rho = 4.84 \times 10^9$ m^{-2}, $r = 1.2$ μm, $L_t = 56$ μm, $Y = 200$ MPa and the α values shown in the plot legends. The initial gap sizes for the theoretical curves, calculated from $g_0 = L_t \cos\alpha$, are 55 and 53 μm for $\alpha = 10.5°$ and 17°, respectively. These values are close to the measured actuator gap size of 58 μm.

The α values were chosen to match with the y displacement. However, the y displacement does not match up perfectly with the linear spring theory. Instead, the data fits within a range of angle values because it acts like a softening spring. This means that there is probably buckling taking place, so the fiber can not be treated simply as a rigid cantilever with a spring at the base. This is also why the simple relation between Δy and Δx listed above does not hold, causing the predicted x displacement values to be off.

A better fit to the data comes from using the elastica model with the same fiber dimensions used for the linear model. The fit from elastica theory also uses a fiber angle value, $\alpha = 27.5°$, closer to the measured value ($\alpha = 35°$ see Chapter 4) than the linear model. This is because, as was shown in Chapter 3, the elastica model predicts that the fibers will soften as they are compressed, and this behavior better matches the observed performance of the actuator. However, the elastica model still overestimates the x deflection. This is likely because the fibers are not perfectly straight, but are instead more of a curved shape (see SEMs in Figure 4.6). A curved fiber would have less x displacement from a load in the y-direction than a straight, angled fiber.

As already mentioned, the data in Figures 5.4(a,b) is atypical for the set of samples. Most samples could survive an electric field of 8 V/μm, but some experienced breakdown at 5 V/μm. Furthermore, the majority of the samples were too stiff to observe significant displacements at these low electric field values. The mean y displacement for all 20 actuators was $\Delta y =$49 nm for a field of $E =$5 V/μm. Assuming a mean gap size of $g_0 =$63 μm, the mean effective modulus

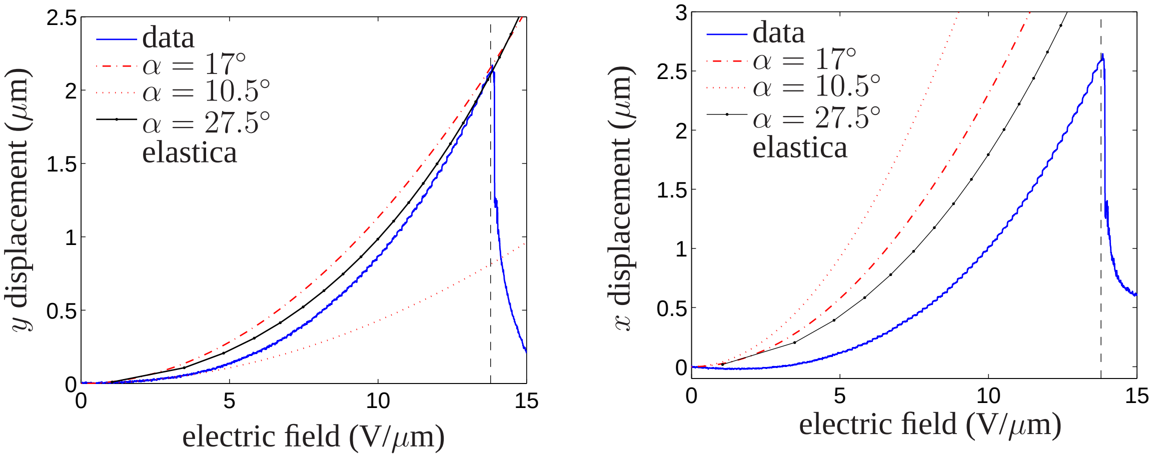

(a) (b)

Figure 5.4: (a) y displacement (compression) and (b) x displacement (transverse) versus applied electric field for a sample peeled at 10° and 25°C. The vertical line marks when breakdown occurs. The dashed lines are displacements predicted from small displacement theory for a specified α, and the solid line with dots is from the elastica model.

of the fiber arrays is $Y_{eff,y}$ =142 kPa. This is 1400 times smaller than the bulk elastic modulus of the material, but still not soft enough to get appreciable displacements at the small electrostatic pressure of only 110 Pa. From the effective modulus, and using the mean fiber dimension values ($\rho = 4.84 \times 10^9$ m^{-2}, $r = 1.05$ μm, $L_t = 61$ μm, $Y = 200$ MPa), the effective fiber angle, α, is approximately 8.3°.

The large discrepancy between predicted and measured displacements is likely tied to a combination of fabrication problems. As shown in the fabrication chapter, there is a significant amount of variation in length, angle and radius between fibers within an array. One possibility is that, as the top plate is attached, the plate initially contacts the longest, most compliant fibers. Then, as the long fibers bend, the shorter, stiffer fibers come into contact with the top plate. When the sample is cooled down, the longer fibers are now effectively the same length as the shorter fibers. However, this is not consistent with the mean gap sizes for the actuators (58 μm for 25°C and 68 μm for 90°C), which are near the mean fiber lengths measured in the fabrication chapter (56 μm for 25°C and 66 μm for 90°C). Another similar possibility is related to the fact that the fibers are curved, rather than straight. The angles measured in the fabrication chapter were from the base to the tip of the fibers and neglected the curvature along the length. However, during attachment of the top plate, it is likely that a portion of the length of highly curved fibers, corresponding to large α values, gets attached to the top plate, effectively lowering the angle α and the fiber length. This concept is illustrated in Figure 5.5.

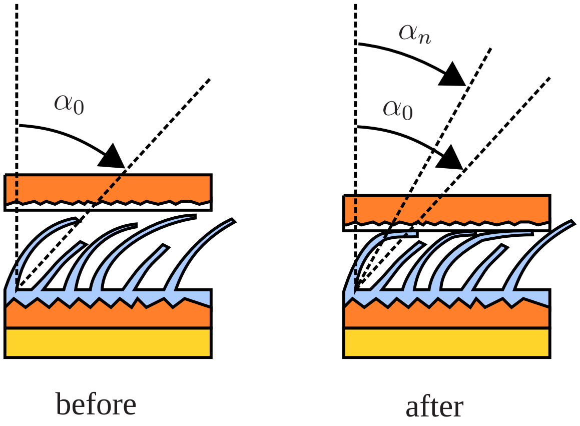

Figure 5.5: Illustration of top plate attachment. The drawing shows how curved fibers become less angled as a result of part of the fiber length bonding to the top plate.

5.4.2 DC Step Response

A repeated DC step response is shown in Figure 5.6 for a sample fabricated by peeling at 40° and 90°C. The voltage of 600 V was cycled at a frequency of 10 Hz. The close up of the step response in Figure 5.6 shows that the initial reponse of the actuator is quite fast ($<$ 2 ms), but the quick response is then followed by a long steady rise.

Careful consideration of the plot reveals that the mean position of the plate drifts until a steady-state value is reached. It is presumed that this is a result of creep in the fiber supports. As discussed in Chapter 3, creep occurs in polymer materials at room temperature, and is especially noticeable at low frequencies.

Figure 5.6(b) shows a close up of the first step with the theoretical viscoelastic curves superimposed on it. The displacement curves are for a step response, where the step input is the electrostatic force, F_e. The electrostatic force is assumed to be constant since the displacement is very small compared to the gap size. The displacement curves are given by the following equations. For the *Kelvin-Voigt* model

$$y(t) = F_e u(t) \left[\frac{1}{k}(1 - e^{-t/\tau_c}) \right], \tag{5.12}$$

where $u(t)$ is the step function and $\tau_c = b/k$. For the *Maxwell* model

$$y(t) = F_e u(t) \left[\frac{1}{k} + \frac{1}{b} t \right]. \tag{5.13}$$

The *Standard Solid* model has a step response of

$$y(t) = F_e u(t) \left[\frac{1}{k_2} - \frac{k_1}{k_2(k_1 + k_2)e^{-t/\tau_c}} \right], \tag{5.14}$$

where

$$\tau_c = \frac{b(k_1 + k_2)}{k_1 k_2}. \tag{5.15}$$

The curves show that there is not much difference between the Maxwell and Standard Solid models, which both give reasonable approximations of the step response.

To verify that the effect is in fact mechanical creep, a simple test is performed where a weight is placed on top of the actuator and the displacement is recorded with no voltage applied. Figure 5.6(d) shows the results of this test. The mass was chosen to provide a force equivalent to the electrostatic force applied in the voltage step response. The large spike in the beginning of the plot is from when the mass was applied. The plot does not show a constant increase in the displacement, but instead seemingly random fluctuations that can be attributed to sensor drift. Furthermore, the slow rise observed in the electrical step response (Figure 5.6(b)) had a slope of $\sim 1\ \mu$m/s, but the mechanical step response (Figure 5.6(b)) shows fluctuations of 100 nm over 50 seconds.

It is possible that the observed creep is an electrostatic phenomenon rather than a mechanical one. When a dielectric with an air interface is placed in a strong electric field, it can start to accumulate surface charges [95]. The slow accumulation of surface charges could lead to a steady rise in voltage, causing the plate to slowly displace. The models used for mechanical creep have electrical analogs to explain charging [89] (capacitors are springs and resistors are dashpots), so, if the effect is actually due to dielectric charging, it is not surprising that the creep models are able to approximate the behavior of the data. Dielectric charging could lead to breakdown or pull-in failures if the actuator is used for extended static holds. The charge accumulation could also lead to operating point drift (as seen in Figure 5.6), affecting precise positioning.

5.5 AC Response

Frequency sweeps were performed on the samples to determine their dynamic response. Because of the high stiffnesses seen in the DC response section, a mass of 302 mg was added to the 9 mg top electrode to bring the resonant frequency down to a low enough value to measure at the 16 kHz sampling rate. The frequency sweeps were done with different electric fields to see how the system changes with operating point. The driving signal is a sinusoid with DC offset, V_{dc}, that sets the operating point, and an AC signal with a peak-to-peak voltage twice the DC voltage, $V_{pp} = 2V_{dc}$. The results are shown in Figure 5.7. From Figure 5.7(a), we can find the resonance frequency, f_0, and the quality factor, Q, and we can use them to estimate the damping, b, and the stiffness, k. To accomplish this we use the following equations,

$$f_0 = \frac{1}{2\pi}\sqrt{\frac{k}{m}} \tag{5.16}$$

and

$$Q = \frac{2\pi f_0 m}{b}. \tag{5.17}$$

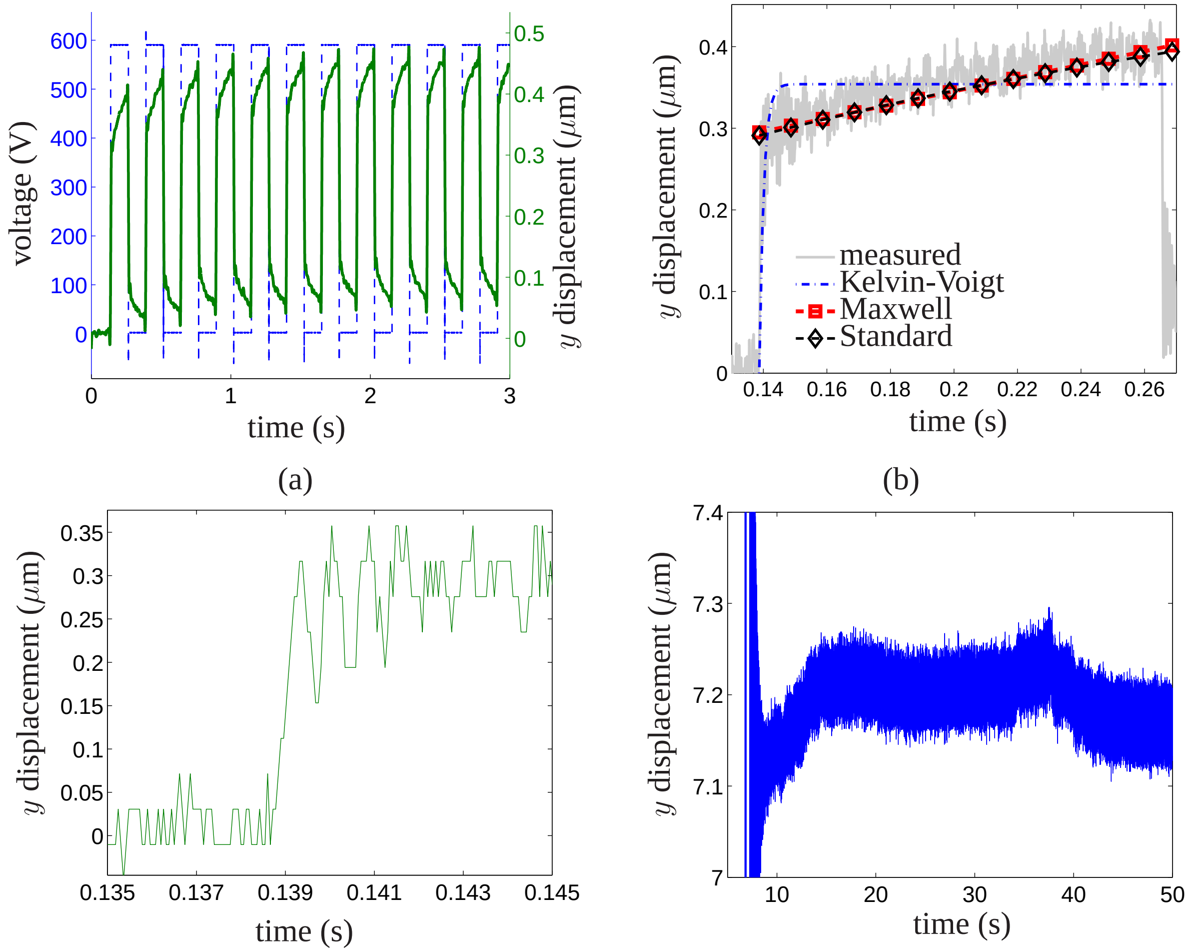

(a) (b)

(c) (d)

Figure 5.6: (a) Repeated DC step response for a sample made by peeling at 40° and 90°C. (b) Close up of unfiltered data for the first step, and theoretical step responses drawn over the data. (c) Close up of first few milliseconds of the step response. (d) Plot of displacement over time for a constant force (481 mg weight).

V_{dc} (V)	V_{pp} (V)	f_0 (hz)	Q	b (Ns/m)	k (N/m)
300	600	845	13.0	0.127	8766
250	500	870	11.4	0.149	9293
200	400	894	7.8	0.224	9812
150	300	960	4.5	0.417	11315

Table 5.2: The Q and f_0 values were measured from Figure 5.7. The damping and stiffness were calculated using the Q and f_0 values. Mass is $m = 311$ mg.

The Q is found from the plot by taking the resonant frequency, f_0, and dividing by the -3db bandwidth below the peak.

The values are shown in Table 5.2. The calculated stiffness values are on the same order as those calculated in the DC response section ($k = E_{eff}A/g_0$, gives $\sim$20-30 kPa). As predicted by the theory, the resonant frequency shifts to lower values because of spring softening at higher voltages. The higher voltages also have the effect of lowering the damping losses. The modest Q value makes it advantageous to run the actuator at resonance. As can be seen in Figures 5.7(c) and (d), the actuator gets approximately twice the displacement by running at resonance, and it has lower losses.

The measured losses are likely a combination of viscoelastic and squeeze-film damping. The contribution from squeeze-film damping can be estimated by using the equation presented in Chapter 3 for low frequency oscillations,

$$b = \frac{0.42A^2\mu}{g_m^3}. \tag{5.18}$$

Using a mean gap size of g_m =59.5 μm, an area of A =25$\times$10^{-6} m^2 and an air viscosity of μ =1.8$\times$10^{-5} kg/(m·s), results in a squeeze-film damping of b =0.022 N·s/m. This number may be an underestimate because the squeeze-film equation assumes parallel plates with no structures in between, so it does not account for any added losses generated due to the air having to move between the fibers.

The Bode plot in Figure 5.7(b) was generated by substituting the values from Table 5.2 (b=0.13 Ns/m, k=8800 N/m, $m = 311$ mg, V_0=300 V, $g_0 = 60$ μm, $R = 380$ kΩ and $y_0 = 0.5$ μm) into the linearized transfer function,

$$\frac{\delta Y(s)}{\delta V_s(s)} = \frac{2ky_0}{V_0(s^2m + sb + k + k_e)}\frac{1}{1 + s\epsilon AR/(g_0 - y_0)}. \tag{5.19}$$

The Bode plot predicts a resonant frequency of 842 Hz and a quality factor of 12.6. The magnitude of the transfer function closely matches the measured magnitude shown in Figure 5.7(a). These numbers are very close to the measured values, so the model may be useful in predicting future operating values.

Predicting the power density of the actuator requires a few assumptions since we have only run the actuator with a purely inertial load. If we assume that the load is matched to the impedance

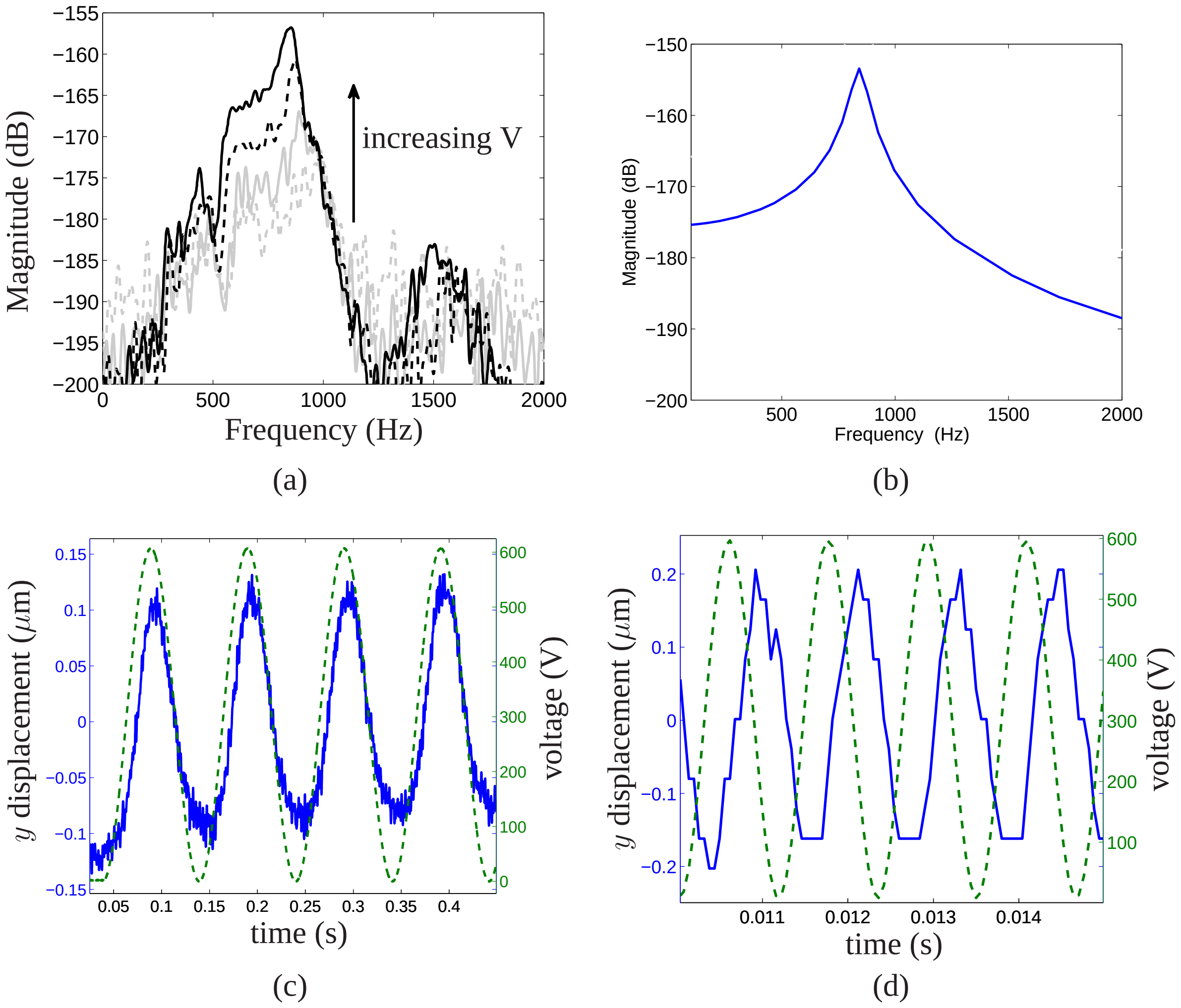

Figure 5.7: Dynamic tests for a sample made 60° and 90°C. (a) The frequency response for increasing voltage. The lowest voltage is 150 V_{dc} + 300 V_{pp} and it increases by 50 V_{dc} and 100 V_{pp} up to 300 V_{dc} + 600 V_{pp}. The magnitude is the y-displacement divided by the applied voltage in decibels. (b) Bode plot for response of linearized model, using b=0.13 Ns/m, k=8800 N/m, $m = 311$ mg, V_0=300 V, $g_0 = 60$ μm, $R = 380$ kΩ and $y_0 = 0.5$ μm. (c,d) Plots of sample running at 300 V_{dc} + 600 V_{pp} at 10 Hz and near resonance at 870 Hz.

of the actuator, and that the load does not affect any of the actuator values, we can estimate the maximum power delivered to the load. The maximum power delivered for a matched load is calculated from the following equation:

$$P_{max} = \frac{1}{8}\frac{F_{max}^2}{b}. \tag{5.20}$$

The F_{max} value was not measured during testing, but it can be estimated from the maximum voltage, V_{max},

$$F_{max} = \frac{1}{2}\epsilon_0 A \left(\frac{V_{max}}{g_0 - y_0}\right)^2. \tag{5.21}$$

Using the values of A =25 mm^2, V_{max} =600 V, g_0 =60 μm and y_0=0.5 μm, the maximum force is F_{max} =11 mN. Using the estimated damping of b =0.127 N·s/m, the maximum power is, P_{max}=120 μW. Finally, dividing by the total mass of the unloaded actuator, 9.4 mg, the estimated power density is 12.8 W/kg. This number is mostly speculative because our assumption that the load does not change the behavior of the system is almost certainly not true. The power density is only one to two orders of magnitude lower than other micro-actuators. For instance, piezoelectric actuators have a power density near 400 W/kg [26].

Chapter 6

Conclusion

This work presented an innovative suspension design for enabling new, energy dense, robust, compact electrostatic actuators. A review of the current actuator field found that, even though there are a large number of established or emergent technologies, they are all lacking in certain key aspects such as reliability, maximum stress and strain, or response speed. Therefore, designs for a new suspension for electrostatic actuators were presented. The critical innovation of the proposed angled fiber and porous foam suspensions was the near zero Poisson ratio that allows the suspension to be placed between standard parallel plate and comb drive electrodes to create an actuator with reliable solid electrodes, potential high stress ($>$1.1 MPa) and elastic strain ($>$50%), a fast response and low mass and volume. A simple fabrication method involving molding and peeling of microfibers showed that it is possible to create high aspect ratio (66:1.8) angled thermoplastic fibers with a fixed radius controlled by the draw ratio of the material. Finally, parallel plate actuators using the angled microfiber arrays were tested and shown to have a fast response time of $<$2 ms, maximum strain of 3.4% at a stress of 0.85 kPa (limited by dielectric breakdown at 13.9 V/μm), and power density of 12.8 W/kg. While not exceptional, the results are promising considering the limitations of the micrometer size scale. Future versions will take advantage of nanometer-scale fibers and gaps in order to approach the theoretical limits of this design.

6.1 Future Work

Clearly the microscale design does not meet the high expectations of the design chapter, but this is not surprising because the design chapter outlined the limits for ideal nanometer-scale devices. Major improvements in actuator performance are possible by addressing the fabrication issues discovered here, and by creating new techniques to generate structures at the nanometer scale.

The fiber peeling method used open molds with random pore spacing that resulted in highly non-uniform fiber arrays. One possible improvement is to seal off one side of the molds to prevent overfilling, and therefore, prevent the large difference in fiber length that can lead to unpredictable stiffness. Another improvement is to use a mold with a regular pore spacing. This would limit the number of entangled fibers that can create stiff fiber bundles and cause problems due to fiber-fiber collisions. Both of these improvements could be accomplished by using molds made from a regular silicon template as shown in Figure 6.1(a).

The proposed improvements to the fiber peeling technique do not address the critical issue of fiber shape. One of the problems with the current fiber arrays is that the fibers are actually curved instead of straight, angled beams. The fiber peeling method was used because it is able to create large area fiber arrays with low forces and simple alignment. However, the alternative fiber pulling technique mentioned in Chapter 4 might provide more ideal angled fibers. Figure 6.1(b) shows how angled fibers could be formed with the electrodes already attached. Having the fibers fixed at both ends during stretching would prevent them from drooping into a curved shape, and it would keep them from clumping together.

Improvements to the current process may not solve the underlying problem of low maximum electric fields. The large gap size of the microscale actuator limits the maximum electric field strength. As was shown in the design chapter, electric fields $\sim$200 times those achieved here are possible with gap sizes <1 μm and atomically flat electrodes. It may be possible to use a method such as in Figure 6.1(b) to create actuators at the nanoscale. However, stretched polymer nanofibers may be too compliant for the high electrostatic stresses possible at very small gaps. Therefore, other materials need to be considered, such as carbon nanotubes (CNTs). In the fabrication chapter, a method was introduced for creating angled CNTs using plasma-assisted chemical vapor deposition. Building on this process, alternating layers of electrodes and CNT suspensions could be deposited to easily build up a multilayer actuator as shown in Figure 6.1(c).

In all the future processes considered, a challenge will be designing the the electrodes so that they are as thin as possible yet still strong enough to support the loads at the outputs. The fibers will help reinforce the electrodes and distribute the loads to limit pressure concentrations, but electrode cracking in between fibers could be an issue.

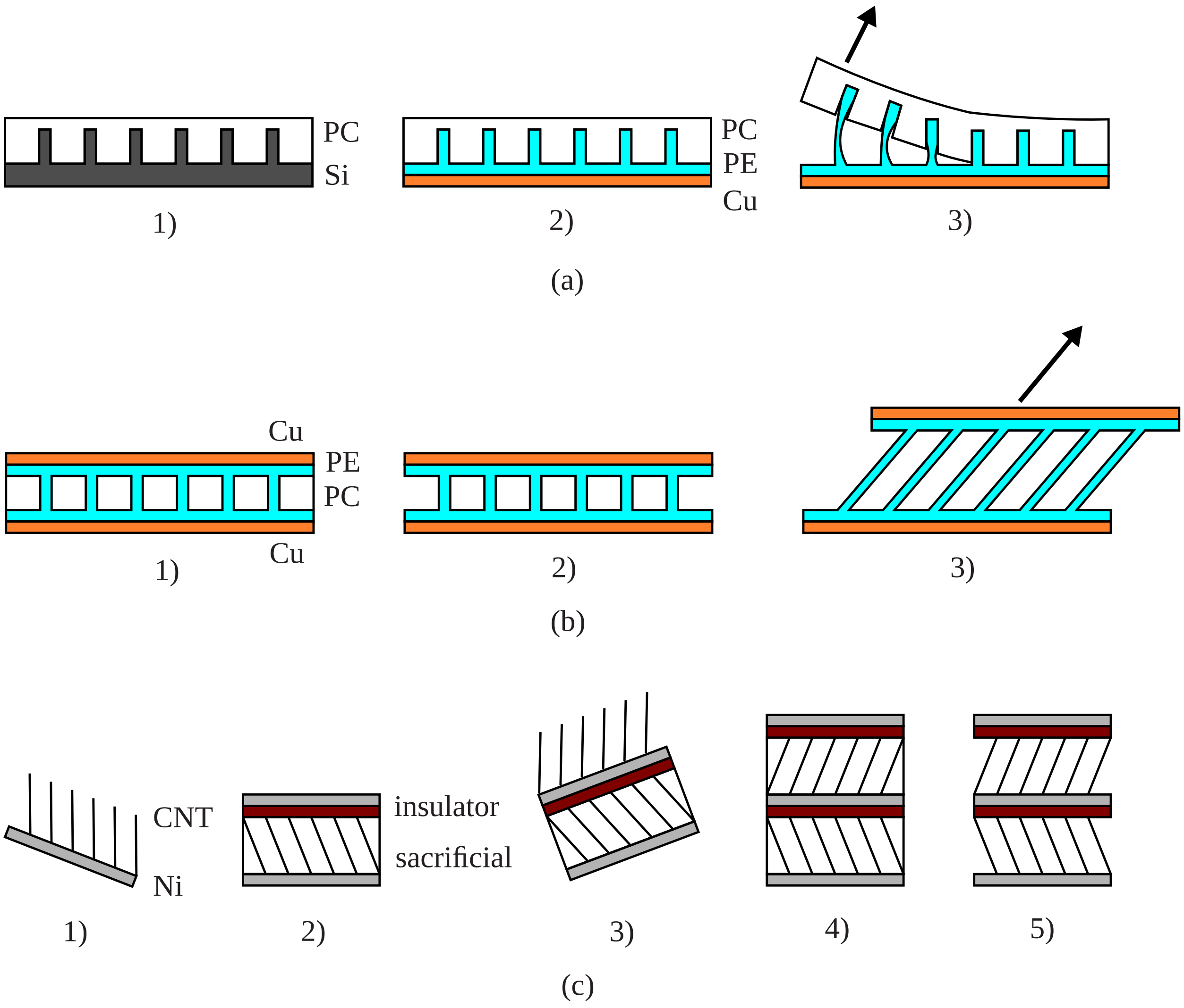

Figure 6.1: Future fabrication methods. (a) Fiber peeling from closed mold with regular pattern. 1) Mold polycarbonate (PC) over silicon (Si) nanowire template. 2) Remove PC from Si and mold polyethylene (PE) on copper (Cu) into the PC mold. 3) Peel off mold. (b) Fiber stretching with attached electrodes. 1) Sandwich a mold between polymer and electrodes. 2) Etch out the mold. 3) Stretch and angle the fibers to the desired dimensions. (c) Layered carbon nanotube (CNT) actuator. 1) Grow CNTs at an angle on nickel (Ni) substrate (see Figure 4.1). 2) Encapsulate CNTs in a sacrificial material and polish to provide flat surface for deposition of insulation layer and top electrode. 3) Deposit next layer of CNTs at opposite angle to create linear actuator. 4) Deposit insulation and electrode. 5) Remove sacrificial encapsulation layers.

Bibliography

[1] B. Aksak, M. P. Murphy, and M. Sitti. Adhesion of biologically inspired vertical and angled polymer microfiber arrays. *Langmuir*, 23:3322–3332, 2007.

[2] A. E. Aliev, J. Oh, M. E. Kozlov, A. A. Kuznetsov, S. Fang, A. F. Fonseca, R. Ovalle, M. D. Lima, M. H. Haque, Y. N. Gartstein, M. Zhang, A. A. Zakhidov, and R. H. Baughman. Giant-stroke, superelastic carbon nanotube aerogel muscles. *Science*, 323:1575–1578, 2009.

[3] R. A. Anderson, R. R. Lagasse, E. M. Russick, and J. L. Schroeder. Effects of void size and gas content on electrical breakdown in lightweight, mechanically compliant, void-filled dielectrics. *Journal of Applied Physics*, 91(5):3205–3212, 2002.

[4] M. Andrews, I. Harris, and G. Turner. A comparison of squeeze-film theory with measurements on a microstructure. *Sensors and Actuators A*, 36:79–87, 1993.

[5] M. Bao and H. Yang. Squeeze film air damping in MEMS. *Sensors and Actuators A*, 136:3–27, 2007.

[6] Y. Bar-Cohen, editor. *Electroactive polymer (EAP) actuators as artificial muscles: Reality, Potential, and Challenges*. SPIE-The International Society for Optical Engineering, Bellingham, Washington, 2nd edition, 2004.

[7] S. Bauer. Piezo-, pyro- and ferroelectrets: Soft transducer materials for electromechanical energy conversion. *IEEE Transactions on Dielectrics and Electrical Insulation*, 13(5):953–962, 2006.

[8] S. Bauer, R. Gerhard-Multhaupt, and G. M. Sessler. Ferroelectrets: Soft electroactive foams for transducers. *Physics Today*, 57:37–43, 2004.

[9] R. H. Baughman, C. Cui, A. A. Zakhidov, Z. Iqbal, J. N. Barisci, G. M. Spinks, G. G. Wallace, A. Mazzoldi, D. De Rossi, A. G. Rinzler, O. Jaschinski, S. Roth, and M. Kertesz. Carbon nanotube actuators. *Science*, 284:1340–1344, 1999.

[10] S. Bergbreiter, D. Mahajan, and K. S. J. Pister. A reusable micromechanical energy storage/quick release system with assembled elastomers. *Journal of Micromechanics and Microengineering*, 19:055009, 2009.

[11] S. M. Bobbio, M. D. Kellam, B. W. Dudley, S. Goodwin-Johansson, S. K. Jones, J. D. Jacobson, F. M. Tranjan, and T. D. DuBois. Integrated force arrays. *Micro Electro Mechanical Systems*, pages 149–154, 1993.

[12] P. Brochu and Q. Pei. Advances in dielectric elastomers for actuators and artificial muscles. *Macromolecular Rapid Communications*, 31:10–36, 2010.

[13] M. Camacho-Lopez, H. Finkelmann, P. Palffy-Muhoray, and M. Shelley. Fast liquid-crystal elastomer swims into the dark. *Nature Materials*, 3:307–310, 2004.

[14] C. G. Cameron, R. S. Underhill, M. Rawji, and J. P. Szabo. Conductive filler–elastomer composites for Maxwell stress actuator applications. *Proceedings of SPIE: Smart Structures and Materials 2004: Electroactive Polymer Actuators and Devices*, 5385:51–59, 2004.

[15] F. Carpi, P. Chiarelli, A. Mazzoldi, and D. De Rossi. Electromechanical characterisation of dielectric elastomer planar actuators: comparative evaluation of different electrode materials and different counterloads. *Sensors and Actuators A: Physical*, 107(1):85–95, 2003.

[16] F. Carpi, G. Gallone, F. Galantini, and D. De Rossi. Silicone-poly(hexylthiphene) blends as elastomers with enhanced electromechanical transduction properties. *Advanced Functional Materials*, 18(2):235–241, 2008.

[17] F. Carpi and E. Smela, editors. *Biomedical applications of electroactive polymer actuators*. John Wiley and Sons Ltd., United Kingdom, 2009.

[18] Y. Chen, D. T. Shaw, and L. Guo. Field emission of different oriented carbon nanotubes. *Applied Physics Letters*, 76(17):2469–2471, 2000.

[19] Z. Cheng and Q. Zhang. Field-activated electroactive polymers. *MRS Bulletin*, 33:183–187, 2008.

[20] P. B. Chu, P. R. Nelson, M. L. Tachiki, and K. S. J. Pister. Dynamics of polysilicon parallel-plate electrostatic actuators. *Sensors and Actuators A*, 52:216–220, 1996.

[21] W. P. Cox and E. H. Merz. The density dependence of the dielectric constant of polyethylene. *Journal of Polymer Science*, 28(118):622–625, 1958.

[22] B. G. Demczyk, Y. M. Wang, J. Cumings, M. Hetman, W. Han, A. Zettl, and R. O. Ritchie. Direct mechanical measurement of the tensile strength and elastic modulus of multiwalled carbon nanotubes. *Materials Science and Engineering A*, 334(1-2):173–178, 2002.

[23] Dynalloy Inc. Technical charactersistics of FLEXINOL® actuator wires. `http://www.dynalloy.com/TechSheets.html`, February 2011.

[24] S. Egawa, T. Niino, and T. Higuchi. Film actuators: planar, electrostatic surface-drive actuators. *Proceedings of IEEE Micro Electro Mechanical Systems*, pages 9–10, 1991.

[25] Etrema Products Inc. Data sheet Terfenol-D. `http://www.etrema-usa.com/documents/Terfenol.pdf`, February 2011.

[26] R. S. Fearing, K. H. Chiang, M. H. Dickinson, D. L. Pick, M. Sitit, and J. Yan. Wing transmission for a micromechanical flying insect. *Proceedings of the 2000 IEEE International Conference on Robotics & Automation*, 2:1509–1516, 2000.

[27] R. Frisch-Fay. *Flexible Bars*. Butterworth Inc., Washington, D.C., 1962.

[28] G. Gallone, F. Carpi, D. De Rossi, G. Levita, and A. Marchetti. Dielectric constant enhancement in a silicone elastomer filled with lead magnesium niobate–lead titanate. *Materials Science and Engineering C*, 27:110–116, 2007.

[29] A. N. Gent and S. Madan. Plastic yielding of partially crystalline polymers. *Journal of Polymer Science: Part B: Polymer Physics*, 27:1529–1542, 1989.

[30] R. Gerson and T. C. Marshall. Dielectric breakdown of porous ceramics. *Journal of Applied Physics*, 30(11):1650–1653, 1959.

[31] L. J. Gibson and M. F. Ashby. *Cellular Solids: Structures and Properties*. Cambridge University Press, Cambridge, United Kingdom, 2nd edition, 1997.

[32] S. M. Ha, I. S. Park, M. Wissler, R. Pelrine, S. Stanford, K. J. Kim, G. Kovacs, and Q. Pei. High electromechanical performance of electroelastomers based on interpenetrating polymer networks. *Proceedings of SPIE: Electroactive Polymer Actuators and Devices*, 6927:69272C–1–69272C–9, 2008.

[33] D. Halliday, R. Resnick, and K. S. Krane. *Physics*, volume 2. John Wiley & Sons, New York, NY, fifth edition, 2002.

[34] M. Hoffmann, D. Nüsse, and E. Voges. Electrostatic parallel-plate actuators with large deflections for use in optical moving-fibre switches. *Journal of Micromechanics and Microengineering*, 11:323–328, 2001.

[35] A. M. Hoover, E. Steltz, and R. S. Fearing. RoACH: An autonomous 2.4g crawling hexapod robot. *IEEE/RSJ International Conference on Intelligent Robots and Systems*, pages 26–33, 2008.

[36] R. G. Horn and D. T. Smith. Contact electrification and adhesion between dissimilar materials. *Science*, 256:362–364, 1992.

[37] C. Huang, R. Klein, F. Xia, H. Li, Q. M. Zhang, F. Bauer, and Z. Y. Cheng. Poly(vinylidene fluoride-trifluoroethylene) based high performance electroactive polymers. *IEEE Transactions on Dielectrics and Electrical Insulation*, 11(2):299–311, 2004.

[38] C. Huang, Q. Zhang, and A. Jákli. Nematic anisotropic liquid-crystal gels–self-assembled nanocomposited with high electromechanical response. *Advanced Functional Materials*, 13(7):525–529, 2003.

[39] I. W. Hunter and S. Lafontaine. A comparison of muscle with artificial actuators. *5th Technical Digest of IEEE Solid-State Sensor and Actuator Workshop*, pages 178–185, 1992.

[40] E. Husain and R. S. Nema. Analysis of Paschen curves for air, N_2, and SF_6. *IEEE Transactions on Electrical Insulation*, EI-17(4):350–353, 1982.

[41] J. W. Hutchinson and K. W. Neale. Neck propagation. *Journal of the Mechanics and Physics of Solids*, 31(5):405–426, 1983.

[42] M. Ieda. Dielectric breakdown process of polymers. *IEEE Transactions on Electrical Insulation*, EI-15(3):206–224, 1980.

[43] J. D. Jacobson, S. H. Goodwin-Johansson, S. M. Bobbio, C. A. Bartlett, and L. N. Yadon. Integrated force arrays: Theory and modeling of static operation. *Journal of Microelectromechanical Systems*, 4(3):139–150, 1995.

[44] H. E. Jeong, J. K. Lee, H. N. Kim, S. H. Moon, and K. Y. Suh. A nontransferring dry adhesive with hierarchical polymer nanohairs. *Proceedings of the National Academy of Sciences*, 106(14):5639–5644, 2009.

[45] H. E. Jeong, J. K. Lee, M. K. Kwak, S. H. Moon, and K. Y. Suh. Effect of leaning angle of gecko-inspired slanted polymer nanohairs on dry adhesion. *Applied Physics Letters*, 96:043704, 2010.

[46] H. E. Jeong, S. H. Lee, P. Kim, and K. Y. Suh. Stretched polymer nanohairs by nanodrawing. *Nano Letters*, 6(7):1508–1513, 2006.

[47] M. Karpelson, G. Y. Wei, and R. J. Wood. A review of actuation and power electronics options for flapping-wing robotic insects. *IEEE International Conference on Robotics and Automation*, pages 779–786, 2008.

[48] T. I. Kim, H. E. Jeong, K. Y. Suh, and H. H. Lee. Stooped nanohairs: geometry-controllable, unidirectional, reversible, and robust gecko-like dry adhesive. *Advanced Materials*, 21:2276–2281, 2009.

[49] R. Lakes. *Viscoelastic Materials*. Cambridge University Press, New York, NY, 2009.

[50] J. Lee, R. S. Fearing, and K. Komvopoulos. Directional adhesion of gecko-inspired angled microfiber arrays. *Applied Physics Letters*, 93:191910, 2008.

[51] Z. Liu and P. Calvert. Multilayer hydrogels as muscle-like actuators. *Advanced Materials*, 12(4):288–291, 2000.

[52] A. J. Lovinger. Ferroelectric polymers. *Science*, 220(4602):1115–1121, 1983.

[53] M. S.-C. Lu and G. K. Fedder. Position control of parallel-plate microactuators for probe-based data storage. *Journal of Microelectromechanical Systems*, 13:759–769, 2004.

[54] A. Masud. A 3-d model of cold drawing in engineering thermoplastics. *Mechanics of Advanced Materials and Structures*, 12:457–469, 2005.

[55] Matweb. `http://www.matweb.com`, February 2011.

[56] A. Mellinger and O. Mellinger. Breakdown threshold of dielectric barrier discharges in ferroelectrets: Where Paschen's law fails. *IEEE Transactions on Dielectrics and Electrical Insulation*, 18(1):43–48, 2011.

[57] H. Meng and J. Hu. A brief review of stimulus-active polymers responsive to thermal, light, magnetic, electric, and water/solvent stimuli. *Journal of Intelligent Material Systems and Structures*, 21:859–885, 2010.

[58] K. Minami, S. Kawamura, and M. Esashi. Fabrication of distributed electrostatic micro actuator (DEMA). *Journal of Microelectromechanical Systems*, 2:3, 1993.

[59] R. Nathanael, V. Pott, H. Kam, J. Jeon, and T. J. King Liu. 4-Terminal relay technology for complementary logic. *IEEE International Electron Devices Meeting (IEDM)*, pages 1–4, 2009.

[60] S. Nemat-Nasser and Y. Wu. Comparative experimental study of ionic polymer-metal composites with different backbone ionomers and in various cation forms. *Journal of Applied Physics*, 93(9):5255–5267, 2003.

[61] T. Niino, S. Egawa, H. Kimura, and T. Higuchi. Electrostatic artificial muscle: Compact, high-power linear actuators with multiple-layer structures. *Proceedings of IEEE Workshop on Micro Electro Mechanical Systems,* pages 130–135, 1994.

[62] J. W. Nilsson and S. A. Riedel. *Electric Circuits*. Prentice-Hall, Upper Saddle River, NJ, 6th edition, 2001.

[63] A. O'Halloran, F. O'Malley, and P. McHugh. A review on dielectric elastomer actuators, technology, application, and challenges. *Journal of Applied Physics*, 104:071101, 2008.

[64] M. A. Osman and A. Atallah. Interparticle and particle-matrix interactions in polyethylene reinforcement and viscoelasticity. *Polymer*, 46:9476–9488, 2005.

[65] A. Peigney, Ch. Laurent, E. Flahaut, R. R. Bacsa, and A. Rousset. Specific surface area of carbon nanotubes and bundles of carbon nanotubes. *Carbon*, 39(4):507–514, 2001.

[66] R. Pelrine, R. Kornbluh, J. Joseph, R. Heydt, Q. Pei, and S. Chiba. High-field deformation of elastomeric dielectrics for actuators. *Materials Science and Engineering C*, 11:89–100, 2000.

[67] R. Pelrine, R. Kornbluh, Q. Pei, and J. Joseph. High-speed electrically actuated elastomers with strain greater than 100%. *Science*, 287:836–839, 2000.

[68] R. E. Pelrine, R. D. Kornbluh, and J. P. Joseph. Electrostriction of polymer dielectrics with compliant electrodes as a means of actuation. *Sensors and Actuators A*, 64:77–85, 1998.

[69] K. Peng, M. Zhang, A. Lu, N. B. Wong, R. Zhang, and S. T. Lee. Ordered silicon nanowire arrays via nanosphere lithography and metal-induced etching. *Applied Physics Letters*, 90:163123, 2007.

[70] Piezo Systems Inc. Piezoceramic materials and properties, PSI-5H4E. `http://www.piezo.com/prodmaterialprop.html`, February 2011.

[71] J. S. Plante and S. Dubowsky. On the properties of dielectric elastomer actuators and their design implications. *Smart Materials and Structures*, 16:S227–S236, 2007.

[72] E. P. Popov and T. A. Balan. *Engineering Mechanics of Solids*. Prentice-Hall, Inc., Upper Saddle River, NJ, 2nd edition, 1998.

[73] X. Qiu and R. Gerhard. Effective polarization fatigue from repeated dielectric barrier discharges in cellular polypropylene ferroelectrets. *Applied Physics Letters*, 93:152902, 2008.

[74] G. G. Raju. *Dielectrics in Electric Fields*. Marcel Dekker, Inc., New York, NY, 2003.

[75] S. Rosset, M. Niklaus, P. Dubois, and H. R. Shea. Metal ion implantation for the fabrication of stretchable electrodes on elastomers. *Advanced Functional Materials*, 19(3):470–478, 2009.

[76] M. N. O. Sadiku. *Elements of Electromagnetics*. Oxford University Press, Inc., New York, NY, 3rd edition, 2001.

[77] J. I. Seeger and B. E. Boser. Charge control of parallel-plate electrostatic actuators and the tip-in instability. *Journal of Microelectromechanical Systems*, 12:656–671, 2003.

[78] S. D. Senturia. *Microsystem Design*. Springer Science+Business Media, LLC, New York, NY, 2001.

[79] M. Shahinpoor and K. J. Kim. Solid-state soft actuator exhibiting large electromechanical effect. *Applied Physics Letters*, 80(18):3445–3447, 2002.

[80] M. Shahinpoor and K. J. Kim. Ionic polymer-metal composites: IV. Industrial and medical applications. *Smart Materials and Structures*, 14:197–214, 2005.

[81] M. Shahipoor, I. D. Norris, B. R. Mattes, K. J. Kim, and L. O. Sillerud. Electroactive polyacrylonitrile nanofibers as artificial nanomuscles. *Proceedings of SPIE Smart Structures and Materials, Electroactive Polymer Actuators and Devices (EAPAD)*, 4695:351–358, 2002.

[82] P. G. Slade and E. D. Taylor. Electrical breakdown in atmospheric air between closely spaced (0.2 μm-40 μm) electrical contacts. *IEEE Transactions on Components and Packaging Technologies*, 25(3):390–396, 2002.

[83] E. Smela, W. Lu, and B. R. Mattes. Polyaniline actuators. Part 1. PANI(AMPS) in HCl. *Synthetic Metals*, 151:25–42, 2005.

[84] J. B. Starr. Squeeze-film damping in solid-state accelerometers. *IEEE Solid-State Sensor and Actuator Workshop, 1990. 4th Technical Digest*, pages 44–47, 1990.

[85] A. Streicher, R. Müller, H. Peremans, M. Katenbacher, and R. Lerch. Ferroelectrets: ultrasonic transducer for a biomimetic sonar system. *IEEE Ultrasonics Symposium*, 2:1142–1145, 2005.

[86] J. Su, J. S. Harrison, and T. St. Clair. Novel polymeric elastomers for actuation. *Proceedings of IEEE International Symposium on Application of Ferroelectrics*, 2:811–814, 2000.

[87] W. C. Tang, T. C. H. Nguyen, and R. T. Howe. Laterally driven polysilicon resonant microstructures. *Sensors and Actuators*, 20:25–32, 1989.

[88] W. C. Tang, T. C. H. Nguyen, M. W. Judy, and R. T. Howe. Electrostatic-comb drive of lateral polysilicon resonators. *Sensors and Actuators A: Physical*, 21(1-3):328–331, 1990.

[89] W. M. van Spengen, R. Puers, R. Mertens, and I. De Wolf. A comprehensive model to predict the charging and reliability of capacitive rf mems switches. *Journal of Micromechanics and Microengineering*, 14:514–521, 2004.

[90] W. Veijola, H. Kuisma, and J. Lahdenperä. Model for gas film damping in a silicon accelerometer. *Proceedings of the International Conference on Solid State Sensors and Actuators (TRANSDUCERS '97)*, 2:1097–1100, 1997.

[91] J. W. Waanders. *Piezoelectric Ceramics: Properties and Applications*. N. V. Philips' Gloeilampenfabrieken, Eindhoven, The Netherlands, 1991.

[92] X. Wang, W. Zeng, G. Lu, O. L. Russo, and E. Eisenbraun. High aspect ratio Bosch etching of sub-0.25 μm trenches for hyperintegration applications. *Journal of Vacuum Science and Technology B*, 25:1376–1381, 2007.

[93] T. C. Waram. *Acutator Design Using Shape Memory Alloys*. T. C. Waram, Hamilton, Ontario, 2nd edition, 1993.

[94] M. Wegener, W. Wirges, R. Gerhard-Multhaupt, M. Dansachmüller, R. Schwödiauer, S. Bauer-Gogonea, S. Bauer, M. Paajanen, H. Minkkinen, and J. Raukola. Controlled inflation of voids in cellular polymer ferroelectrets: Optimizing electromechanical transducer properties. *Applied Physics Letters*, 84(3):392–394, 2004.

[95] J. Wibbeler, G. Pfeifer, and M. Hietschold. Parasitic charging of dielectric surfaces in capacitive microelectromechanical systems (MEMS). *Sensors and Actuators A*, 71:74–80, 1998.

[96] W. Wirges, M. Wegener, O. Voronina, L. Zirkel, and R. Gerhard-Multhaupt. Optimized preparation of elastically soft, highly piezoelectric, cellular ferroelectrets from nonvoided poly(ethylene terephthalate) films. *Advanced Functional Materials,* 17:324–329, 2007.

[97] R. J. Wood. *Composite Microstructures , Microactuators and Sensors for Biologically Inspired Micro Air Vehicles*. PhD thesis, University of California, Berkeley, 2004.

[98] R. J. Wood. The first takeoff of a biologically inspired at-scale robotic insect. *IEEE Transactions on Robotics*, 24(2):341–347, 2008.

[99] W. Yuan, L. B. Hu, Z. B. Yu, T. Lam, J. Biggs, S. M. Ha, D. J. Xi, B. Chen, M. K. Senesky, G. Grüner, and Q. Pei. Fault-tolerant dielectric elastomer actuators using single-walled carbon nanotube electrodes. *Advanced Functional Material*, 20(3):621–625, 2008.

[100] J. Zhang, N. Kikuchi, V. Li, A. Yee, and G. Nusholtz. Consitutive modeling of polymeric foam material subjected to dynamic crash loading. *International Journal of Impact Engineering*, 21(5):369–386, 1998.

[101] R. Zhang, P. Lochmatter, A. Kunz, and G. Kovacs. Dielectric elastomer spring roll actuators for portable force feedback device. *International Symposium on Haptic Interfaces for Virtual Environment and Teleoperator Systems (HAPTICS'06)*, page 53, 2006.

[102] M. Zupan, M. F. Ashby, and N. A. Fleck. Actuator classification and selection–the development of a database. *Advanced Engineering Materials*, 4(12):933–940, 2002.

Appendix A

Fiber pulling angles

When creating angled fibers by peeling a mold from a stationary sample using moving stages, some consideration needs to be given to the peeling angle, θ_{peel}, and the pulling angle, θ_{pull}. As shown in Figure A.1, the peeling angle is the angle of the mold with respect to the substrate, and the pulling angle is the angle of the motion of the stages with respect to the substrate. The pull and peel angles are not the same, except for the case where $\theta_{peel} = 0$.

Figure A.1 shows two positions of a mold being peeled away from the substrate. The pull angle can be solved for using simple trigonometry if it is assumed that the mold material is not elastic. Then, as it is peeled away from the substrate, the length of the mold not attached to the substrate increases by an amount equal to the length of substrate exposed, ΔL. Then, the pull angle is,

$$\begin{aligned}\theta_{pull} = \tan^{-1}\left(\frac{y}{x+\Delta L}\right) &= \tan^{-1}\left(\frac{\Delta L \sin\theta_{peel}}{\Delta L \cos\theta_{peel} + \Delta L}\right)\\ &= \tan^{-1}\left(\tan\frac{\theta_{peel}}{2}\right) = \frac{\theta_{peel}}{2} \qquad \text{(A.1)}\end{aligned}$$

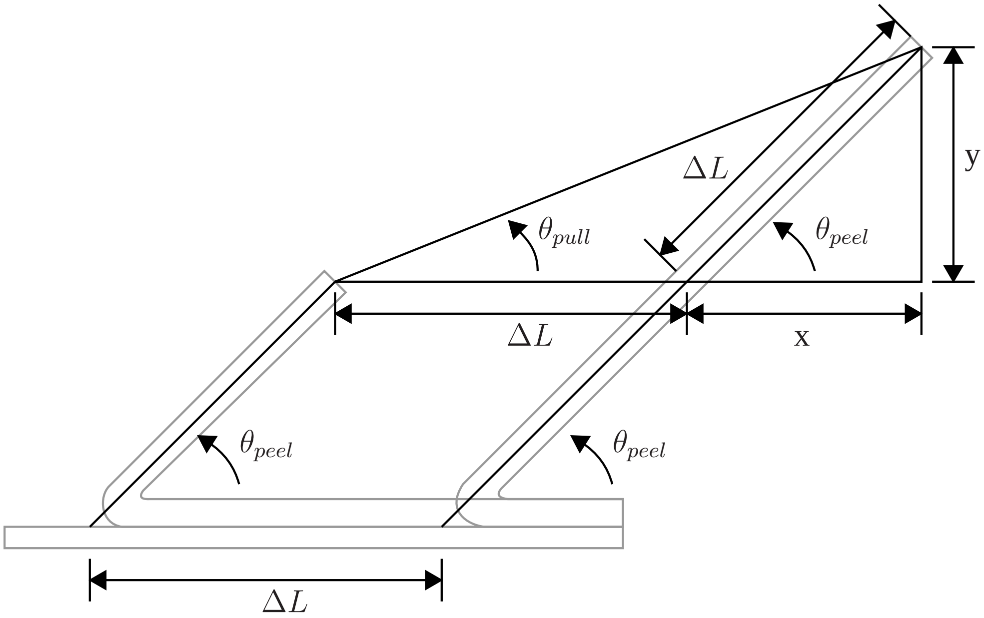

Figure A.1: Geometric diagram of peeling.